ASSESSMENT OF RADIOTHERAPY OF CANCER BY APOPTOSIS IMAGING WITH F-18 ML-10

A Dissertation
Presented to
The Academic Faculty

by

Kedi Zhou

In Partial Fulfillment
of the Requirements for the Degree
Doctor of Philosophy in the
Department of Biomedical Engineering
College of Engineering

Georgia Institute of Technology
Emory University
Peking University
August 2017

ASSESSMENT OF RADIOTHERAPY OF CANCER BY APOPTOSIS IMAGING WITH F-18 ML-10

Approved by:

Dr. Qiushi Ren, Advisor
Department of Biomedical Engineering
Peking University

Dr. Zhifei Dai
Department of Biomedical Engineering
Peking University

Dr. Shuming Nie, Co-advisor
Department of Biomedical Engineering
Emory University

Dr. Kun Yang
Department of Quality and Technical Supervision
Hebei University

Dr. Changhui Li
Department of Biomedical Engineering
Peking University

Date Approved: June 2, 2017

To my family

ACKNOWLEDGEMENTS

This dissertation was finished under the support and guidance from my advisors Dr. Qiushi Ren and Dr. Shuming Nie. I started my journey of pursuing the PhD degree from 2011 in Ren lab, and spent a year and half in Nie lab at Emory. I learnt so much from Qiushi and Shuming, and I would like to express my sincere thanks to them.

Thanks for the support from Wallace H. Coulter Foundation and Chinese Scholarship Council, and thanks to Dr. Cheng Zhu and Dr. Shiyi Chen for running the joint program

I would like to thank my thesis committee members: Dr. Zhifei Dai, Dr. Zuhong Lu, Dr. Changhui Li, Dr. Mingyuan Gao, Dr. Jinming Zhang, Dr. Kun Yang, and Dr. Peng Xi. I would also like to thank my supervisors Dr. Hongfang Sun, Dr. Jinming Zhang, Dr. Ximei Qian, and Dr. Jiahe Tian.

I would like to especially thank my parents and my wife.

I would also like to thank my colleagues and friends from Beijing and Atlanta. I would like to especially thank Dr. Yanye Lu, Mingbing Guo, Congzhe Zhang, Dr. Yichen Ding, Dr. Hening Wang, Bo Pang, Xiangxi Meng, Ivan Vuletic, Sihao Zhu, Zhaoheng Xie, Kun Zhou, Suying Li, Jian Tian, Qiushi Zhang, Yue Yu, Zekuan Yu, Da Zou, Lingyi Zhao, Zhe Jiang, Huan Xu, Jing Xiang, Xi Liu, Xiaohui Zhai from Ren lab; Dr. Yiqing Wang, Dr. Jinzhi Du, Dr. Jie Song, Dr. Hui Wei, Dr. Brad Kairdolf, Dr. Gee Young Lee, and Dr. Lucas Lane from Nie lab; Xiaojun Zhang and Jian Liu from General Hospital of PLA. I would also like to thank Dr. Zhenhai Li, Dr. Lining Ju, Dr. Xiaokun Wang, Dr. Jie Liu, Dr. Qingshen Jing, Yunfeng Chen, and Chenghao Ge.

I would like to acknowledge Beijing Arrays Molecular Imaging Corporation and colleagues in General Hospital of PLA.

I would like to thank Jialei Luo, Xiaofeng Gao and Shannon Sullivan for their help. I would also like to thank Dr. Hongfang Sun for kind revision of my dissertation over and over.

TABLE OF CONTENTS

LIST OF TABLES

LIST OF FIGURES

LIST OF SYMBOLS AND ABBREVIATIONS

©	A vacancy of Ca site
F-18 ML-10	F-18 labeled 2-(5-fluoropentyl)-2-methyl malonic acid
PET	Positron emission tomography
MRI	Magnetic resonance imaging
K2.2.2	4,7,13,16,21,24-hexaoxa-1,10-diazabicyclo (8.8.8) hexacosane
SERS	Surface enhanced Raman scattering
GBM	Glioblastoma multiforme
WHO	World Health Organization
NCI	National Cancer Institute
CT	Computed tomography
GWAS	Genome-wide associated study
MI	Molecular imaging
SPECT	Single photon emission computed tomography
ICG	Indocyanine green
DNA	Deoxyribonucleic acid
RNA	Ribonucleic acid
F-18 FDG	F-18 fluorodeoxyglucose
USP	United States Pharmacopeia
ChP	Chinese Pharmacopoeia
EP	European Pharmacopoeia
TLC	Thin layer chromatography
GC	Gas chromatography

HPLC	High performance liquid chromatography
LC/MS/MS	Liquid chromatography-tandem mass spectrometry
CNS	Central nervous system
MRS	Magnetic resonance spectroscopy
DOT	Diffuse optical tomography
CK	CyberKnife
ROI	Region of interest
FOV	Field of view
ECG	Electrocardiography
GTV	Gross tumor volume
TSP	Trisodium phosphate
HCL	Hydrochloric acid
DMEA	N, N-dimethylethanolamine
NBS	N-bromosuccinimide
EDTA	Ethylenediaminetetraacetic acid
DTPA	Diethylenetriaminepentaacetic acid
QD	Quantum dots
BSA	Bovine serum albumin
PBS	Phosphate buffered saline
GFP	Green fluorescence protein
FMT	Fluorescence molecular tomography
LYSO	Lutetium-yttrium oxyorthosilicate
PS-PMT	Position sensitive multi-anode photomultiplier tube
SiPM	Silicon photomultiplier
NIR	Near-infrared

EPR	Enhanced permeability and retention
Tc-99m MIBI	Tc-99m 2-Methoxyisobutylisonitrile
ADHD	Attention Deficit Hyperactivity Disorder
PD	Parkinson’s disease

SUMMARY

Cancer, currently the second leading cause of death in the United States, is expected to become the first killer in the near future by surpassing heart diseases. Molecular imaging has become a key tool in the biomedical research and clinical diagnosis. By employing specific imaging probes, molecular imaging traces various biological processes at the molecular level in living tissues with high resolution and specificity. In this dissertation, the early assessment of clinical radiotherapy effects has been carried by positron emission tomography (PET) imaging with F-18 labeled 2-(5-fluoropentyl)-2-methyl malonic acid (F-18 ML-10). However, most of the researches on application of F-18 ML-10 are preclinical studies.

Currently, the clinical assessment of radiotherapy effects is based on the measurement of tumor size by magnetic resonance imaging (MRI) 2-4 months post radiotherapy. However, several months' late assessment caused many patients who is bearing malignant tumor to lose the chance of surrogate therapy. This has caused an impediment for the management of therapy plan. Therefore, there is a great demand for early assessment of radiotherapy of cancer in the clinic. As apoptosis of tumor cells is one of the early events that occurred after radiotherapy, therefore monitoring of apoptotic cells by F-18 ML-10 PET imaging can be used for the early assessment. However, there are many challenges for its clinical use.

As is produced through F-18 fluoride labelling via nucleophilic substitution reaction, Kryptofix 2.2.2 (K2.2.2) is one of the most widely used phase-transfer reagents for F-18 nucleophilic substitution reaction. Due to the toxicity of K2.2.2, its residue in F-18

radiopharmaceuticals should not exceed 50 μg/mL, as required by the United States Pharmacopeia 40. However, false-positive or false-negative results of K2.2.2 detection affects the safety of F-18 pharmaceuticals. In this dissertation, we have overturned the hypothesis that amine compounds caused the false positive results. Moreover, we also proposed and tested the effect of reductive stabilizer and pH value on the false negative results.

In the investigation on safety assessment of radiotherapy, a special clinical case for therapeutic assessment on lung cancer after CK treatment has been investigated. After CK treatment, there was no significant change in the apoptosis of tumor. However, the apoptosis in heart tissue and aortic arch increased significantly, indicating injuries in adjacent tissue by CK treatment caused by a rapid apoptotic response. The late return visit indicated that the cancer recurred, this is coincident with the F-18 ML-10 imaging results. This finding was verified by following preclinical studies on rabbits. Thus, this case study suggested that this method has the potential for the assessment of subsidiary-injury of lung cancer radiotherapy.

In the investigation on efficacy assessment of radiotherapy, in the clinical applications, 29 clinical cases of different types of brain tumor have been included, and the PET image has been analyzed volume-by-volume in assessment of response of different types of tumors to CyberKnife (CK) radiotherapy. There are many challenges for quantitative analysis of therapeutic assessment by using apoptosis imaging. As apoptosis is essentially a transient process, it is necessary to standardize the imaging method and time point, and to make quantitative analysis based on “volume-by-volume” of the image, to distinguish between cell apoptosis and spontaneous apoptosis. Furthermore, correlation between the

result of this early assessment and subsequent anatomic change in tumor determined by MRI was also investigated. The results show a high correlation between the F-18 ML-10 imaging results and the tumor volume changes evaluated by MRI. This research has provided a clinical method for the early evaluation of tumor radiotherapy. The applicability of this method has been discussed by analyses on different brain tumor types.

In addition, two other imaging related projects which I have done during my PhD period are also included in this dissertation. For the application of spectroscopic molecular imaging to real-time surgery guidance, the sensitivity of a novel surface enhanced Raman spectroscopy (SERS) hand-held spectroscopic device for intraoperative tumor detection has been investigated. The SERS gold nanoparticles have been proved to be ultra-high sensitive for in vitro detection with wide dynamic range, thus could distinguish the signal of tumor tissue from that of normal tissue. Furthermore, the differentiation of tumor tissue from inflammatory tissue has also been investigated by a preclinical quad-modality imaging with multiple probes.

CHAPTER 1. INTRODUCTION

An estimated 1,688,780 new cases of cancer will be diagnosed in the United States and 600,920 people will die from the disease in 2017 [1]. The World Health Organization (WHO) has published the "World Cancer Report 2014", analyzing the overall situation and current trends of cancer among more than 180 countries and 28 types of carcinoma around the world. According to this report and data from National Cancer Institute (NCI), the global number of people living beyond a cancer diagnosis, having reached 14 million in 2012, is predicted that the global cancer cases will show a rapid growth. It is expected to reach 19 million in 2025 [2]. The annually global expenditures for cancer care totaled higher than $895 billion. In China, the estimated nationwide 5-year cancer prevalence was 7.49 million, and the 5-year prevalence proportion was 556/100,000 [3].

1.1 Current challenges in cancer therapeutics

"To cure sometimes, to relieve often, to comfort always" is a well-known quotation from Dr. Edward L. Trudeau in nineteenth century. Although have many new technologies been developed in the past century, there is still lack of effective therapeutics for many diseases especially cancer. The variation in the biologic behavior of tumor is one of the major challenges for complete elimination of cancer [4, 5]. To make a progress on cure of cancer and personalized healthcare, President Obama launched "Precision Medicine Initiative" in January 2015. Personalized healthcare is helpful in medical practice, and information in the molecular level will make medicine more precise.

1.1.1 Challenges in early diagnosis

With traditional diagnostic methods, cancer could not be diagnosed in a very early stage. Patients in many cases are not diagnosed until the tumor has been growing to later stage with significant size or effect to their health. Clinical results show that the improvement of the five-year survival rate of cancer patients is mainly due to early diagnosis followed by proper therapeutics with currently available treatment technology and methods. Therefore, early diagnosis is an important way to improve the treatment outcome and reduce medical expense.

1.1.2 Challenges in early assessment after treatment

There are more than 20,000 of newly diagnosed brain tumor patients in the United States each year, of which 70% were malignant glioblastoma multiforme (GBM) [6-8]. However, the average survival period after therapy is only 12 to 15 months. In this situation, it is needed to make a breakthrough not only in therapeutic method, but also in assessment early after therapeutic. Currently, the most common method to assess therapeutic outcome is magnetic resonance imaging (MRI), by comparison the morphological change of tumor. However, there are limitations of the application of this method in terms of early evaluation, since the changes in tumor size usually takes a certain period before being reflected, and therefore cannot accurately reflect the changes in the molecular physiology of tumors at an early stage.

Nowadays, the most common radical cancer treatments are surgery, radiotherapy and chemotherapy. Among them, radiotherapy is an important method for intracranial treatment that could either be a main regiment, or adjuvant therapy after surgery for keeping cancer from recurrence. The evaluation of therapeutic response mainly relies on

the change of tumor size assessed by computed tomography (CT) and MRI images. For radiotherapy and chemotherapy, however, the anatomical volume change comes later than the rapid biological change on cellular level, resulting in a serious lag effect for the evaluation [9]. Indeed, the anatomical volume change of intracranial tumor is difficult to be visualized by CT or MRI till 4-8 weeks after whole brain radiotherapy [10, 11]. Particularly, for patients with malignant brain tumor, such as high-grade gliomas and metastatic tumors, etc., the average survival time is short. With the lag effect of conventional assessments, the early response after radiotherapy is hard to be assessed which might result in a delay or loss of chance for an alternative treatments [12-14]. Moreover, the tumor tissue and radio-necrotic tissue could not be distinguished by CT and MRI images, which might cause ambiguous or even wrong judgment of therapeutic effect. Therefore, a method which could offer an early response assessment after radiotherapy for clinical management improvement is required.

Apoptosis is a basic biological process regulating cell death and playing an important role in many diseases. Apoptosis imaging has been widely applied to visualize tumor hallmark [15-29]. Spontaneous apoptosis in tumors is increased than in normal tissue, and apoptosis generally reflects tumor molecular physiological processes, which could be used as a useful indicator of tumor progress by comparing the apoptosis imaging before and early after treatment.

1.2 Molecular imaging

1.2.1 Precision medicine

The principle of precision medicine, formerly known as personalized medicine, is using of specialized treatment for particular disease from a specific patient, at a particular time. However, we still cannot classify those diseases, patients and treatments based on current research progress of biology or medicine. Unlike genome-wide associated study (GWAS), molecular imaging does not focus on the mechanism of tumorigenesis. To achieve precision medicine, molecular imaging provides an approach to visualize physiological changes in early stage of cancer from the signal of molecular probes.

1.2.2 Molecular imaging

Imaging is a brilliant strategy to get information without knowing the detailed activities of biological processes. As shown in Figure 1.1, recent advances of molecular imaging provide great opportunities for early diagnosis of cancer [30-32]. In the past decade, researches on drug design, discovery, and delivery have enhanced the performance of chemotherapy and radiotherapy by improving the selectivity and reducing the toxicity [33, 34], thus providing effective therapeutic regimen especially for the treatment of widespread tumors. Molecular probes are specifically modified molecules those who could visualize specific physiological information. Once after being injected in human body, molecular probes could recognize then combine with certain biomarker such as receptor, enzyme, nucleic acid, etc. By visualizing the signal from molecular probe from high-precision imaging, we could obtain molecular information of disease progression.

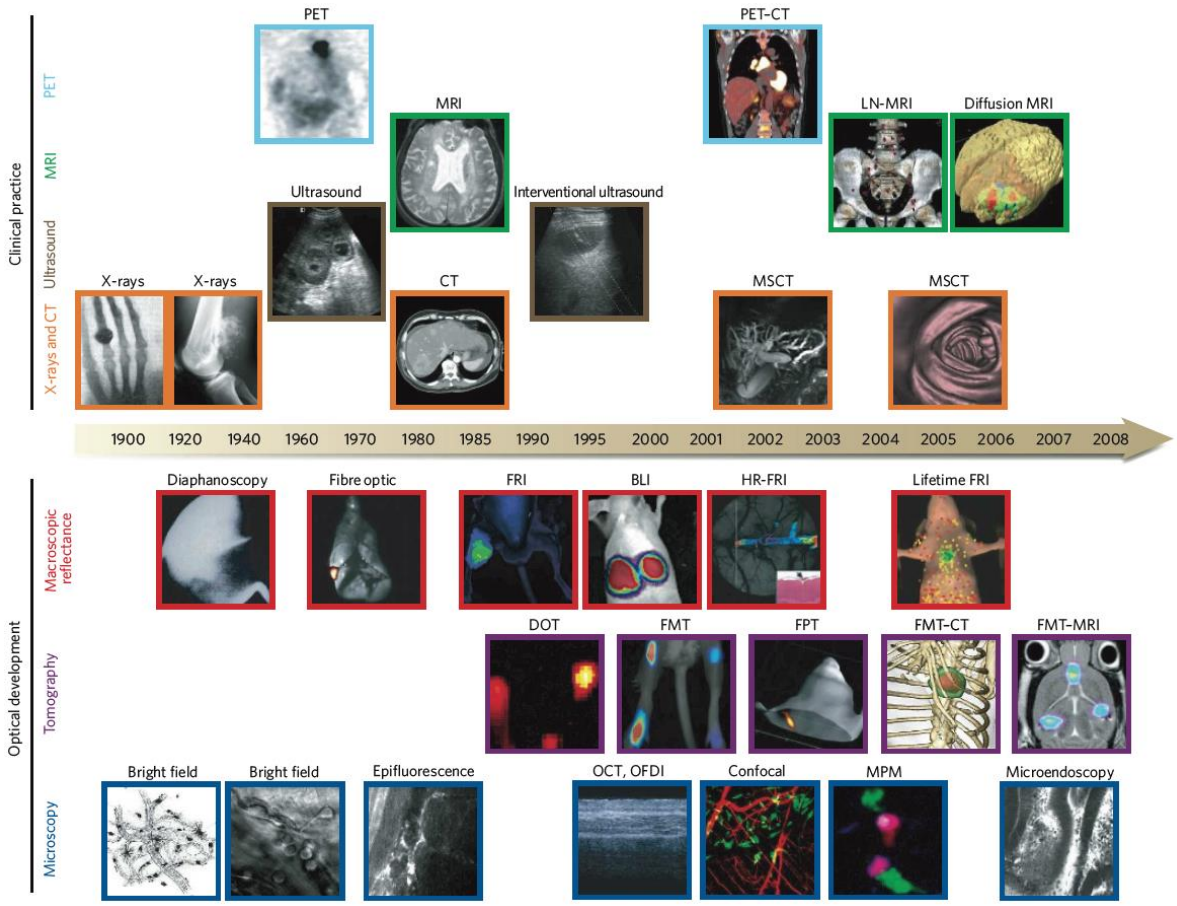

Figure 1.1 – Development of molecular imaging used in oncology. Reprinted from Weissleder and Pittet [30] with permission. Copyright © 2008 Nature Publishing Group.

In clinical trials, the regular treatment for localized and locally advanced tumor is still dominated by surgical resection combined with chemo or radiology. Especially, compared to non-surgical treatment, surgery could greatly improve the survival of patients, by accurate tumor staging and complete removal of lesions. According to statistics, surgery can prolong survival rate of patients with lung cancer 10 times, thus surgery is still the preferred option for cancer treatment. During surgery, however, the surgeon still mainly dependent on two tools: the eyes to look suspicious tissue, and the hands to feel abnormal tissue; thus inevitably causing problems with incomplete excision, thereby leading to tumor

recurrence and metastasis, which is the biggest problem of tumor surgery, because once the recurrence and metastasis, then surgery is extremely difficult to occur, which seriously affected the survival of patients [35]. According to statistics, the ratio of patients with postoperative local recurrence of tumor after surgery reaches 40%. As the molecular imaging could accurately distinguish cancerous and normal tissues, detect and locate cancerous tissue, especially tumor accurately determine edge positions, which will greatly increase the possibility complete resection of the tumor, the surgical accuracy could be improved significantly. The second specific aim of this project is focused on an investigation on sensitivity of hand-held spectroscopic imaging device for surgery guidance.

With the completion of Human Genome Project and the progress of gene sequencing of various animals, it has been found that the genes of mice that commonly used in laboratory is highly homologous to human [36]. The development of transgenic technology has made it possible to project human diseases to animal models, used to support the research of related diseases, the development of new drugs, and the evaluation of drug efficacy [37-39]. Due to the differences between individuals, in vivo imaging is critical to the diagnosis and treatment of cancer. Since the 1980s, the Medical Imaging technology has been developed from the traditional single structural imaging towards the stage of multi-modal functional and Molecular Imaging. The development of genomics and molecular biology has improved our understanding of diseases into the cellular and molecular level.

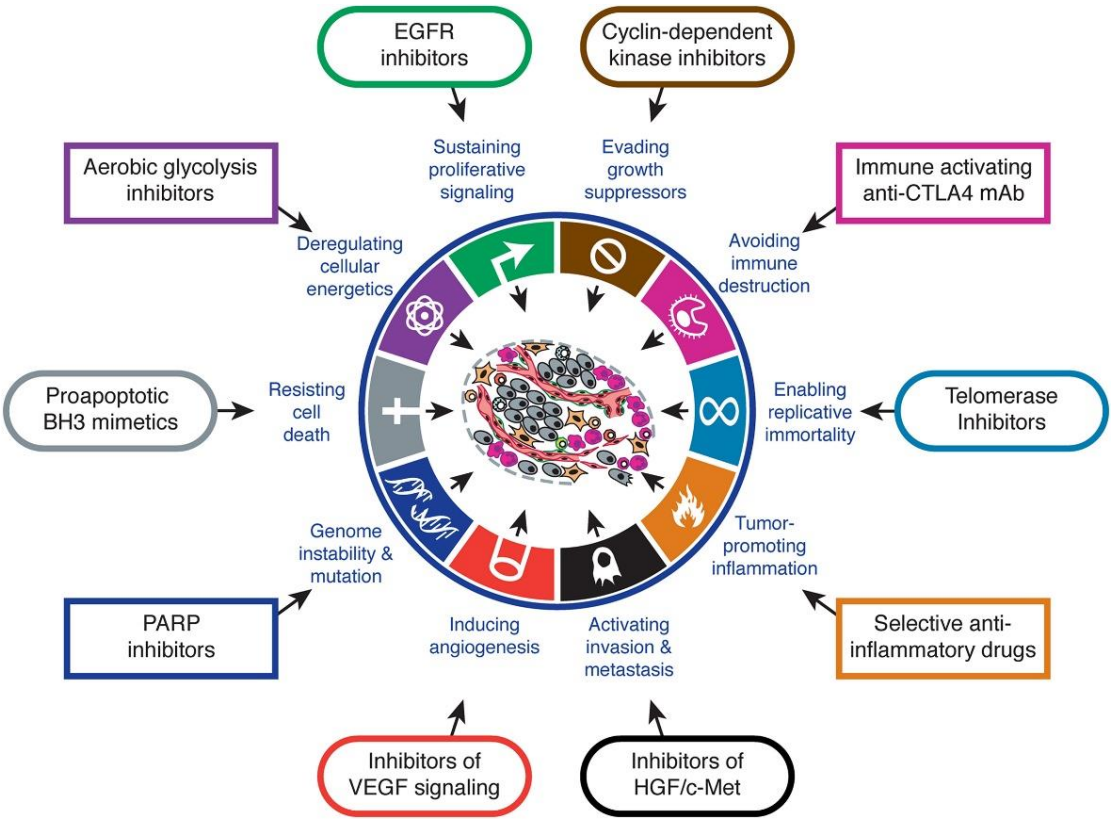

Figure 1.2 – Active targeting and hallmarks of cancer. Reprinted from Hanahan et al [40] with permission. Copyright © 2011 Elsevier Inc.

Dr. Ralph Weissleder and colleagues first proposed the concept of Molecular Imaging (MI) in 1999 [41], which means applying the imaging methods to perform qualitative and quantitative research on biological process in vivo at the cellular and molecular level [42, 43]. This method uses specific biomarker in human body as the target of molecular probes, and noninvasively images the internal physiological or pathological processes at the molecular level, based on existing medical imaging technologies, as depicted in Figure 1.2 [40]. The molecular imaging integrates physiological information, which is then detected by sophisticated imaging technique and processed through a series of image post-processing techniques, to represent the real-time biological processes in vivo at the cellular and molecular level.

1.2.3 Principles of molecular imaging for early diagnosis

Since it was proposed in 1990s, molecular imaging has become a key tool in the biomedical research and clinical imaging [44, 45]. Molecular imaging traces the biological processes at the molecular level in living tissues with high resolution and specificity, sensing diseases at their very early stage. Various molecular imaging methods based on different mechanisms, such as the radiolabeling and optical labeling, have gained significant progresses over past decades [46-64]. The most common imaging modalities are CT, positron emission tomography (PET), single photon emission computed tomography (SPECT), MRI, and ultrasound, etc.

However, a living body is an extremely complex system, imaging such system using a single biomarker is generally not enough to understand its physiology. Even a simple biological process gets involved in many biochemical reactions, and a single biomarker might only partially represent the process. Moreover, different biological processes may have overlap in molecular reactions. For instance, both cancer and inflammation can cause abnormal metabolic activities, so that tracing the glucose metabolism alone cannot separate these two distinct diseases. Thus, using multiple biomarkers that could trace different biological processes in the living animal is of great desire for biomedical research. On the other hand, the use of different biomarkers vary in depth, location, chemical property, and concentration, etc., which require multimodal imaging methods [65]. Therefore, multimodal and multi-probes molecular imaging gain increasing interest and will have great impact on the biomedical imaging [66-78].

Multi-modality imaging, which is capable of providing non-invasive and real-time *in vivo* observations of biomedical processes, has been developed for preclinical researches, such as new pharmacological studies, drug distribution, disease diagnosis, especially in cancer research [44, 45]. In general, imaging modalities could be divided into anatomical and functional imaging. Anatomical imaging modalities, such as ultrasound imaging, computed tomography (CT) and magnetic resonance imaging (MRI) can provide anatomical information whereas the functional imaging modalities [e.g. positron emission tomography (PET), single photon emission computed tomography (SPECT) and fluorescence imaging (FMI)] excel at detecting or measuring changes in metabolism, blood flow, regional chemical composition, and absorption that very often use tracers or probes to reflect spatial distribution of them in the body. However, each single molecular imaging method cannot answer all biological questions and is inadequate to meet ever increasing demands of resolution, sensitivity and specificity in today's scientific research. An ideal imaging method should be able to furnish anatomical, physiological, and molecular information with high sensitivity, specificity and good resolution. Because no single imaging modality can provide information on all these aspects, it is very desirable that a system combines these imaging modalities to harness the strengths of different imaging methods. Following the development of the first dual-modality imaging system[53, 54], which combined SPECT and CT, the concept of multi-modality imaging technology has been widely recognized and accepted in both preclinical and clinical studies. Therefore, most of the multi-modality imaging combinations have been devoted toward integrating one technique from each group, for example, PET-CT, SPECT-CT, Optical-CT, PET-SPECT-CT and most recently PET-MR. [46-52]

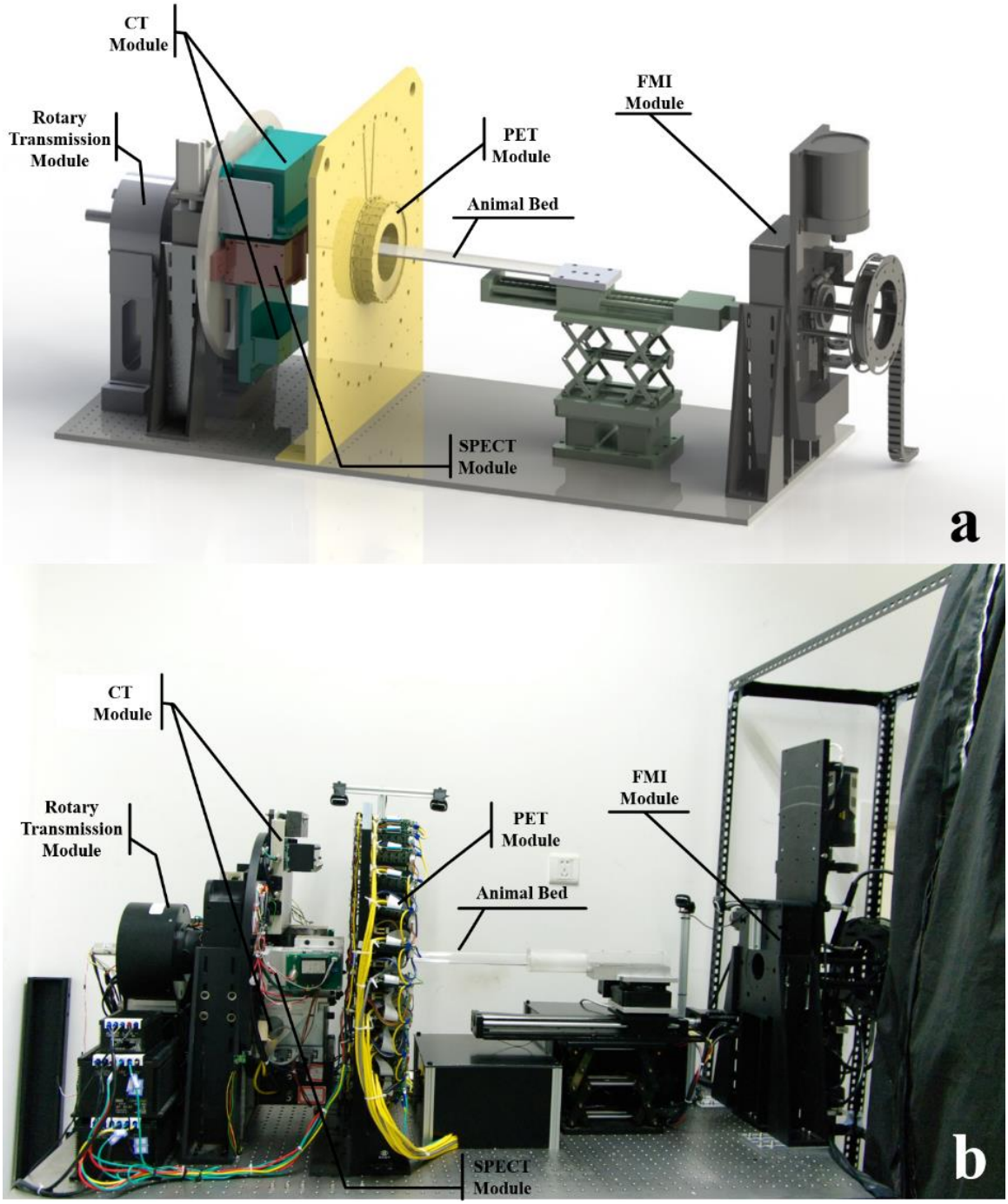

Figure 1.3 – Integration of the Quad-modality imaging system. (a) Draw of quad-modality imaging system, which consisted of the PET, CT, SPECT and FI imaging modules. (b) Photograph of the quad-modality imaging system, which can be setup on an optical table. Reprinted from Lu et al [78] with permission. Copyright © 2014 Society of Nuclear Medicine and Molecular Imaging, Inc.

Another important aspect of the multi-modality imaging comes from a surge in research and technology developments of novel molecular probes [65]. For molecular imaging research, the rise in multi-modality probes has sparked great desires for new technologies in research on multi-modality instrumentation development to measure multiple molecular targets simultaneously or in immediate sequence during the same session. In this condition, several multi-modality imaging systems have been developed for multi-probe imaging that might offer many advantages for preclinical studies [55, 56, 58, 60, 61, 63].

In these multi-modality imaging systems, SPECT, PET, FI modalities use the idea of tracers to image physiologic processes in vivo and the CT modality provide anatomic information for co-registration. While PET and SPECT generally detects high energy gamma rays emitted from radioactive molecular tracers, bioluminescence or fluorescence tracers are traditionally imaged with FMT that detects low energy light (visible or near-infrared light). SPECT permits to use many tracers and biomarkers, which can image a lot of physiologic processes. In contrast with SPECT, PET has the advantages of high sensitivity and temporal resolution, but permits small number of isotope tracers and generally gives metabolic information. FI has high sensitivity and specificity, but low spatial resolution and imaging quality that caused by tissue scattering has limited its applications. These functional imaging modalities have their respective pros and cons but can complement and consult each other. For instance, although PET has high sensitivity in metabolic information but sometimes difficult to differentiate the inflammatory response versus cancer's process, with optical tracers and SPECT tracers, which although have low spatial contrast and low sensitivity respectively, however with the fusion imaging that can

give the complementary information, significantly improve the specificity. It can be harness to more comprehensive information that performing several different molecular probes to detect the same site in immediate sequence during the same session, several critical but complementary biomedical information can give more accurate understanding of the process. Thus, to combine two or three of these functional imaging modalities providing complementary information is a worthwhile goal.

Several articles [50, 51, 57, 67, 75, 76] have discussed the feasibility and potential opportunities of combining the PET-SPECT and radiology-optical imaging modalities, and recommended to use these kind of strategies in biomedical research. Yet so far none of such this imaging system that combines all the three functional imaging modality of PET, SPECT and FI has been developed. Considering this, in this paper we proposed a strategy about tetra-modality molecular imaging that combines PET, SPECT, FI, and X-ray CT modalities for molecular imaging research. Specifically, PET, SPECT and FI modalities provide functional information in different aspects, and CT modality plays a vital role of providing anatomical data as structural reference.

The quad-modality imaging system used modular design, i.e., PET, CT, SPECT and fluorescence molecular tomography (FMT) modalities were designed and manufactured separately. A line-type X-ray detector with a helical scan mode was used in the CT module and a design of a rotary transmission module. On the same rotating plate with CT, SPECT system was installed (as seen in Figure 1.3), which has two gamma cameras anti-parallelly opposed to increase the axial field of view (FOV) of SPECT that can cover the whole-body area of most mice. The gamma camera has a 22 × 22 cerium doped lutetium-yttrium oxyorthosilicate (LYSO) scintillator array coupled to a Hamamatsu H8500 position

sensitive multi-anode photomultiplier tube (PS-PMT) by optical silicone oil. It took 10 - 20 minutes to finish one SPECT whole-body imaging of a typical nude mouse. The next individual module is PET, which is a fixed ring that contains 54 silicon photomultiplier (SiPM) based detectors. It takes 30 - 40 minutes to scan a mouse (three or four bed positions). On the end side of the system, a non-contact, full-angle and vertically rotating FMI imaging module was installed. The FMI can carry out not only traditional fluorescence 2D imaging with both epi-illumination and trans-illumination, but also tomographic 3D imaging. It took less than 10 seconds and 10 minutes to complete traditional 2D imaging and tomographic 3D imaging, respectively. In addition, a transparent animal bed was mounted on a high-precision motor-controlled one-dimensional translation stage, which carried the animal from one modality to another automatically. The entire imaging system can be installed on a 900 mm $\times$ 1500 mm optical table (Figure 1.3b).

The PET, SPECT and CT modules were set up on one side of the motor-controlled animal bed, and the FMI module was placed on the other end because that FMI module requires strictly light shielding. The animal bed can be shifted between PET/SPECT/CT imaging and FMI imaging for multi-modality imaging fusion and so that each imaging module can acquire information data precisely with the co-registered animal position. In this way, this design not only achieved a compact multimodality system but also facilitated the shading of radiation and undesired light. Geometric calibration and image co-registration was processed using fiducial markers on the animal holder. The coordinates of the fiducial markers in images acquired were used for the geometrical transformations leading to the fusion of multi-modality images.

1.2.4 Imaging-guided therapy

In the 2009 World Molecular Imaging Congress, the concept of molecular imaging guided cancer surgery was proposed by Dr. Roger Y. Tsien, and a relevant preclinical research was published in 2010, showing a guided resection of tumor tissue in mice by fluorescence microscopy [79]. The first clinical trial of fluorescence imaging guided ovarian cancer surgery was conducted by Leiden University Medical Center in 2011 [80]. Since then, the molecular imaging-guided cancer surgery has become a globally hot area in precision medicine especially cancer research [81-83].

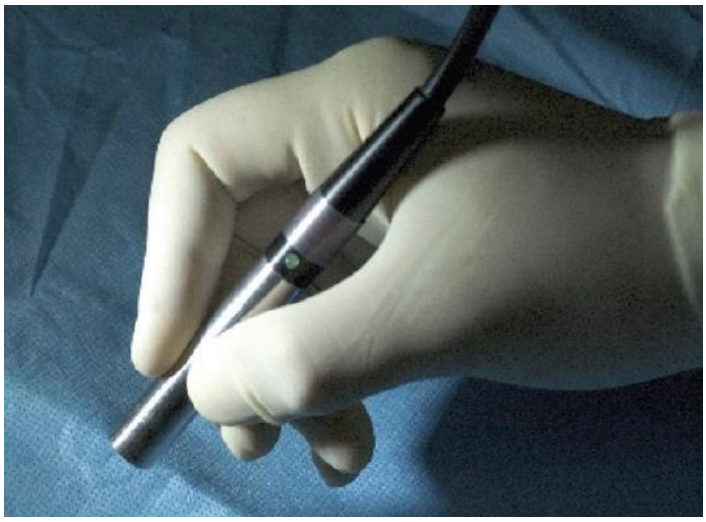

Figure 1.4 – A hand-held spectroscopic device for intraoperative tumor detection. Reprinted from Mohs et al [82] with permission. Copyright © 2010 American Chemical Society.

With imaging guided therapy, surgeons could accurately determine and locate the tumor tissue, especially margin area, thus could significantly increase the possibility of completely removing the entire tumor. As shown in Figure 1.4, a hand-held spectroscopic device for intraoperative tumor detection has been developed by our group [82]. The sensitivity of this real-time imaging is the most important factor for guidance during surgery, since the signal of tumor margin or satellite tumor tissue could be much lower.

Traditional molecular probes for imaging-guided surgery is indocyanine green (ICG), a fluorescent dye being injected intravenously prior to surgery.

1.3 Molecular probes

In molecular biology, molecular probe refers to the labeled deoxyribonucleic acid (DNA) or ribonucleic acid (RNA) used to detect the complementary nucleic acid sequence; while in terms of molecular imaging, the molecular probe refers to the molecules, such as ligands or antibodies, that can specifically bind with the target tissues, to form a compound with molecules that can produce imaging signals (such as isotopes, fluorescein, etc.) in a particular way (as shown in Figure 1.5).

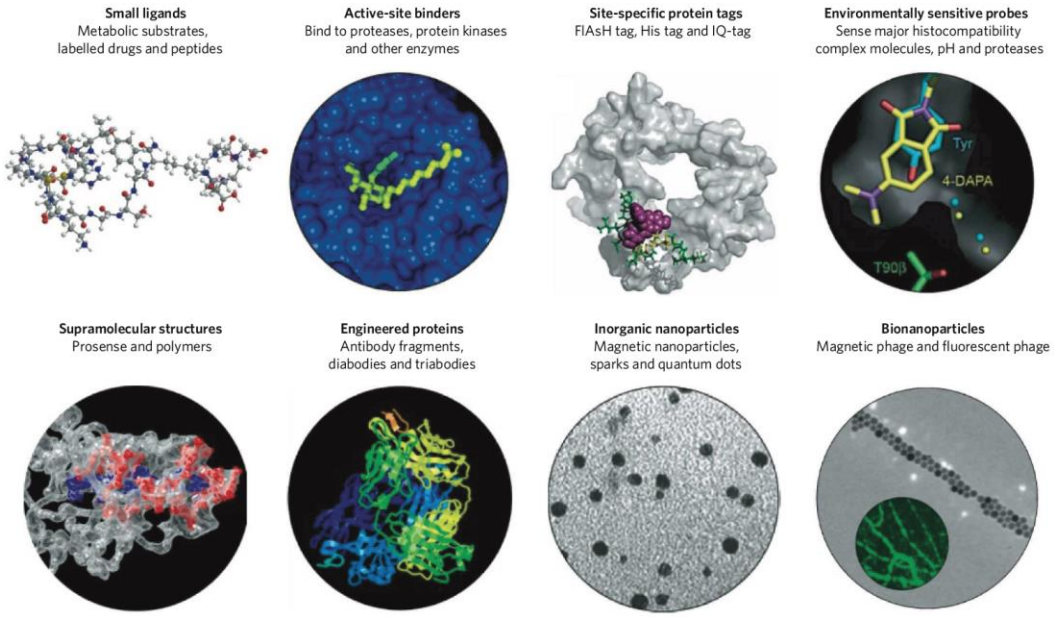

Figure 1.5 – Various types of molecular probes. Reprinted from Weissleder and Pittet [30] with permission. Copyright © 2008 Nature Publishing Group.

With the molecular probe, the molecular and genetic information could be indirectly revealed through the signal change detected by the high-resolution imaging system, based on the principles of targeted binding or enzyme activating [84-107]. The molecular probe

should be able to bind with a specific molecular target in vivo, and provide signal to be detected. Therefore the following three requirements should be met when designing a molecular probe: (1) high specificity and affinity with the target molecule; (2) ability to pass through physiological barriers in vivo and to reach the target cells; (3) high biocompatibility and stability, while participating the relative physiological processes in vivo [71, 73, 108-132].

1.3.1 F-18 ML-10 apoptotic PET imaging

Currently, three types of widely used apoptosis probes are proteins, non-specific small molecules and caspase activation. However, the limitations such as poor specificity, slow blood clearance and immunogenicity etc. impede these probes' clinical applications. An ideal apoptosis probe for clinical practice should be specific for apoptotic cells, with rapid clearance, nontoxic, and high stable [28, 133, 134]. Tc-99m labeled annexin V and F-18 labeled 2-(5-fluoropentyl)-2-methyl malonic acid (F-18 ML-10) are the only two clinically available radiotracers for apoptotic imaging, and the latter is the only probe for PET imaging. ML-10 is derived from the Aposense family apoptotic biomarker. F-18 ML-10 (as shown in Figure 1.6), a low-molecular mass (molecular weight = 206) PET apoptotic tracer derived from Aposense family, is the first clinically available apoptosis probe for in vivo imaging.

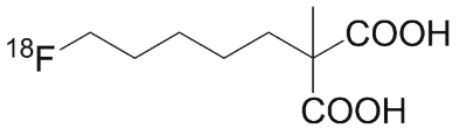

Figure 1.6 – F-18-labeled 2-(5-fluoropentyl)-2-methyl malonic acid (F-18 ML-10).

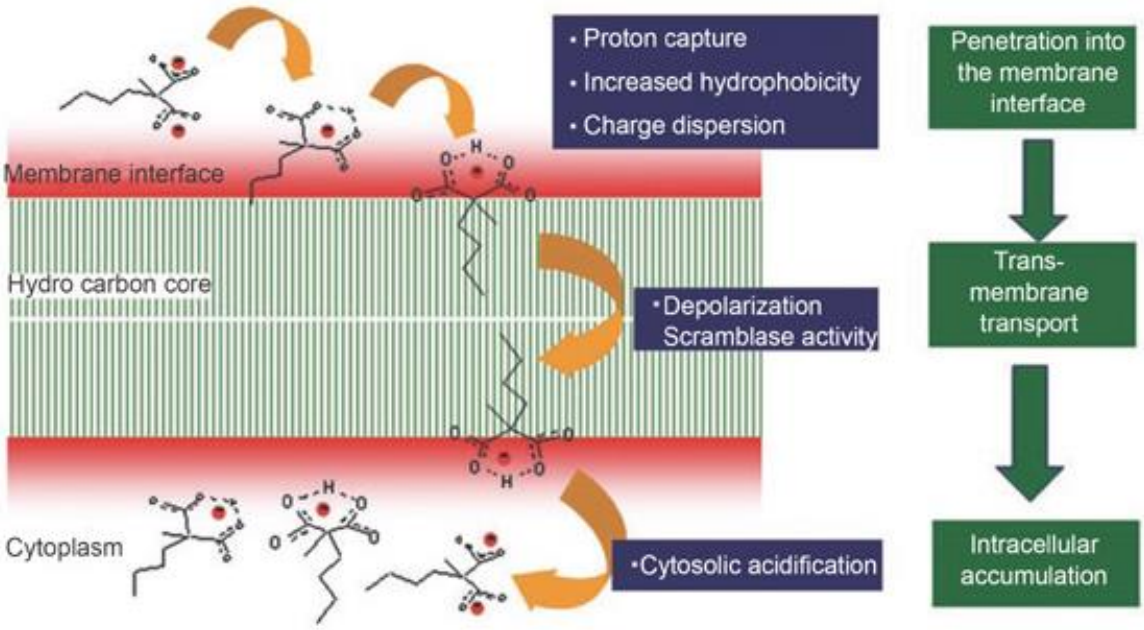

Figure 1.7 – Mechanism for ML-10 uptake by apoptotic cells. Reprinted from Cohen et al [135] with permission.

Being investigated in multi-center preclinical and clinical trials, F-18 ML-10 shows high stability, safety, specificity, and rapid biodistribution [22, 23]. As a probe to visualize cell apoptosis in vivo, F-18 ML-10 selectively accumulates in apoptotic cells by recognizing alterations on the surface of apoptotic cells [19, 20], thus the apoptotic cells could be distinguished from normal cells. Additionally, F-18 ML-10 could be transported through cytoplasmic membrane in apoptotic cells, whereas there is no F-18 ML-10 membrane transportation in necrotic cells. Aposense compounds are rationally designed to selectively bind and accumulate in cells manifesting apoptosis-specific alterations, collectively designated the apoptotic membrane imprint with following steps [135]:

1. Acidification of the external membrane leaflet due to exposure of phosphatidylserine from apoptotic cells;

2. Permanent membrane depolarization;

3. Irreversible loss of intracellular pH control;

4. Activation of the phospholipid scrambling mechanism while membrane integrity is still preserved.

The concurrence of these apoptotic membrane imprint features marks the commitment point of a cell to the apoptotic death process, thus distinguishing such a cell from its viable or necrotic counterparts F-18 ML-10 manifested selective binding to apoptotic cells, high stability, and a favorable biodistribution profile on systemic administration in vivo.

1.3.2 Safety by quality control of F-18 radiopharmaceuticals

Safety is one of the most important aspects for pharmaceuticals to investigate by preclinical and clinical studies before applying to patients. Quality control is an important method to assure the safety of pharmaceuticals. F-18 radiopharmaceuticals are commonly produced by F-18 fluoride labelling via nucleophilic substitution reaction. As shown in Figure 1.8, 4,7,13,16,21,24-hexaoxa-1,10-diazabicyclo (8.8.8) hexacosane (Kryptofix 2.2.2, K2.2.2) is one of the most widely used phase-transfer reagents for F-18 nucleophilic substitution reaction, as well as the main source of chemical impurities in F-18 radiopharmaceuticals. However, the toxicity of K2.2.2 has been revealed by investigation on rodents [136, 137]. As an important quality control requirement, its residue in F-18 fluorodeoxyglucose (F-18 FDG) injection should not exceed 50 μg/mL, required by the United States Pharmacopeia 40 (USP 40) [138] and Chinese Pharmacopoeia (ChP) 2015 [139]. The European Pharmacopoeia (EP) 9.0 [140] proposed a maximum permissible level of 2.2 mg/V as patient dose, which is higher than the threshold set by USP 40 and ChP 2015.

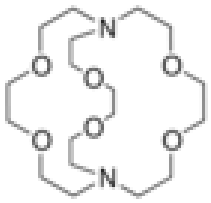

Figure 1.8 – 4,7,13,16,21,24-hexaoxa-1,10-diazabicyclo (8.8.8) hexacosane (Kryptofix 2.2.2).

Currently, a number of methods have been developed to measure the residue of K2.2.2 in F-18 radiopharmaceuticals, such as thin layer chromatography (TLC) [141-144], gas chromatography (GC) [145], high performance liquid chromatography (HPLC) [146, 147], liquid chromatography-tandem mass spectrometry (LC/MS/MS) [148], spectroscopy etc. Among them, the iodoplatinate staining spot test on TLC, described by Mock BH and Colleagues [143], has been adopted by Chinese Pharmacopoeia 2015 and European Pharmacopoeia for the detection of K2.2.2 in F-18 FDG [139, 140]. This is a great step in quality control of F-18 radiopharmaceuticals in China. In previous version of Chinese Pharmacopoeia, the proposed method was spectrophotometry. As the minimum volume for spectrophotometry was 0.3 mL, it was impossible to do the quality control prior to injection. Therefore, the retrospective quality control was required. In current version of Chinese Pharmacopoeia, the spot test method has been adopted. With the spot test, only 3 μL is required for the detection. Therefore, the quality control can be conducted prior to injection, which could better assure the safety of radiopharmaceuticals. However, as other tertiary amine can also react with the iodoplatinate reagents on the silica gel plate [149], such interference could result in a false-positive or false-negative reaction [143, 150]. Therefore, the amine's interference to the result has been considered as a limitation of the application of the spot test [143, 151].

1.4 Research objectives

The goal of this thesis is to investigate the assessment of radiotherapy of cancer by F-18 ML-10 apoptosis imaging. In this dissertation, I hypothesize a method to early assess the safety and efficacy of radiotherapy by apoptosis imaging. In the safety assessment, this method monitors subsidiary injury from exposure of irradiation by measurement of apoptosis change in adjacent tissue outside tumor area. In the efficacy assessment, this method monitors early apoptosis change in tumor area, to predict the tumor shrinkage in several months.

The apoptotic cells and normal cells have been classified by F-18 ML-10 clinical imaging, to validate the following unsolved scientific problems:

1. The interference on K2.2.2 detection in F-18 pharmaceuticals synthesis via spot tests remains unclear.

2. With the lag effect of conventional assessments, the early response after radiotherapy is hard to be assessed which might result in a delay or loss of chance for alternative treatments.

3. It is a challenge to quantitative assessment of apoptosis response of intracranial tumor early after radiotherapy.

4. Although F-18 ML-10 apoptosis imaging has been applied in some case reports [9, 19, 20, 22], the application of the assessment for lung cancer early after radiotherapy has not been reported.

In other related works included in this dissertation, the tumor tissue and inflammatory tissue have been distinguished by preclinical quad-modality imaging with novel probes, and the sensitivity of real-time intraoperative imaging for surgery guidance to distinguish the tumor tissue and normal tissue has been investigated.

Therefore, I started to investigate the safety and quality control of F-18 ML-10 in the synthesis process, to reveal the mechanism of interference in K2.2.2 detection in F-18 radiopharmaceuticals synthesis via spot tests.

CHAPTER 2. QUALITY CONTROL OF F-18 ML-10

As an F-18 radiopharmaceutical, F-18 ML-10 is commonly produced by F-18 fluoride labelling via nucleophilic substitution reaction. K2.2.2 is one of the most widely used phase-transfer reagents for F-18 nucleophilic substitution reaction, as well as the main source of chemical impurities in F-18 radiopharmaceuticals. The removal and detection of K2.2.2 residue in F-18 ML-10 is important in synthesis and quality control process. However, false-positive or false-negative results curb the accuracy of K2.2.2 detection. Although amines have long been considered as the main cause of false-positive or false-negative results of K2.2.2 detection by spot tests, this chapter suggests instead that it is the pH of the sample solution that produces the false-negative results. It is also shown that such interference cannot be attributed to the presence of amines. Commonly used reagents' interference in the detection of K2.2.2 by spot tests was also determined in this chapter. Through testing reagents and stabilizers that are commonly utilized in the process of synthesis of F-18 radiopharmaceuticals, ascorbic acid was found to interfere in the spot test, resulting in a false-negative result.

2.1 Introduction

F-18 radiopharmaceuticals are commonly produced by F-18 fluoride labelling via nucleophilic substitution reaction. K2.2.2 is one of the most widely used phase-transfer reagents for F-18 nucleophilic substitution reaction, as well as the main source of chemical impurities in F-18 radiopharmaceuticals.

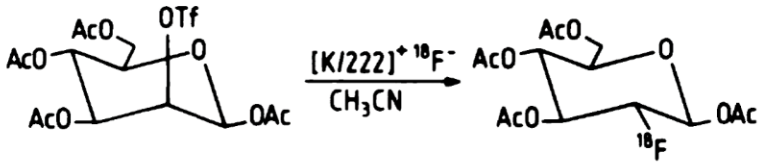

Figure 2.1 – K2.2.2 as the catalyst in F-18 pharmaceuticals synthesis. Reprinted from Hamacher et al[152] with permission.

As shown in Figure 2.1, in the process of synthesis of F-18 radiopharmaceuticals, the 1,3,4,6-tetra-O-acetyl-2-O-triflate-beta-D-mannopyranose were utilized as a precursor, and the K2.2.2 was also added as a phase-transfer catalyst[152]. Due to the toxicity of K2.2.2 [136, 137], its residue in F-18 fluorodeoxyglucose (F-18 FDG) injection should not exceed 50 μg/mL, required by the United States Pharmacopeia 40 (USP 40) [138] and Chinese Pharmacopoeia (ChP) 2015 [139]. The European Pharmacopoeia (EP) 9.0 [140] proposed a maximum permissible level of 2.2 mg/V as patient dose, which is higher than the threshold set by USP 40 and ChP 2015.

Currently, a number of methods have been developed to measure the residue of K2.2.2 in F-18 radiopharmaceuticals, such as thin layer chromatography (TLC) [141-144], gas chromatography (GC) [145], high performance liquid chromatography (HPLC) [146, 147], liquid chromatography-tandem mass spectrometry (LC/MS/MS) [148], spectroscopy etc. Among them, the iodoplatinate staining spot test on TLC, described by Mock BH and Colleagues [143], has been adopted by Chinese Pharmacopoeia and European Pharmacopoeia for the detection of K2.2.2 in F-18 FDG [139, 140]. However, as other tertiary amine can also react with the iodoplatinate reagents on the silica gel plate [149], such interference could result in a false-positive or false-negative reaction [143, 150]. Therefore, the amine's interference to the result has been considered as a limitation of the application

of the spot test [143, 151]. In our experience of quality assurance of F-18 pharmaceuticals, however, the presence of amine occasionally leads to false-negative results, but not leading to false-positive results, by spot test. Here, we investigated the amine's contribution to the iodoplatinate staining spot test for K2.2.2 detection by a semi-quantitative method. Furthermore, as the stabilizer has also been reported leading to a false-negative result [150], we also investigated the interference from stabilizers and other reagents commonly used in the synthesis of F-18 FDG.

2.2 Results and discussion

2.2.1 Detection limit of K2.2.2 by iodoplatinate staining spot test

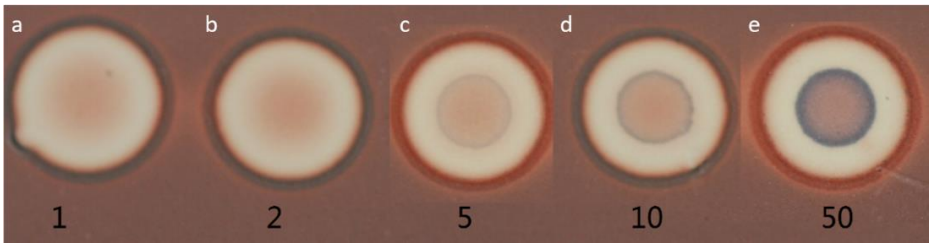

Figure 2.2 – Visualization of K2.2.2 at concentrations of 1 μg/mL (a), 2 μg/mL (b), 5 μg/mL (c), 10 μg/mL (d), and 50 μg/mL (e). The inner dark bluish circles represent the visualization of K2.2.2.

Two concentric circles can be visualized on the silica gel plate, after applying 3 μL droplet of K2.2.2 at certain concentration. As depicted in Figure 2.2, the outer circle, with brown color, represents the solvent; whereas the darker one, innermost bluish circle, is from K2.2.2. The spot with highest concentration of K2.2.2 is shown in Figure 2.2e, and the dark bluish circle is clearly visible by naked eye (Figure 2.2e). With further dilution, from 50 to 1 μg/mL (Figure 2.2a – e), the intensity of dark bluish circle decreased accordingly. Finally, the signal of dark bluish circle cannot be detected by digital camera

at 2 μg/mL (Figure 2.2b). Therefore, the detection limit of K2.2.2 by this method is 5 μg/mL (Figure 2.2c).

2.2.2 Amine's interference on spot test for K2.2.2 detection

Two concentric circles can be visualized on the silica gel plate, after applying 3 μL droplet of 50 μg/mL K2.2.2 on it. As depicted in Figure 2.3a, the outer circle, with brown color, represents the solvent, while the darker one, innermost bluish circle, is the signal from K2.2.2.

With this spot test, the interference from each amine-containing sample could be analyzed by comparing the color and intensity of the dark bluish circular signal from spot B and C. As the spot C is from K2.2.2 standard solution, the color and intensity of this dark bluish circular signal in spot C could be considered as the reference of K2.2.2 without any interference. By visually comparing the color and intensity of K2.2.2's signal in spot B with spot C, the amine's interference to the spot test in each sample could be determined.

In the result from NBS, iminodiacetic acid, EDTA, DTPA, and choline, the signal in spot B is with the same color and intensity as spot C, suggesting that the amine in sample solution did not interfere the result. However, as shown in Figure 2.3b, no dark-bluish circle spot could be observed from DMEA's spot B, and the color of innermost circle changed to yellowish. Besides, as shown in Figure 2.3c, the intensity of the circular signal from tetrabutylamine was lighter than the reference. As the color and intensity of signal in spot B is different from reference, indicating that these amines in sample solution could

make interference on the spot test. Furthermore, as the color and intensity is less intense than reference, there could be a false-negative result from DMEA and tetrabutylamine.

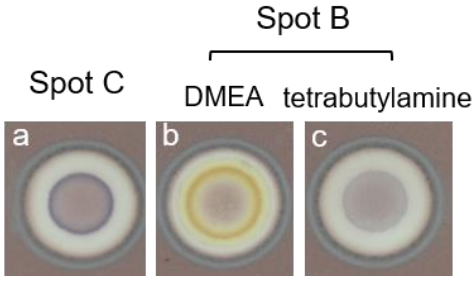

Figure 2.3 – K2.2.2 reference signal in spot C (a) and K2.2.2 signal in Spot B from DMEA (b) and tetrabutylamine (c).

Moreover, since spot A is from sample without mixed with K2.2.2 solution, the possible interference leading to false-positive result could be determined by the visualization of dark bluish circle in sample solutions in spot A. By the test on 7 different kinds of amine solutions in this study, no dark bluish circle could be observed in spot A. Besides, their intensities of signals from spot B were not higher than reference in spot C. Therefore, it is suggested that the presence of 7 kinds of amines does not lead to false-positive results, but DMEA and tetrabutylamine may interfere with K2.2.2 detections by leading to a false-negative result.

To elucidate why DMEA and tetrabutylamine interfere with K2.2.2 detection, while the other five amines do not interfere significantly, the pH of the sample solutions was measured. The result revealed that the pH of DMEA and tetrabutylamine were higher than 12.0, while the other amine samples are with a neutral pH (pH = 7.0). This result indicates that the pH may contribute to the false-negative results. To further investigate the interference of amines without the contribution of pH, the sample solutions of DMEA and tetrabutylamine were neutralized to pH=7.0 by citric acid prior to the spot test. It was

interesting to find that the color and intensity of their spot B were the same as that of the reference in spot C, like other amines with pH=7.0. Therefore, the results indicate that the presence of other amines in sample solutions does not contribute to the false-negative result of K2.2.2 detection, but that the cause may be the change of pH.

2.2.3 Interference from the pH

To investigate the interference from pH, spot tests on non-amine samples with pH ranging from 1.0 to 11.5 has been performed. The samples are 0.1 mol/L hydrogen chloride (HCl, pH=1.0), 0.1 mol/L trisodium phosphate (TSP, pH=7.5), 0.1 mol/L $NaHCO_3$ (pH=8.2), and 0.1 mol/L trisodium citrate (pH=11.5).

As the result from spot A, no dark bluish circle was observed in those samples, suggesting that the change of pH does not lead to false-positive results. However, the results from spot B were not consistent: spot B's signals from HCl and TSP were the same as K2.2.2 reference in spot C, while that signal from $NaHCO_3$ was lighter than reference, even no signal was observed in spot B from trisodium citrate. As a result, HCl (pH=1.0) and TSP (pH=7.5) do not interfere with the spot test, but $NaHCO_3$ (pH=8.2) and trisodium citrate (pH=11.5) cause the false-negative result. Taking the result from amine test into consideration, it is confirmed that the alkali pH causes the interference, and a false-negative result can be generated when the pH in sample solution is greater than 8.0.

2.2.4 Interference from stabilizers commonly used in F-18 FDG synthesis

As widely used radiolytic stabilizers, ethanol and ascorbic acid are usually added in the process of synthesis of F-18 FDG to reduce the self-decomposition of

radiopharmaceuticals [153-155]. In this study, the interference from these common radiolytic stabilizers has been investigated by testing 0.1% ethanol and 10 mg/mL ascorbic acid with neutral pH via spot test. The results of spot A and B from 0.1% ethanol did not show any significant change in color or intensity, suggesting that the presence of ethanol does not interfere with the spot test. As for test on 10 mg/mL ascorbic acid, however, the color of spot A changed to yellowish, as shown in Figure 2.4a. Moreover, the dark bluish circle could not be observed in spot B. By pH measurement, the sample solution is neutral (pH=7.0). Therefore, the presence of ascorbic acid is most likely to be related to the false-negative result.

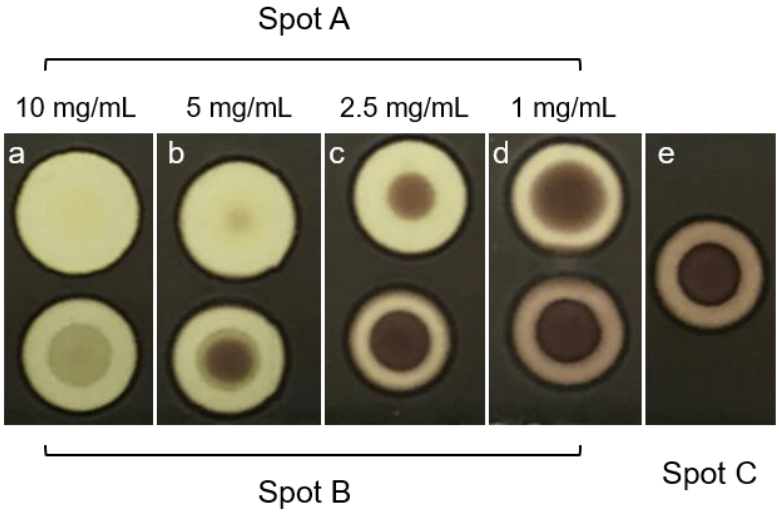

Figure 2.4 – The interference from different concentrations of ascorbic acid.

Furthermore, the ascorbic acid sample solution has been diluted to 5, 2.5, and 1.25 mg/mL to investigate the relationship between the interference and the concentration of ascorbic acid in the solution. As depicted in Figure 2.4, the intensity of the yellowish color is reduced with the decrease of ascorbic acid's concentration, while the signal of dark bluish circle grows more intense in spot B. As shown in Figure 2.4d, the intensity and color

of dark bluish circle in spot B becomes the same as reference when the concentration of ascorbic acid is 1.25 mg/mL. Therefore, the ascorbic acid in sample solution could also lead to a false-negative result. Such interference could be neglected when the concentration of ascorbic acid is as low as 1.25 mg/mL.

As ascorbic acid is a reductant, the staining reagent may be discolored by its reducibility. To testify this hypothesis, the interference from another reductant $SnSO_4$ has also been tested via spot test. Same results were found as shown in Figure 2.5. The dark bluish circle cannot be observed in spot B from samples of saturate $SnSO_4$ in 10% H_2SO_4, and $SnSO_4$ in water. Therefore, it is confirmed that the ascorbic acid, as a commonly used radiolytic stabilizer, could generate false-negative results of iodoplatinate staining spot test, and the reducibility of ascorbic acid is the reason of the discolor of spot on iodoplatinate silica gel plate.

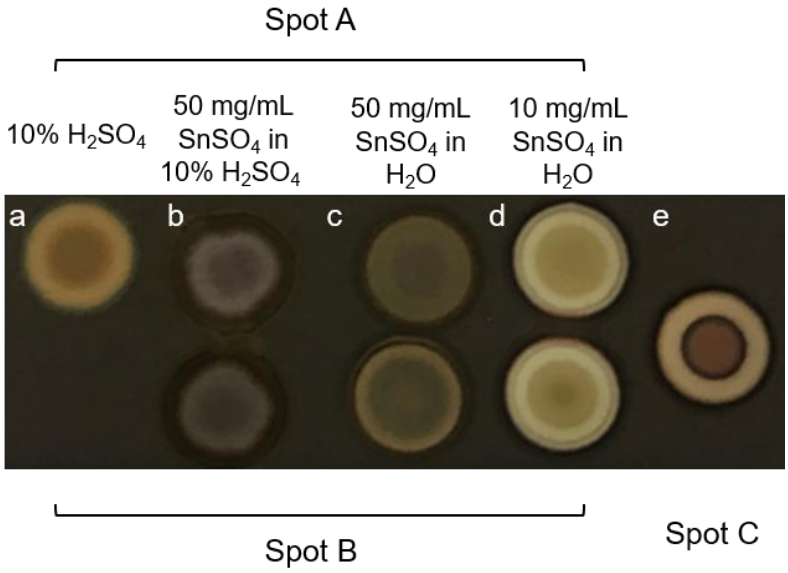

Figure 2.5 – The interference from different concentrations of $SnSO_4$: The dark bluish circle cannot be observed in spot B from samples of saturate $SnSO_4$ in 10% H_2SO_4, and $SnSO_4$ in water.

2.2.5 Interference from reagents for F-18 FDG synthesis

Sodium citrate buffer solution (pH=6.0) and 1,3,4,6-tetra-O-acetyl-2-O-triflate-beta-D-mannopyranose in acetonitrile are main reagents used in the F-18 FDG synthesis. By the interference test, no dark bluish circle was observed in spot A, and the signal in spot B from each sample is the same with K2.2.2 reference in spot C, suggesting that these reagents do not make interference to the spot test.

Besides, samples of liquids from IC-H, Al_2O_3, C-18 separation column, and from Dowex-50 resins in empty column were also collected and tested by interference experiments. Similarly, no interference has been observed from the results.

2.2.6 System suitability of iodoplatinate staining spot test

To investigate the system suitability of Iodoplatinate Staining Spot Test, silica gel plates from different companies (Macherey-Nager and Whatman) were used and compared for K2.2.2 detection at three concentrations (50, 10, and 5 μg/mL). As a result, silica gel plates from both companies can perform accurate detection of K2.2.2. Meanwhile, the K2.2.2 obtained from ABX and Huayi Technology Co., Ltd. has also been compared, resulting in a consistent detection outcome. Furthermore, we compared the detection of K2.2.2 in F-18 FDG produced by three different synthetic routes that uses K2.2.2. The residue of K2.2.2 in F-18 FDG synthesized by HCl hydrolysis[156], liquid phase alkaline hydrolysis[157], and alkaline hydrolysis on solid phase support[158, 159] is 5 – 50 μg/mL, < 5 μg/mL, and < 5 μg/mL, respectively. These results have been confirmed with that resulted from iodine-vapor TLC stain method.

2.2.7 Detection of K2.2.2 in three batches of F-18 radiopharmaceuticals

Samples of three batches of F-18 FDG were also spotted on silica gel plates. For the result from spot A, no dark bluish circle was observed in samples with batch #20150111, #20150114, and #20150105. By the interference test, the signal in spot B from each sample is consistent with K2.2.2 reference in spot C, suggesting that the result of spot A would be accurate. This indicates the concentration of K2.2.2 in these three batches of F-18 FDG is lower than 5 μg/mL. These results have been verified by TLC stain method[142].

K2.2.2 is the most commonly used phase transfer catalyst for F-18 nucleophilic substitution reaction, and there is usually certain residue in the F-18 radiopharmaceuticals. Thus, the detection of K2.2.2 residue is an essential analysis for quality control. The 36th version of US Pharmacopeia[138] adopts iodine-vapor TLC stain method for K2.2.2 detection. With this method, the sample is separated by developing agent, therefore getting rid of the interference reagents. A high specificity could be achieved by this method. However, the procedure of this method is complicated and time consuming, and large sample size (0.1 mL for spotting) needed[160]. UV-Vis spectrophotometry is also used for K2.2.2 detection, but it takes long time and large amount of sample (0.5 mL for spotting). [160] More importantly, it was reported with poor specificity for K2.2.2 detection because of the interference from reagents.[161] The European Pharmacopoeia 9.0 version [140] and the Chinese Pharmacopoeia 2015 version [139] adopt Iodoplatinate Staining Spot Test for K2.2.2 detection, and there are also limitations for the application of this method. K2.2.2 can react with tertiary amine [149], thus leading to a false-positive or false-negative result. If the intensity of K2.2.2 signal exceeds the threshold, it would be necessary to validate the

result by iodine-vapor TLC stain method. Therefore, it is important to test the specificity of Iodoplatinate Staining Spot Test, prior to apply to routine quality control.

Results in this study suggest that reagents or fluids from separation columns commonly used in F-18 FDG synthesis do not make interference to the detection of K2.2.2 by Iodoplatinate Staining Spot Test. The results also indicate that Iodoplatinate Staining Spot Test is superior to UV-Vis spectrophotometry for K2.2.2 detection as quality control in the procedure of F-18 FDG production. Among the amine samples we tested in the interfering study, the presence of DMEA and tetrabutylamine significantly interfere with K2.2.2 detections, leading to a false-positive result. However, the presence of non-amine in alkaline condition (i.e., pH>8.0) also led to the false-positive result. The result of pH measurement shows that the pH of DMEA and tetrabutylamine are greater than 12.0. As a result, the interference is not likely due to the presence of amine, but relative with the pH condition. Therefore, the specificity of Iodoplatinate Staining Spot Test is high when pH<8.0.

Additionally, the sensitivity of Iodoplatinate Staining Spot Test has also been investigated in this study. The actual detection limit of K2.2.2 by this method is 5 μg/mL, which is slightly less sensitive than Mock BH and colleagues' claim (2 μg/mL)[143]. Such difference in detection limit may come from the difference concentration of K_2PtCl_6 and KI used for pretreatment of the silica gel plate. This sensitivity is adequate for K2.2.2 detection, as the maximum permissible level of K2.2.2 residue is 50 μg/mL, required by the Pharmacopoeia [138-140].

The system suitability of Iodoplatinate Staining Spot Test has been investigated by comparisons of different silica gel plates, K2.2.2 reagents and F-18 FDG synthetic methods. Confirmed with iodine-vapor stain TLC method, the results of this Iodoplatinate Staining Spot Test are reliable and reproducible.

Based on the results of this study, a rapid K2.2.2 detection protocol is suggested as follows. First, measure the pH of the F-18 FDG injection. When the pH<8.0, apply 3 μL of the injection on iodoplatinate pretreated silica gel plate by micropipette, and observe from the spot. If there is no dark bluish circle, the residue of K2.2.2 does not exceed 5 μg/mL; while if a dark bluish circle can be found, further comparison with reference is needed. When the pH>8.0, neutralize the alkaline in the injection prior to applying K2.2.2 detection.

2.3 Summary

In this chapter, I demonstrate that the interference from reagents commonly used in F-18 pharmaceutical production to spot test of K2.2.2. No false-positive result of spot test for detection of K2.2.2 has been observed with the presence of seven different amines or other reagents commonly utilized in F-18 radiopharmaceutical synthesis. The interference test demonstrated that the false-negative results are not due to the presence of amines or other chemical impurities. However, it was shown that the pH and the presence of ascorbic acid could lead to false-negative results.

The specificity of iodoplatinate staining spot test for K2.2.2 detection has been investigated in this study. The detection of K2.2.2 is not interfered by other chemical impurities. However, the pH should be lower than 8.0, to make an accurate detection. The

lower limit of the detection is 5 μg/mL by this method, which is applicable for the test of K2.2.2 residue in F-18 FDG injection produced by routes of synthesis that uses K2.2.2. Therefore, the iodoplatinate staining spot test is rapid and easy to operate, and sample saving (3 μL versus 0.1 mL) for routine quality control.

2.4 Experimental

2.4.1 Reagents and apparatus

K2.2.2, AR was purchased from ABX GmbH (Radeberg, Germany) and Huayi Technology Co., Ltd. (Jiangsu, China). N, N-dimethylethanolamine (DMEA), choline, and tetrabutylammonium (TBA) aqueous solution (1 mol/L) were purchased from Aldrich Chemical Co. (Milwaukee, WI, U.S.A.). N-bromosuccinimide (NBS), iminodiacetic acid (IDA), ethylenediaminetetraacetic acid (EDTA), trisodium phosphate (TSP), sodium citrate, and sodium bicarbonate were obtained from Beijing Chemical Works (Beijing, China). Diethylenetriaminepentaacetic acid (DTPA) was acquired from Shanghai Reagent First Factory (Shanghai, China). Ascorbic acid was obtained from McGuff Pharmaceuticals, Inc (Santa Ana, CA, U.S.A.). SEP-PAK C-18 column and SEP-PAK Al_2O_3 column were acquired from Waters Corp. (Milford, MA, U.S.A.). IC-H column was obtained from Grace Alltech (Columbia, MD, U.S.A.). Dowex-50 resins were acquired from Bio-Rad Laboratory (Hercules, CA, U.S.A.). 1,3,4,6-tetra-O-acetyl-2-O-triflate-beta-D-mannopyranose was obtained from Huayi Technology Co., Ltd. (Jiangsu, China). $SnSO_4$ was purchased from Xiya Reagent (Chengdu, China). Potassium hexachloroplatinate (K_2PtCl_6) and potassium iodide (KI) were acquired from JK Chemical (Beijing, China). 0.2 mm Polygram® polyester sheets SIL G were obtained from Macherey-Nager (Dueren,

Germany). Flexible plates for TLC, PE Sil G/UV, were obtained from Whatman (Buckinghamshire, UK). Canon EOS 40D with an EF 100 mm f/2.8 USM lens was acquired from Canon (Tokyo, Japan).

2.4.2 Gel plate preparation

Iodoplatinate staining silica gel plate was prepared in accordance with the guidance from Chinese Pharmacopoeia [139]: 3 mL of 100 g/L K_2PtCl_6 solution was diluted in 97 mL of water, then mixed with 100 mL of 60 g/L KI solution. Silica G plates were immersed in this K_2PtCl_6 and KI mixed solution for 5 – 10 seconds, then dehydrated in dark place in room temperature for more than 12 hours.

2.4.3 TLC analysis

Stock standard solution of 100 μg/mL K2.2.2 was prepared in water for injection (WFI). 3 μL of the following solutions were spotted on the iodoplatinate pretreated silica gel plate by micropipette:

Spot A: sample solutions alone;

Spot B: sample solutions mixed with K2.2.2 standard solution in a relation of 1:1 (v/v);

Spot C: 50 μg/mL K2.2.2 solution: 100 μg/mL K2.2.2 standard solution mixed with water for injection (WFI) in a relation of 1:1 (v/v).

The plates were then photographed by the Canon EOS 40D camera 10 min after spotting for visual analysis.

2.4.4 Three batches of F-18 FDG synthesis

Three batches of F-18 FDG were synthesized by solid phase extraction method we reported in previous work[158]. In short, F-18 ion in cyclotron was captured by QMA column, then washed with sodium carbonate solution containing K2.2.2 and dehydrated in tube. The 1,3,4,6-tetra-O-acetyl-2-O-triflate-beta-D-mannopyranose was dissolved in acetonitrile then added to the tube, an intermediate could be produced afterwards. After adsorbed by C-18 column, the intermediate was hydrolyzed by sodium hydroxide (NaOH) solution. After purification by IC-H column, Al_2O_3 column, C-18 column, and sterile membrane, the F-18 FDG injection was produced.

2.4.5 Sample solutions

Sample #1 – #4 are liquid collected from separation column. Sample #5 and #6 are reagents commonly used in the synthesis of F-18 FDG as shown in **Error! Reference source not found.**.

Sample #7 – #13 are different types of amine solution as shown in

Table 2.2. Among them, NBS, IDA, and EDTA are divalent amines; DTPA and DMEA are trivalent amines; choline and TBA are tetravalent amines.

Sample #14 – #17 are non-amine solution with different pH as shown in Table 2.3, with pH ranging from 1.0 to 11.5.

Sample #18 – #22 are radiolytic stabilizer solutions as shown in Table 2.4. Ethanol and ascorbic acid are commonly used stabilizer when synthesizing F-18 radiopharmaceuticals.

Table 2.1 – Sample #1 – #6: reagents commonly used in the synthesis of F-18 FDG and liquid collected from separation column.

Sample ID	Volume	Sample information
Sample #1	2 mL	Wash the IC-H column with 2 mL of WFI, then collect the washing fluids.
Sample #2	10 mL	Wash the Al_2O_3 column with 10 mL of WFI, then collect the washing fluids.
Sample #3	10 mL	Wash the C-18 column with 10 mL of WFI, then collect the washing fluids.
Sample #4	10 mL	Install 1.5 g of Dowex-50 resins into empty column, then wash with 10 mL WFI and collect the washing fluid.
Sample #5	10 mL	10 mL of 0.5 mol/L sodium citrate buffer at pH=6.0.

Sample #6	10 mL	Dissolve 20 mg of 1,3,4,6-tetra-O-acetyl-2-O-triflate-beta-D-mannopyranose with 2 mL of Acetonitrile, then dilute in 8 mL of water.

Table 2.2 – Sample #7 – #13: different types of amine solution.

Sample ID	Concentration	Sample information
Sample #7	1 mg/mL	N-bromosuccinimide (NBS) aqueous solution
Sample #8	1 mg/mL	Iminodiacetic acid (IDA) aqueous solution
Sample #9	1 mg/mL	Ethylenediaminetetraacetic acid (EDTA) aqueous solution
Sample #10	1 mg/mL	Diethylenetriaminepentaacetic acid (DTPA) aqueous solution
Sample #11	1 mg/mL	N, N-dimethylethanolamine (DMEA) aqueous solution
Sample #12	1 mg/mL	Choline aqueous solution

Sample #13	0.1 mol/L	tetrabutylammonium (TBA) aqueous solution

Table 2.3 – Sample #14 – #17: non-amine solution at different pH conditions.

Sample ID	Concentration	Sample information
Sample #14	0.1 mol/L	Hydrochloric acid (HCl), pH=1.0
Sample #15	0.1 mol/L	Trisodium phosphate (TSP), pH=7.5
Sample #16	0.5 mol/L	$NaHCO_3$, pH=8.2
Sample #17	0.1 mol/L	Trisodium citrate, pH=11.5

Table 2.4 – Sample #18 – #22: radiolytic stabilizer solutions with different pH.

Sample ID	Concentration	Sample information
Sample #18	0.1%	Ethanol
Sample #19	10 mg/mL	Ascorbic acid
Sample #20	5 mg/mL	Ascorbic acid
Sample #21	2.5 mg/mL	Ascorbic acid
Sample #22	1.25 mg/mL	Ascorbic acid

CHAPTER 3. F-18 ML-10 IMAGING FOR SAFETY ASSESSMENT OF RADIOTHERAPY

The safety assessment early after treatment is important for disease management, especially for patients with malignant tumor. In last chapter, the application of F-18 ML-10 in assessment of radiotherapy of brain tumor has been investigated. However, there is no report of applying F-18 ML-10 to assess the radiotherapy of lung cancer. In this chapter, a special case for therapeutic assessment on lung cancer is reported. By this case study, the early safety assessment of radiation by the F-18 ML-10 apoptosis imaging has been first applied to lung cancer, and the result of this assessment is consistent with that of traditional evaluation. Furthermore, the side effect of CyberKnife (CK) radiotherapy has also been discussed. However, the apoptosis in heart tissue and aortic arch increased significantly, indicating a damage on heart tissue and smooth muscle in aortic arch by CK treatment. By animal studies, the subsidiary injury in heart tissue after radiation was observed by apoptosis imaging. Therefore, the CK treatment in this case could cause subsidiary-injury of heart tissue, due to a rapid apoptotic response from heart tissue after radiotherapy, and the F-18 ML-10 apoptosis imaging shows the potential to assess and guide the radiotherapy early after therapy and between fractions.

3.1 Introduction

For radiotherapy and chemotherapy, there is always a serious lag effect for the evaluation the therapeutic due to lack of the assessment based on rapid biological response, resulting in a delay or loss of chance for an alternative treatments [12-14].

Molecular imaging visualizes real-time biological process in cellular and molecular level by molecular probes. The development of molecular imaging makes early therapeutic assessment of radiotherapy feasible. As one of molecular imaging methods, apoptotic imaging could evaluate the early therapeutic response by providing dynamic apoptotic information after radiation, because radiotherapy cures cancer mainly by inducing apoptosis [25, 29, 162]. F-18 ML-10, is the first clinically available apoptosis probe for in vivo imaging [135]. The F-18 ML-10 can be transported through cytoplasmic membrane in apoptotic cells, whereas there is no F-18 ML-10 membrane transportation in necrotic cells, providing an imaging tool to distinguish apoptosis from necrosis [27]. Although having been used to assess the outcome of radiotherapy for brain tumor for couple of years [9, 19, 20, 22], the F-18 ML-10 has hardly ever been applied to therapeutic assessment for tumor on other sites.

In this chapter, a special case for therapeutic assessment on lung cancer is reported. By this case study, the application of F-18 ML-10 on lung cancer has been investigated. Furthermore, the side effect of Cyber-Knife (CK) radiotherapy has also been discussed.

3.2 Results and discussion

3.2.1 Subject and image registration

The subject included in this study was 76 years old male with lung cancer, scheduled to undergo CK stereotactic radiotherapy. F-18 ML-10 PET/CT images has been obtained before and 48 hours after the CK radiotherapy. As the patient's position of two scans changed and the lack of feature points in CT, the registration by MIM software gave a poor accuracy.

As a result shown in Figure 3.1, in the subtraction result, the reddish area represents the higher apoptosis, whereas the bluish area represents the lower apoptosis. However, the contour of the body showed reddish, while noisy heterogeneous signal was observed in the lung. Therefore, other method should be used to make a precise registration. In this study, two methods have been used for registration of the images to analyze the change of apoptosis before and after the radiotherapy.

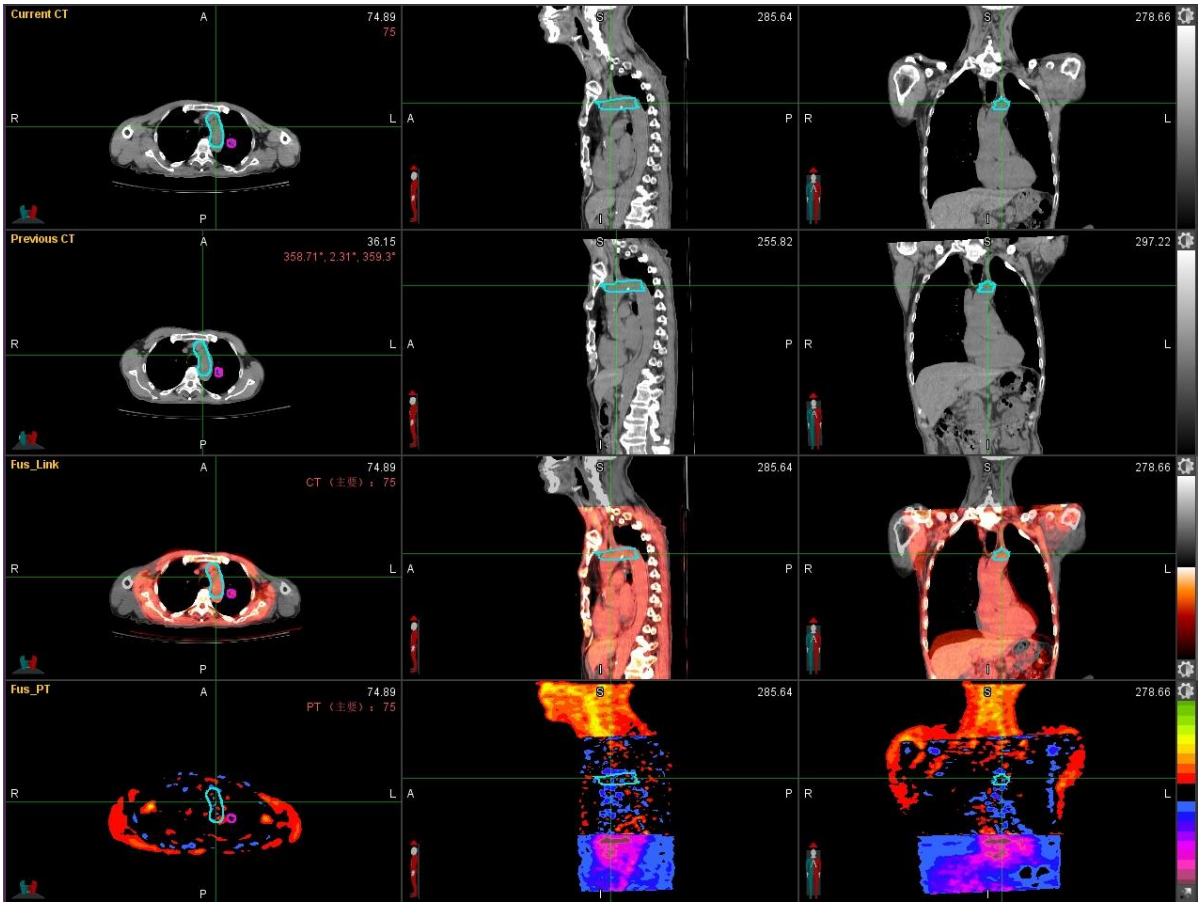

Figure 3.1 – Registration and analysis by MIM 6.6.5 software.

As the PET/CT scanning gives registered PET and CT images for once scanning, we can achieve the registration of PET images by registering their CT images before and after CK radiotherapy. As shown in Figure 3.2, the CT images in each slide has been registered

between the baseline (before CK radiotherapy) and the early therapy assessment (48 hours after CK radiotherapy).

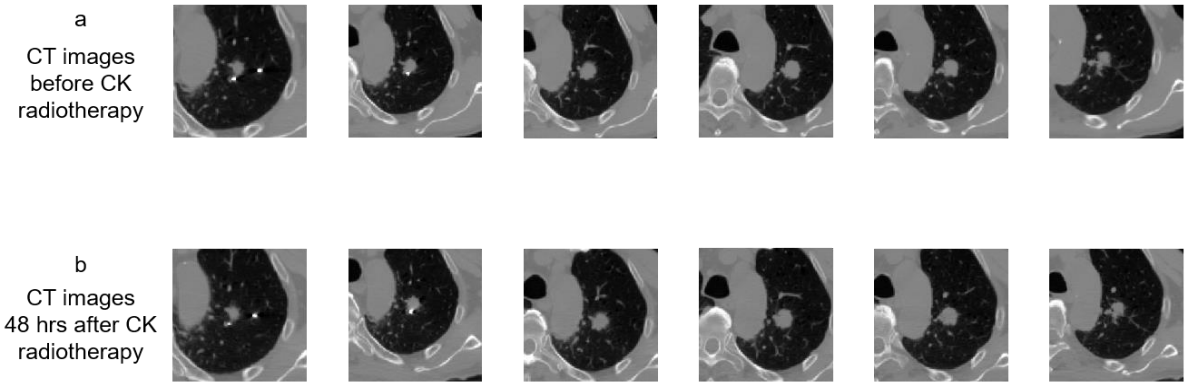

Figure 3.2 – Registration of CT images in each slide before and 48 hours after CK radiotherapy.

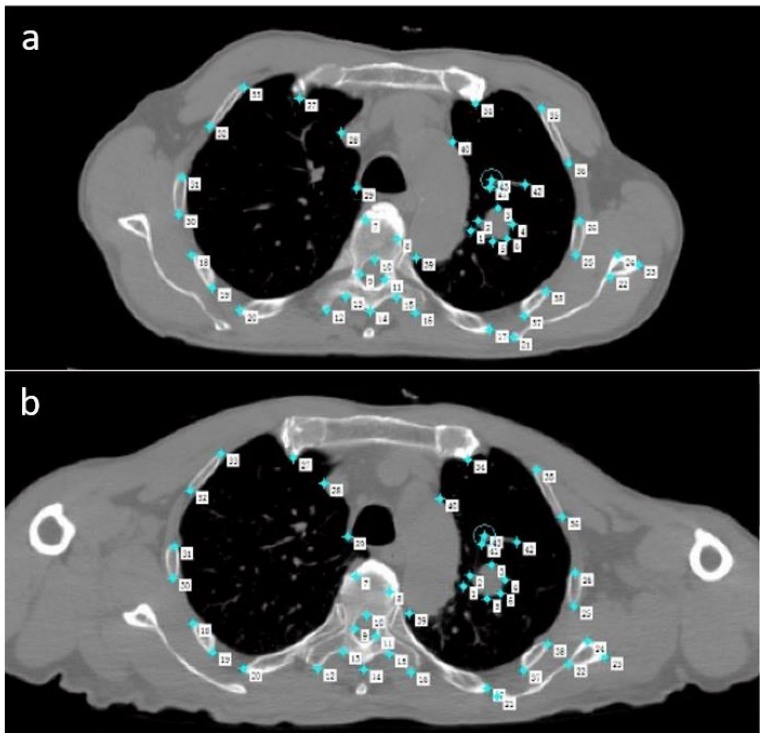

Figure 3.3 – Registration of CT images before (a) and 48 hours after (b) CK radiotherapy with detail features as indicated by cyan stars.

The advantage of this method is that the CT image could give a more accurate registration by detail features (see Figure 3.3), while the PET images cannot reach this high

resolution. However, by this registration method, we need to perform three times registration to get two registered PET images. In specific, the CT images before and after CK should be registered as introduced before, then the PET images would be registered with their own CT images. Finally, the PET images could be registered with the location markers from previous registration. In these processes, the error could be induced in the registrations. At this situation, we also adopted another method for the direct registration of PET images.

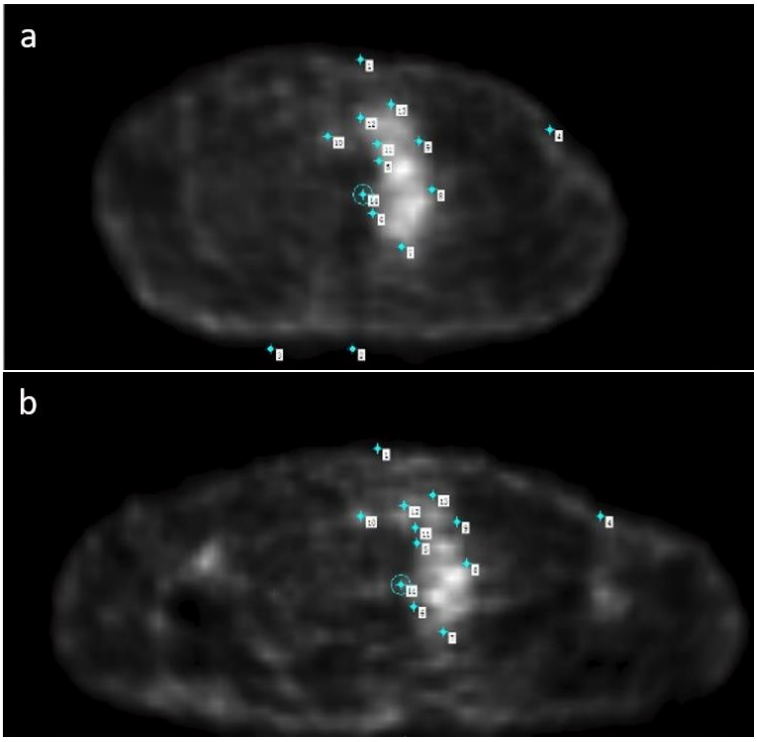

Figure 3.4 – Direct registration of PET images before (a) and 48 hours after (b) CK radiotherapy.

Although the features in PET images are limited comparing with that in CT images, it is sufficient for the registration of PET images, and the accuracy is even higher than the indirect registration we proposed in last paragraph. Therefore, the direct registration of PET

images of different slides has been adopted for the registration of this case. Furthermore, the PET images have been normalized based on the radioactive dosages.

3.2.2 High apoptosis in heart tissue

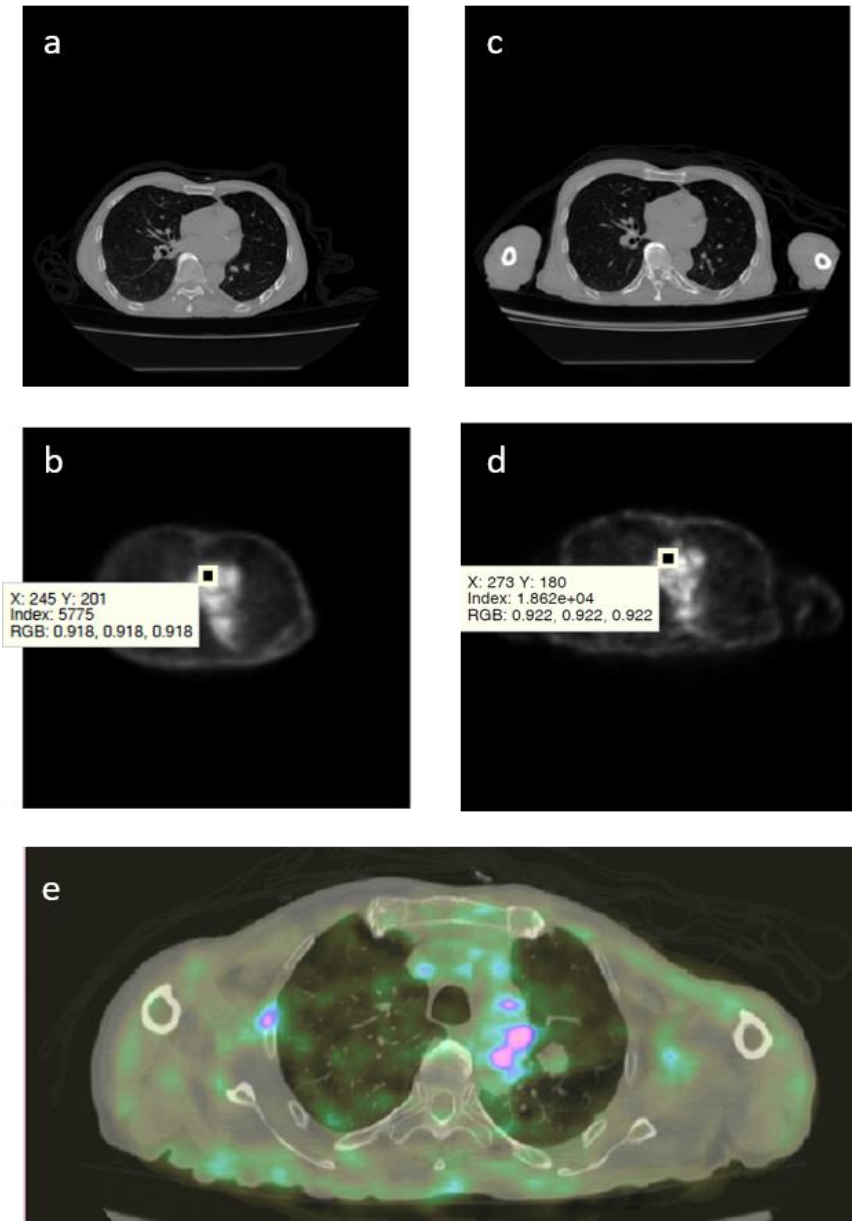

Figure 3.5 – The change in radioactivity from heart tissue before and after CK radiotherapy: (a) CT image before CK; (b) PET image before CK; (c) CT image after CK; (d) PET image after CK; and (e) subtraction of PET images.

By the analysis of the registered PET images before and early after CK radiotherapy, the change of apoptosis activity in the region of interest (ROI) was visualized by the change of radioactivity in the image.

As shown in Figure 3.5, the registration of PET image has been confirmed with the CT image for each slide (see Figure 3.5a and Figure 3.5b). Interestingly, the change in radioactivity from heart tissue overwhelms that from tumor area, as indicated in Figure 3.5c and Figure 3.5d. With the calculation of radioactivity, the apoptotic activity changed to 3.279 times higher after CK therapy, as shown in cyan color area in Figure 3.5e. It is indicated that the heart tissue was damaged by the radiotherapy, while the apoptosis of tumor tissue does not change significant.

3.2.3 Recurrence of lung tumor

By the analysis of apoptosis imaging, the apoptosis of tumor tissue was not significantly changed, indicating that there may not be a rapid response of the tumor after the CK radiotherapy. According to the return visit of the patient one year after the CK radiotherapy, the result showed a recurrence of the tumor in the same site. Therefore, the result of early assessment of the radiotherapy by F-18 ML-10 apoptosis imaging is consistent with the therapeutic assessment one year afterwards.

As shown in the CK treatment plan in Figure 3.6, though it was focused on the tumor in left lung, the heart tissue and aortic arch also received dosage from this therapy. As the aortic arch and heart are usually treated as “blood pool”, the signal could be influenced by the F-18 ML-10 in blood stream. In this study, the PET/CT imaging was scanned 90 minutes after the injection, which is longer than the F-18 ML-10 clearance ratio. Therefore,

the influence of F-18 ML-10 in blood could be eliminated in this study, and the signal are likely from the high uptake of the tissues accordingly. To verify this hypothesis from the results in this case study, an animal study was designed to investigate the subsidiary-injury of heart tissue induced by radiation.

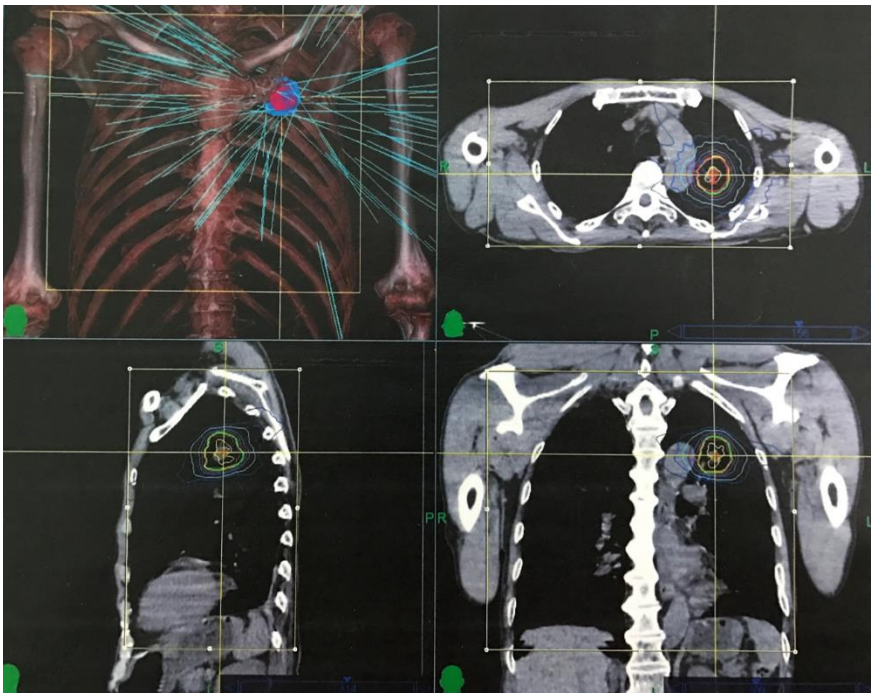

Figure 3.6 – Plan of CK radiotherapy.

3.2.4 Evaluation of subsidiary-injury of lung cancer radiotherapy

To evaluate the subsidiary-injury induced by lung cancer radiotherapy, a rabbit model has been developed according to the CyberKnife plan shown in Figure 3.6. As the detail plan shown in Figure 3.7, the total dose was 50 Gy, and the total fractions are 5, and the bioequivalent dosage was 100 Gy. In the radiotherapy of tumor in lung tissue or adjacent to heart, the heart tissue could receive radiation with dosage higher than 20 Gy in many cases.

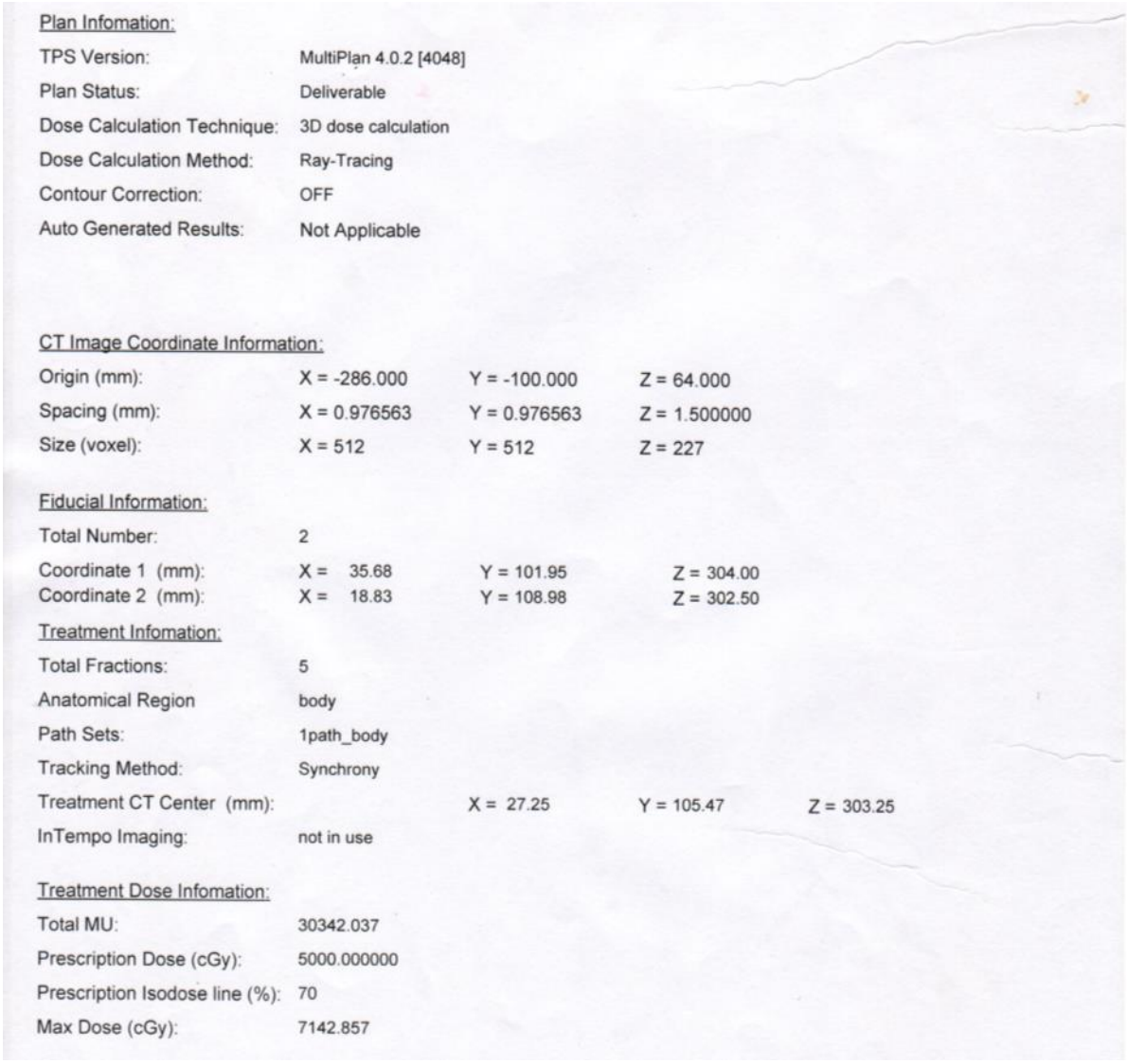

Plan Infomation:

TPS Version:	MultiPlan 4.0.2 [4048]			
Plan Status:	Deliverable			
Dose Calculation Technique:	3D dose calculation			
Dose Calculation Method:	Ray-Tracing			
Contour Correction:	OFF			
Auto Generated Results:	Not Applicable			

CT Image Coordinate Information:

Origin (mm):	X = -286.000	Y = -100.000	Z = 64.000
Spacing (mm):	X = 0.976563	Y = 0.976563	Z = 1.500000
Size (voxel):	X = 512	Y = 512	Z = 227

Fiducial Information:

Total Number:	2		
Coordinate 1 (mm):	X = 35.68	Y = 101.95	Z = 304.00
Coordinate 2 (mm):	X = 18.83	Y = 108.98	Z = 302.50

Treatment Infomation:

Total Fractions:	5			
Anatomical Region	body			
Path Sets:	1path_body			
Tracking Method:	Synchrony			
Treatment CT Center (mm):		X = 27.25	Y = 105.47	Z = 303.25
InTempo Imaging:	not in use			

Treatment Dose Infomation:

Total MU:	30342.037
Prescription Dose (cGy):	5000.000000
Prescription Isodose line (%):	70
Max Dose (cGy):	7142.857

Figure 3.7 – Plan information of CK radiotherapy. Prescription dose was 50 Gy, with 5 fractions.

In this rabbit model, the heart tissue received radiation with different dosage, then F-18 ML-10 imaging was obtained 24 hours after the radiation. Registration of heart tissue has been scanned by CT prior to the radiation, and the setup of the radiation for rabbit is shown in Figure 3.8.

Figure 3.8 – Registration of heart tissue for rabbit radiation.

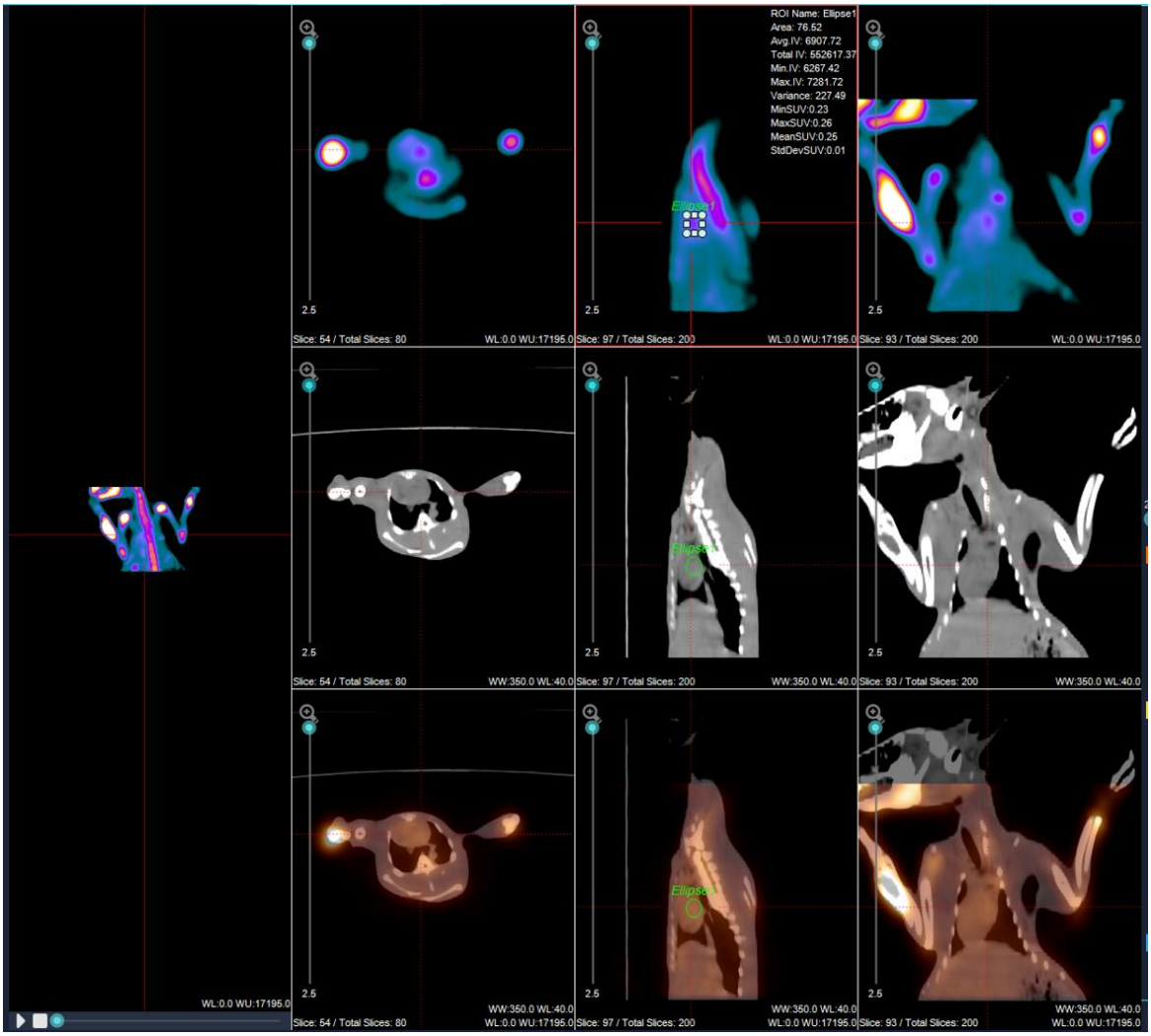

Figure 3.9 – F-18 ML-10 PET/CT imaging of control rabbit (i.e., without radiotherapy). The average SUV in ROI is 0.25.

The result of F-18 ML-10 PET/CT imaging of control rabbit is shown in Figure 3.9. In this PET imaging, the F-18 ML-10 signal from heart tissue has been circled as the ROI. The mean SUV measured in ROI is 0.25. In the control group, the average SUV of five rabbits in control group is 0.22.

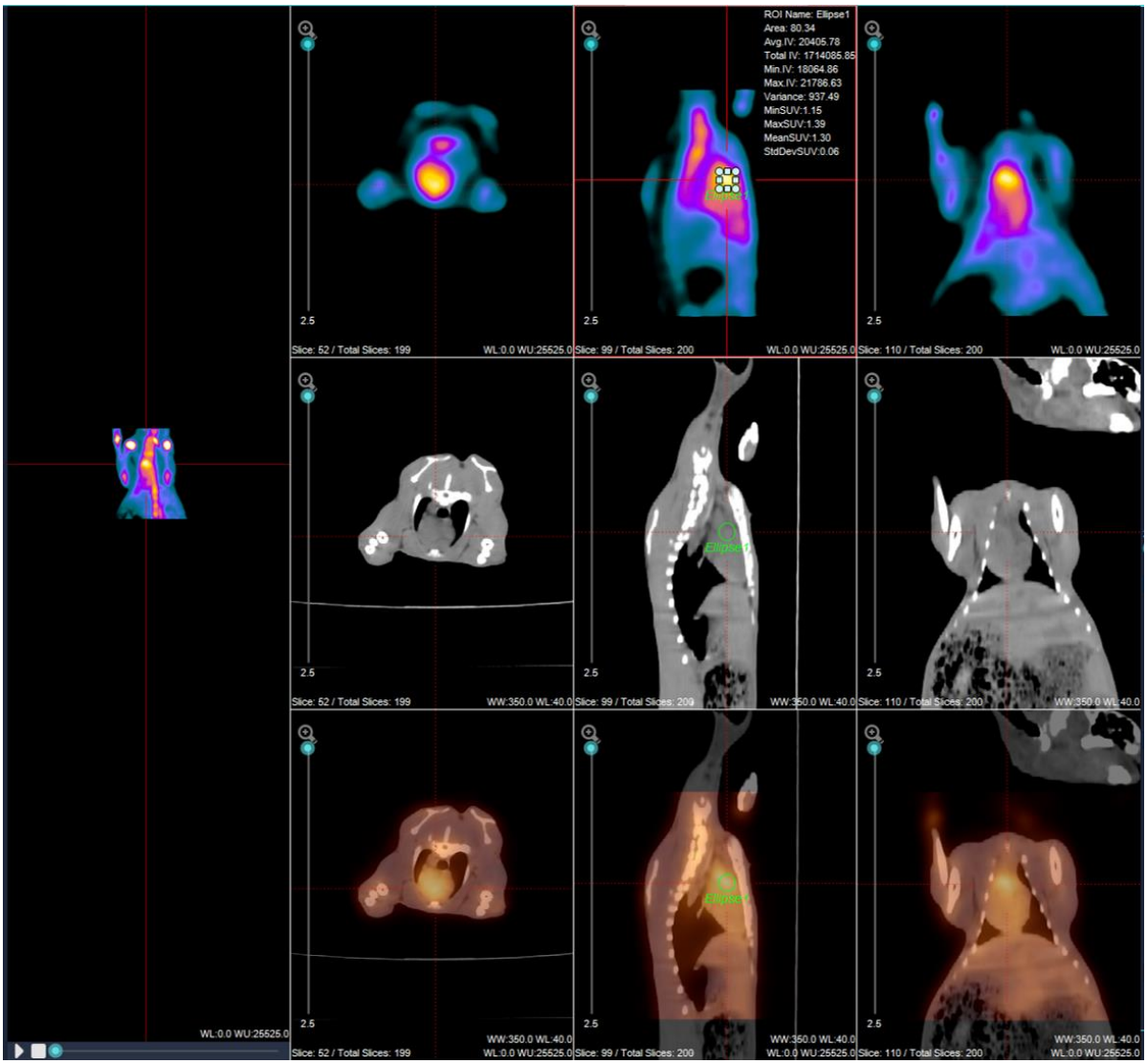

Figure 3.10 – F-18 ML-10 PET/CT imaging of rabbit 24 hours after radiotherapy with 20 Gy radiation. The average SUV in ROI is 1.30.

In one of the experimental groups, the rabbits received 20 Gy radiation, and then scanned 24 hours after radiotherapy. As the result shown in Figure 3.10, the mean SUV in

ROI is 1.30, and the average of two rabbits in this experimental group is 1.24. Comparing with the control group, a very significant increase ($p < 0.01$) of the apoptosis was induced by the radiation of 20 Gy, and such radiation may induce subsidiary-injury of heart by lung cancer therapy by a rapid apoptosis response.

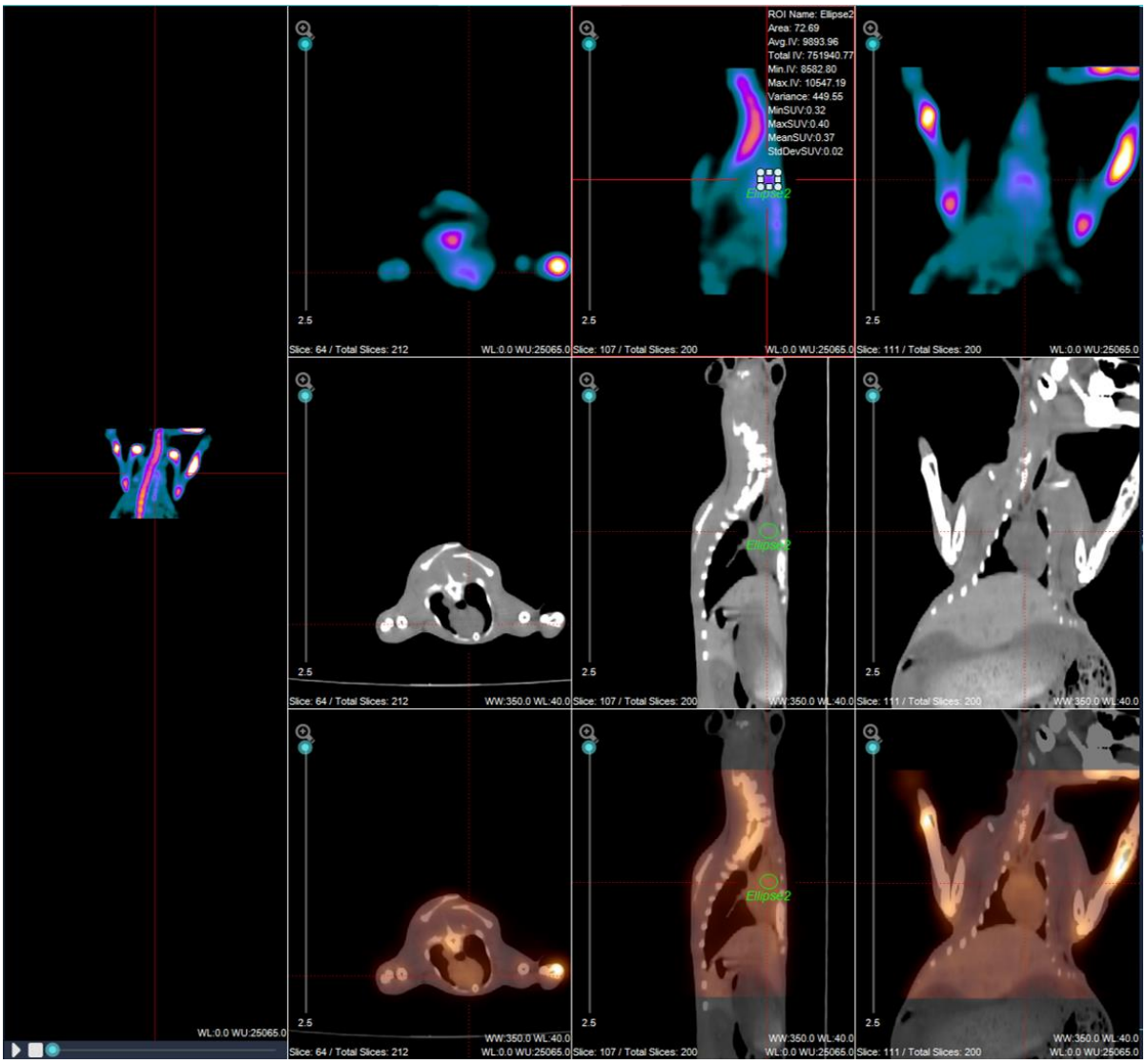

Figure 3.11 – F-18 ML-10 PET/CT imaging of rabbit 24 hours after radiotherapy with 10 Gy radiation. The average SUV in ROI is 0.37.

Moreover, in another experimental group, we decreased the dosage of radiation to 10 Gy, to visualize the change in apoptosis early after the radiation with lower dosage. As

shown in Figure 3.11, the mean SUV in ROI is 0.37 from one of the rabbits 24 hours after 10 Gy radiation, and the average of three rabbits in this experimental group is 0.35. By comparing with the control group, the average apoptosis is higher after the radiation, but no statistically significant difference could be found, $p = 0.10$.

By statistical analysis on the apoptotic change in F-18 ML-10 PET imaging, the result of quantification of the apoptotic change in SUV is shown in Figure 3.12. The signal in ROI from the group of rabbits received 20 Gy radiation became significantly higher than the control group, suggesting that the rapid apoptosis response could be induced in radiotherapy when the dose of heart is as high as 20 Gy. The PET results from rabbits received 10 Gy radiation indicate that 10 Gy radiation on heart tissue may not induce rapid apoptosis in this study.

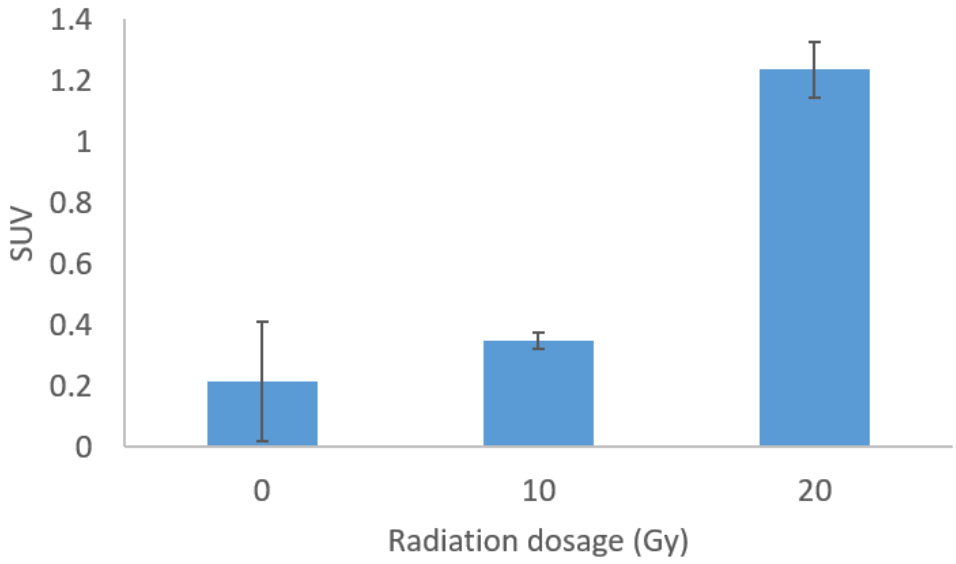

Figure 3.12 – Comparison on SUV of F-18 ML-10 PET imaging after 10 and 20 Gy radiation.

Therefore, the animal study provides more evidence to visualize the subsidiary-injury of lung cancer therapy by F-18 ML-10 PET imaging. Furthermore, the F-18 ML-10 shows its potential to guide the radiotherapy between fractions, by evaluating the apoptosis response and the subsidiary-injury of heart induced by radiation.

3.3 Summary

In this chapter, the early assessment of therapeutic response by the F-18 ML-10 apoptosis imaging has been first applied to lung cancer, and the result of this assessment is consistent with that of traditional evaluation. After CK treatment, there was no significant change in the apoptosis of tumor. However, the apoptosis in heart tissue and aortic arch increased significantly, indicating a damage on heart tissue and smooth muscle in aortic arch by CyberKnife treatment. An animal study provides more evidence to the subsidiary-injury of lung cancer therapy by visualization of apoptosis response from F-18 ML-10 PET imaging. Therefore, this study suggests that CK treatment could cause subsidiary-injury of heart tissue, by inducing a rapid apoptosis of heart tissue after radiotherapy. Therefore, it is suggested to protect the heart tissue from the radiation due to its rapid apoptotic response.

3.4 Experimental

3.4.1 Informed consent and statement of human rights

Informed consent was obtained from all participants. All protocol of this clinical study has been approved by Institutional Review Board of Chinese PLA General Hospital

3.4.2 PET/CT acquisition protocol

PET/CT imaging were performed before and 48 hours after CK therapy with AMIC Ray-Scan 64 PET/CT system (AMIC, Beijing, China), 90 minutes after F-18 ML-10 tracer injection with 0.12 mCi/kg b. w. The F-18 ML-10 tracer was produced at the Department of Nuclear Medicine at PLAGH PET Facility [163] with PET-MF-2V-IT-I Fluorine multifunctional synthesis module (PETKJ, Beijing, China), and the radiochemical purity is of >98% by HPLC.

PET images were acquired by three-dimensional brain mode, with 2.5-mm slice width, 512 × 512 reconstruction matrix. CT images were acquired with a 50-cm field of view (FOV), 75-cm diameter of gantry, 2.5-mm of slice width, 150-cm maximum positioning length, 175-cm axial moving range of patient bed, and 512 × 512 of reconstruction matrix.

3.4.3 CT acquisition protocol

CT images for localization of tumor were acquired on Brilliance TM (Philips healthcare, Amsterdam, Netherland), with an 80-cm maximum field of view (FOV), 60-cm actual FOV, 85-cm diameter of gantry, 1.5-mm of slice thickness, 150-cm maximum positioning length, 190-cm axial range of patient bed, and 1024 × 1024 of maximum reconstruction matrix.

3.4.4 Radiotherapy protocol

CyberKnife which enables stereotactic radiosurgery delivery applied in this study was manufactured by Accuray (Accuray Inc., Sunnyvale, CA, USA). Non-isocentric treatment plan was implemented through accelerator mounted on the robotic arm with continuous real-time image-guided technology.

The blood, urine as well as biochemical examination, electrocardiography (ECG) and chest X-ray was acquired before. After enrolment, patient underwent head CT and MRI scanning for location of tumor. The acquired CT images was co-registered with MRI images by MIM software (version number: 6.5.4), which was imported into CyberKnife Robotic Radiosurgery System (Multiplan 4.0.2) for target and organs at risk delineation. With the information provided by the fused images, the target area of CK treatment was optimized and the gross tumor volume (GTV) was recorded by radiologists and physicians. Patients underwent CK stereotactic radiosurgery with 6D‑skull tracking, and the treatment scheme was with 10 Gy in 5 fractions according to the tumor size and position.

3.4.5 In vivo animal studies

We performed studies on seven 2.8 – 3.0 kg male rabbits. Two rabbits underwent 20 Gy radiation by Elekta Synergy^{TM} S linear accelerator, three rabbits underwent 10 Gy radiation by the same system, while five rabbits are in control group. 3 mCi of F-18 ML-10 was injected via auricular vein 24 hours after the radiation. PET/CT scanning was performed 60 minutes after injection of F-18 ML-10. The protocol of animal study has been approved by Institutional Review Board of Chinese PLA General Hospital.

3.4.6 Statistical analysis

For statistical analysis, two-tail paired Student's t-tests were applied to analyze the change in radioactivity before and after treatment, and $p < 0.05$ was considered as statistically significant.

CHAPTER 4. F-18 ML-10 IMAGING FOR EFFICACY ASSESSMENT OF APOPTOSIS RESPONSE OF INTRACRANIAL TUMOR EARLY AFTER RADIOTHERAPY

As discussed in last chapter, the removal and detection of K2.2.2 in the synthesis process of F-18 ML-10 has been demonstrated. In this chapter, I demonstrate the clinical use of F-18 ML-10 to assess the apoptosis response of intracranial tumor early after CyberKnife (CK) treatment. As F-18 ML-10 is a novel apoptosis molecular probe, limited clinical studies has been investigated on F-18 ML-10. In the clinical use, there are many challenges for quantitative analysis of therapeutic assessment by using apoptotic imaging. As apoptosis is essentially a transient process, it is necessary to standardize the imaging method and time point, and to make quantitative analysis based on "volume-by-volume" of the image, to distinguish between cell apoptosis and spontaneous apoptosis.

In this chapter, a pilot study on 29 human subjects diagnosed with intracranial tumors were included in this study. Clinical data of different types of brain tumor have been collected, and the PET image has been analyzed volume-by-volume in assessment of response of different types of tumors to radiotherapy. Furthermore, correlation between the result of this early assessment and subsequent anatomic change in tumor determined by MRI was also investigated for the further safety and effectiveness assessment.

A positive correlation was observed between the change in F-18 ML-10 uptake in the tumor measured during early treatment and the subsequent change in tumor volume measured after the completion of CK treatment. Malignant tumors tend to be more sensitive to CK treatment, but the treatment outcome is not affected by pre-CK apoptotic status of tumor cells, F-18 ML-10 PET imaging could be taken as an assessment tool within 48

hours after CK treatment. By analyses on the application of this method on different patients, the result indicates that the F-18 ML-10 early assessment may give a more accurate evaluation early after radiotherapy.

4.1 Introduction

Intracranial and central nervous system (CNS) tumors are of high incidence in adolescents (0-19 years). In the U.S., the average age-adjusted incidence is annually 5.57 per 100,000 population from 2008 to 2012, and nearly 700,000 people live with intracranial and CNS tumors [17]. In the past decades, the overall diagnostic rate of intracranial tumor has been raised by the development of diagnostic imaging technologies, such as X-ray computed tomography (CT) and magnetic resonance imaging (MRI). Nowadays, the most common radical cancer treatments are surgery, radiotherapy and chemotherapy. And radiotherapy is an important method for intracranial treatment that could either be a main regiment, or adjuvant therapy after surgery for keeping cancer from recurrence. The evaluation of therapeutic response mainly relies on the change of tumor size assessed by CT and MRI images. For radiotherapy and chemotherapy, however, the anatomical volume change comes later than the rapid biological change on cellular level, resulting in a serious lag effect for the evaluation [9]. Indeed, the anatomical volume change of intracranial tumor is difficult to be visualized by CT or MRI till 4-8 weeks after whole brain radiotherapy [10, 11]. Particularly, for patients with malignant brain tumor, such as high-grade gliomas and metastatic tumors, etc., the average survival time is short. With the lag effect of conventional assessments, the early response after radiotherapy is hard to be assessed which might result in a delay or loss of chance for an alternative treatments [12-14]. Moreover, the tumor tissue and radio-necrotic tissue could not be distinguished by CT and MRI

images, which might cause ambiguous or even wrong judgment of therapeutic effect. Therefore, a method which could offer an early response assessment after radiotherapy for clinical management improvement is required.

Molecular imaging visualizes real-time biological process in cellular and molecular level by molecular probes. The development of molecular imaging makes early therapeutic assessment of radiotherapy feasible. As one of molecular imaging methods, apoptotic imaging could evaluate the early therapeutic response by providing dynamic apoptotic information after radiation, because radiotherapy cures cancer mainly by inducing apoptosis [25, 29, 162]. In the past decade, molecular imaging modalities such as PET/CT, MRI, magnetic resonance spectroscopy (MRS), B- Ultrasound and diffuse optical tomography (DOT), etc. have been developed and widely used. Among these modalities, only PET/CT could accurately provide quantitative information of apoptosis with proper apoptosis probe at molecular level.

Currently, three types of widely used apoptosis probes are proteins, non-specific small molecules and caspase activation. However, the limitations such as poor specificity, slow blood clearance and immunogenicity etc. impede these probes' clinical applications. An ideal apoptosis probe for clinical practice should be specific for apoptotic cells, with rapid clearance, nontoxic, and high stable [28, 133, 134]. F-18 labeled 2-(5-fluoropentyl)-2-methyl malonic acid (F-18 ML-10), a low-molecular mass (molecular weight = 206) PET apoptotic tracer derived from Aposense family, is the first clinically available apoptosis probe for in vivo imaging. Being investigated in multi-center preclinical and clinical trials, F-18 ML-10 shows high stability, safety, specificity, and rapid biodistribution [22, 23]. As a probe to visualize cell apoptosis in vivo, F-18 ML-10 selectively accumulates in apoptotic cells by

recognizing alterations on the surface of apoptotic cells [19, 20], thus the apoptotic cells could be distinguished from normal cells. Additionally, F-18 ML-10 could be transported through cytoplasmic membrane in apoptotic cells, whereas there is no F-18 ML-10 membrane transportation in necrotic cells. Therefore, we are able to distinguish apoptosis from necrosis[27].

In this study, we investigated the performance of early response after CyberKnife (CK) stereotactic treatment on 29 patients with intracranial tumors, through F-18 ML-10 PET/CT imaging with voxel-by-voxel analysis. Furthermore, the correlation between the result of this early assessment and subsequent anatomic change in tumor determined by MRI was also investigated for the further safety and effectiveness assessment.

4.2 Results and discussion

4.2.1 Subjects and lesions information

In this trial, 33 patients aged from 22 to 69 years old, with 34 lesions were included. 29 patients with 30 lesions completed the trial. Among the 30 lesions, there are 12 metastatic neoplasms (in 11 subjects), 6 meningiomas, 3 cavernous hemangiomas, 3 germ cell tumors, 2 hemangiopericytomas, 2 adenoid cystic carcinomas, 1 chordoma, and 1 hypophysoma. The 29 patients who completed the trial were with no radiation-related complication occurred.

4.2.2 Visualization and analysis of apoptotic imaging of intracranial tumor

The result of F-18 ML-10 PET/CT apoptosis imaging (Figure 4.1) shows a high PET signal from spontaneous apoptosis in the lesion area, while the signal in surrounding

normal brain tissue is relatively low. Thus, the location and extent of the tumor could be identified in PET/CT images.

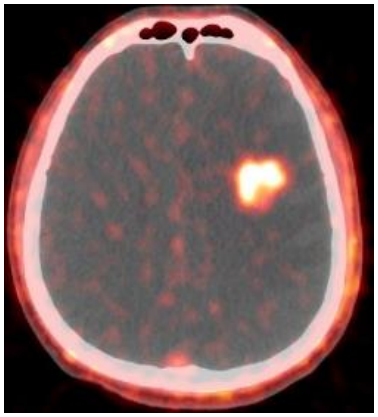

Figure 4.1 – Representative PET/CT F-18 ML-10 image of a male patient, 48 years old, diagnosed with kidney cancer brain metastases, pre-CK.

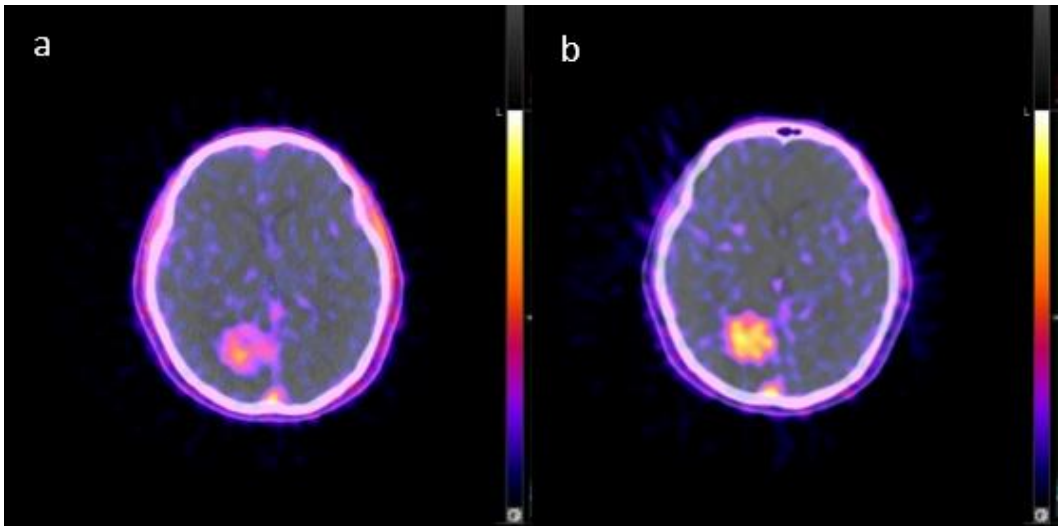

Figure 4.2 – Pre-CK PET/CT image (a) and post-CK PET/CT image (b) of a female patient, 61 years old, diagnosed with lung cancer brain metastases, showing an obvious and uniform increase of F-18 ML-10 uptake

The change in F-18 ML-10 uptake between pre-CK (Figure 4.2a) and post-CK (Figure 4.2b) is analyzed by a voxel-wise method. As shown in Figure 4.2a and Figure 4.2b, the post-CK uptake of ML-10 tracer is clearly higher than pre-CK uptake. In other cases, however, there is obscure difference of F-18 ML-10 uptake between pre-CK (Figure 4.3a)

and post-CK (Figure 4.3b). As clear change in F-18 ML-10 uptake cannot be visualized by the PET/CT images, the subtraction of "post-CK" – "pre-CK" (Figure 4.3c) is processed by MIM software, with a reference of GTV information as the red contour of tumor. With this subtraction analysis shown in Figure 4.3c, a greater change in the F-18 ML-10 was found in the central area of the tumor, rather than the edge, suggesting that there are more apoptotic cells at the center while less apoptotic cells at the edge after CK treatment. In this case, an intuitive and clear change in the apoptotic tumor cells could be visualized by the change in F-18 ML-10 uptake with subtraction of PET images. Moreover, the area with high PET signal corresponded well with the lesions determined by GTV and MRI fused image (Figure 4.3d).

The analysis based on subtraction enables the judgement of whether there is more or less apoptosis happening in ROI after CK treatment feasible. However, the heterogeneous and two-way overall changes of tracer uptake cannot be revealed by subtraction analysis. As shown in Figure 4.4, some portion of the tumor becomes more apoptotic, while the other becomes less apoptotic, and there is unchanged portion remains. Therefore, quantitative analysis of the voxel-based subtraction is needed to further investigate cases with heterogeneous and two-way changes.

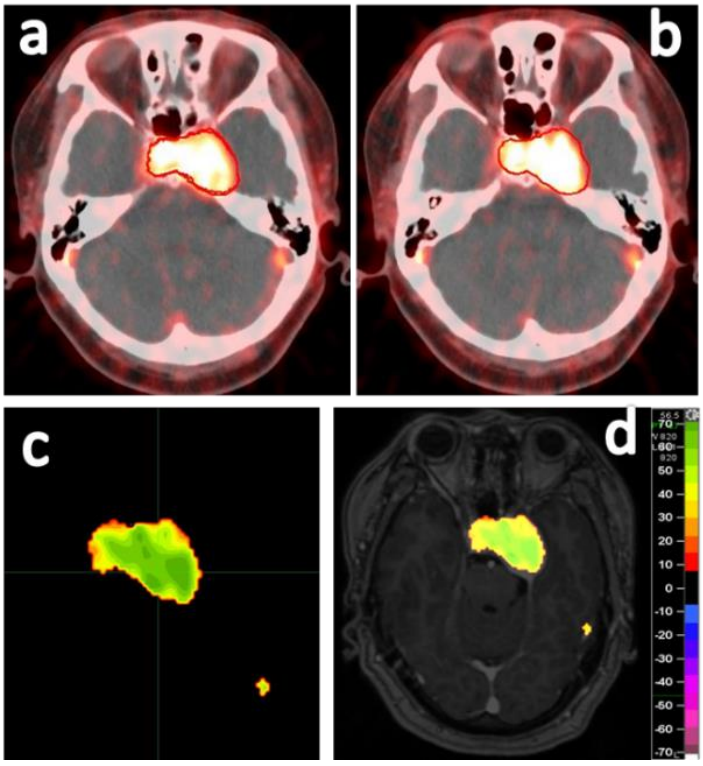

Figure 4.3 – Pre-CK PET/CT image (a), post-CK PET/CT image (b), subtraction (c) of PET image, and fused PET/MRI images (d) of a female patient, 54 years old, diagnosed with Cavernous hemangioma in cavernous sinus. Red line indicates the contour of tumor. The color bar shown in (d) corresponds to radioactivity changing ratio.

4.2.3 Quantitative analysis for accurate subtraction

With the registration and fusion of pre-CK and post-CK PET images, the change in F-18 ML-10 uptake in radioactivity after CK treatment of each voxel in ROI could be extracted and sorted into one of the following three categories: (1) voxels with increased F-18 ML-10 uptake, defined as a positive change in radioactivity of more than 12.5% from pre-CK, representing cells in early apoptosis; (2) voxels with decreased F-18 ML-10 uptake, defined as a negative change in radioactivity of more than 12.5% from pre-CK, representing vascular occlusion and/or clearance of apoptotic cells; (3) voxels without

change in F-18 ML-10 uptake, defined as a change in radioactivity of less than 12.5%. Wherein, the threshold of 12.5% is set in accordance with references [9, 164].

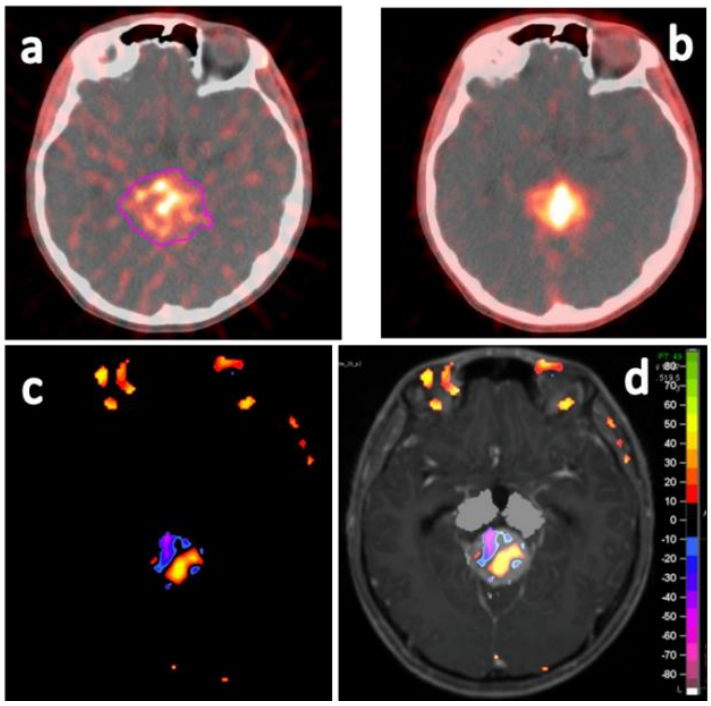

Figure 4.4 – Pre-CK PET/CT image (a), post-CK PET/CT image (b), subtraction (c) of PET image, and fused PET/MRI images (d) of a male patient, 21 years old, diagnosed with germ cell tumor. Color bar shown in (d) corresponds to radioactivity changing ratio. The change in tracer uptake from pre-CK (a) to post-CK (b) is visualized by the subtraction of PET images (c) and PET/MRI images (d).

As the change in apoptosis could not be accurately quantified by average change in radioactivity due to the heterogeneity of tumor tissue, the signal change in each voxel in ROI is plotted into scatter graph (Figure 4.5), with pre-CK's radioactivity on the X-axis, and the post-CK's radioactivity on the Y-axis. Voxels with increased signal are shown in red, representing increased apoptotic activities, voxels with decreased signal are shown in blue, while voxels with unchanged (change less than ±12.5%) signal are shown in green.

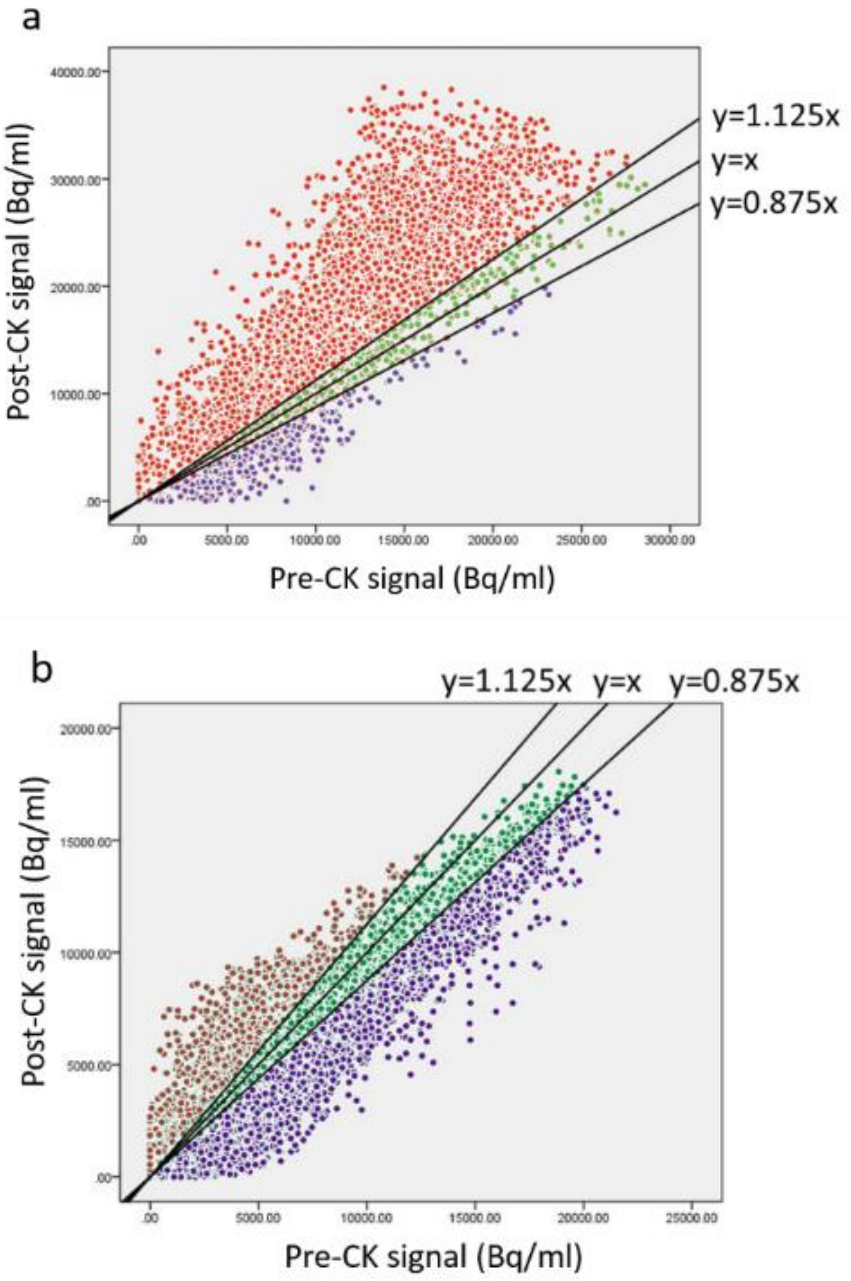

Figure 4.5 – Voxel-based subtraction scatterplots showing the effect of CK treatment in a subject with positive apoptotic response (a) and a subject without significantly apoptotic response (b). The X-axes represent the pre-CK radioactivity, while the Y-axes represent post-CK radioactivity. Voxels with increased signal are shown in red, representing increased apoptotic activities. Voxels with decreased signal are shown in blue, and voxels with unchanged (change less than ±12.5%) signal are shown in green.

The response of radiotherapy could be classified into different types, by the comparison of different subjects' signal changing pattern depicted in scatterplots (Figure 4.5a and Figure 4.5b).The change in tumor size for all 30 lesions from 29 subjects was obtained by MRI 2 to 4 months after CK treatment completion, and the mean percentage of volume change was 30.96%±21.73% (95% CI 22.85% – 39.08%) reduced in tumor size. In the meanwhile, the mean change per voxel was 32.03%±18.40% (95% CI 25.16% – 38.90%). As correlation analysis shown in Figure 4.6, a significant correlation was observed between the change in F-18 ML-10 uptake (X) and subsequent change in tumor volume (Y) with a Pearson correlation coefficient $R = 0.862$, $p < 0.05$. The linear regression equation is: $Y = 1.018 * X - 0.016$. T-test result of the regression coefficient is: $t = 9.010$, $p < 0.05$, and ANOVA result of the regression coefficient is: $F = 81.175$, $p < 0.05$.

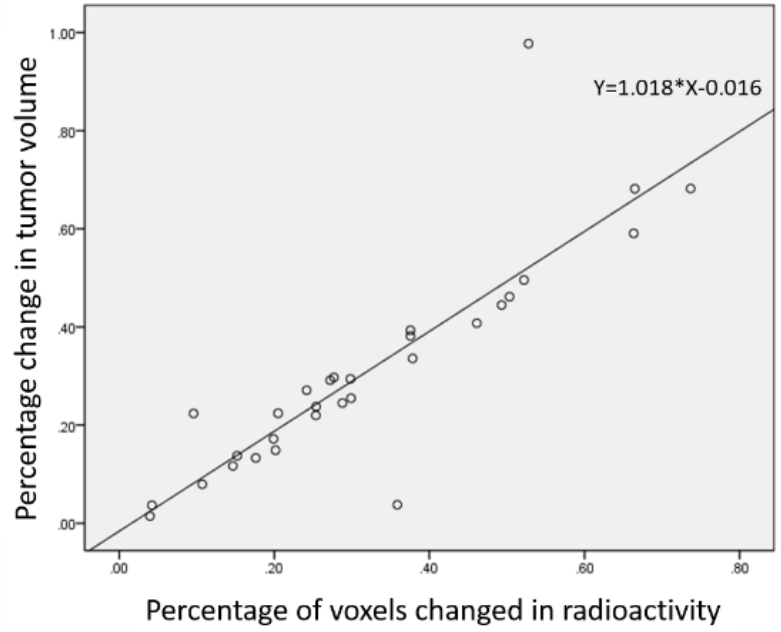

Figure 4.6 – Correlation between the change in F-18 ML-10 uptake (X) and subsequent change in tumor volume (Y). The Pearson correlation coefficient is R = 0.862, p < 0.05.

4.2.4 Comparison of the therapeutic response in different cancer type

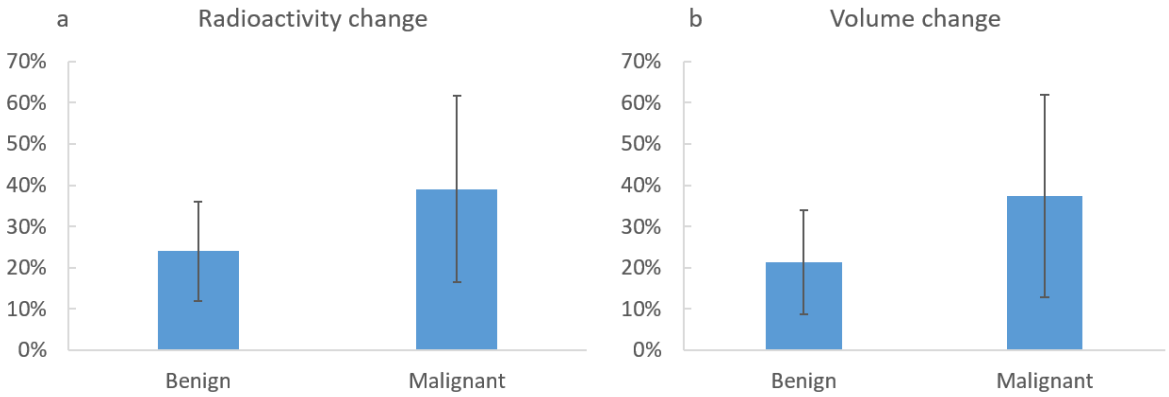

Figure 4.7 – The comparison of therapeutic response in benign and malignant tumors. A significant difference of the radioactivity change (a) between malignant and benign tumor has been observed, p = 0.0258. Furthermore, this difference is confirmed by subsequent volume change (b) with statistical significance, p = 0.0262.

As shown in Figure 4.5a, the number of voxels with increased apoptosis indicated by red spots overwhelms that of decreased and unchanged signal, showing that positive apoptosis has been increased in tumor area by SRS, thus suggests an effective radiotherapy. However, for the other case shown in Figure 4.5b, no significant change in apoptotic signal could be defined as an increase or decrease by the scatterplot result. Therefore, the individual response early after radiotherapy could be revealed by quantitative scatterplot of apoptotic change, especially for heterogeneous change. Moreover, Moffat et al assessed the effectiveness by correlating the early apoptotic change and the subsequent change in tumor volume [164].

In accordance with 2016 World Health Organization's (WHO) classification of CNS tumors, 30 lesions in this study could be classified into 2 groups: 18 malignant and 12 benign tumors. The changes in radioactivity and subsequent tumor volume of each lesion have been analyzed, and the comparison in different cancer type are shown in Figure 4.7.

As depicted in Figure 4.7a, a significant difference of the radioactivity change between malignant and benign tumor has been observed, p = 0.0258. Furthermore, this difference is confirmed by subsequent volume change with statistical significance (see Figure 4.7b), p = 0.0262. Therefore, malignant tumors could be considered to be more sensitive to CK treatment in comparison with benign tumors.

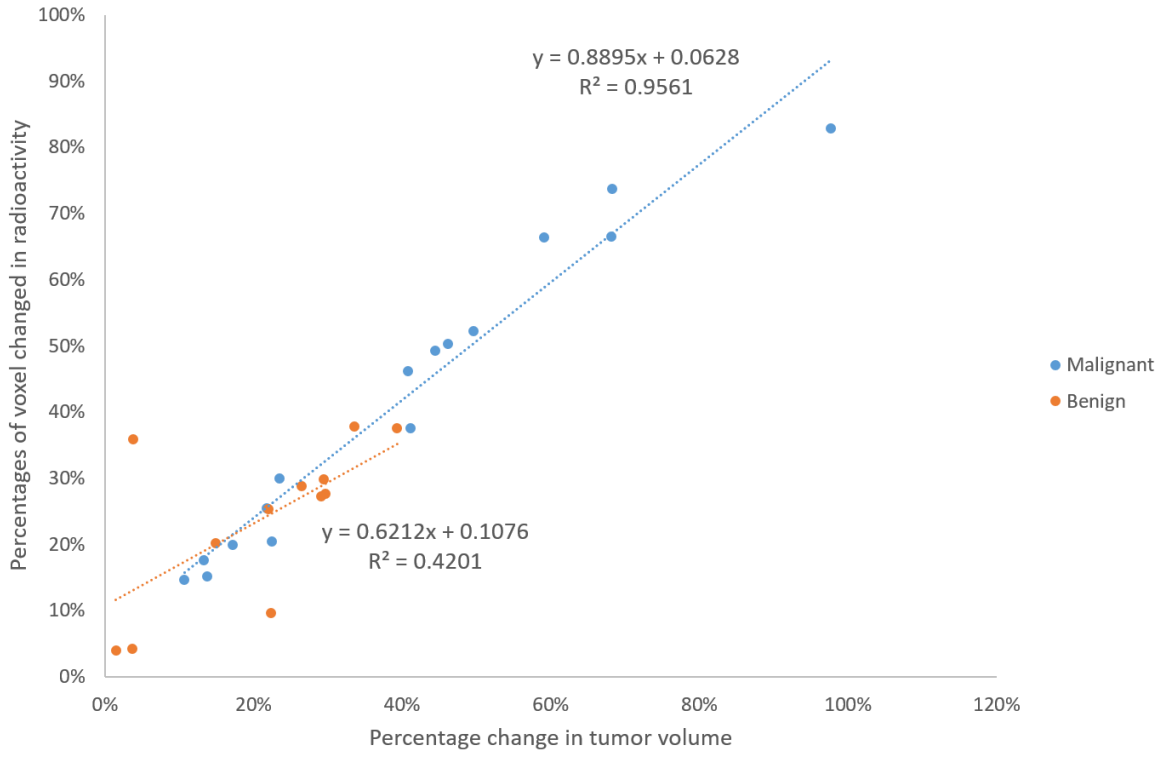

Figure 4.8 – The comparison of the F-18 ML-10 assessment in patients with malignant (blue) and benign (red) tumor. The F-18 ML-10 assessment on patients with malignant shows a better linear correlation between tumor volume change and changes in radioactivity early after radiotherapy.

Furthermore, the analysis on the F-18 ML-10 assessment in patients with malignant (blue) and benign (red) tumor has been conducted. As shown in Figure 4.8, the F-18 ML-10 assessment on patients with malignant shows a better linear correlation between tumor volume change and changes in radioactivity early after radiotherapy. The R square of F-18

ML-10 assessment on malignant tumors is 0.9561, whereas it is 0.4201 for assessment on benign tumors. Therefore, this suggests that malignant tumors are more sensitive to radiotherapy by inducing more apoptosis in the tumor area, and the F-18 ML-10 assessment may give a more accurate evaluation on radiotherapy of patients with malignant tumors.

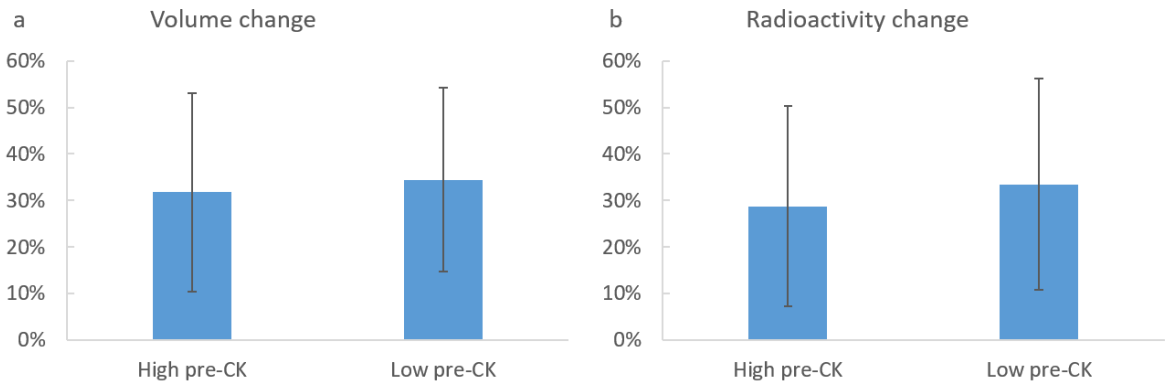

Figure 4.9 – The comparison of therapeutic response in high pre-CK radioactivity and low pre-CK radioactivity tumors. No significant difference in radioactivity change (a, p = 0.5640), or subsequent volume change (b, p = 0.7226) was found between these two groups.

Among all lesions included in this study, there are 16 lesions with high pre-CK radioactivity value, while 14 lesions with lower radioactivity before CK treatment, with the threshold of 10,000 Bq/mL. The comparison of therapeutic response between high pre-CK and low pre-CK groups was conducted. As shown in Figure 4.9a and Figure 4.9b, there is no significant difference in radioactivity change (p = 0.5640), or subsequent volume change (p = 0.7226) between these two groups after CK treatment. Furthermore, the F-18 ML-10 assessment between these two subgroups of patients has been compared as shown in Figure 4.10. Therefore, this suggests that the pre-CK radioactivity does not influence the applicability of F-18 ML-10 assessment method in this study.

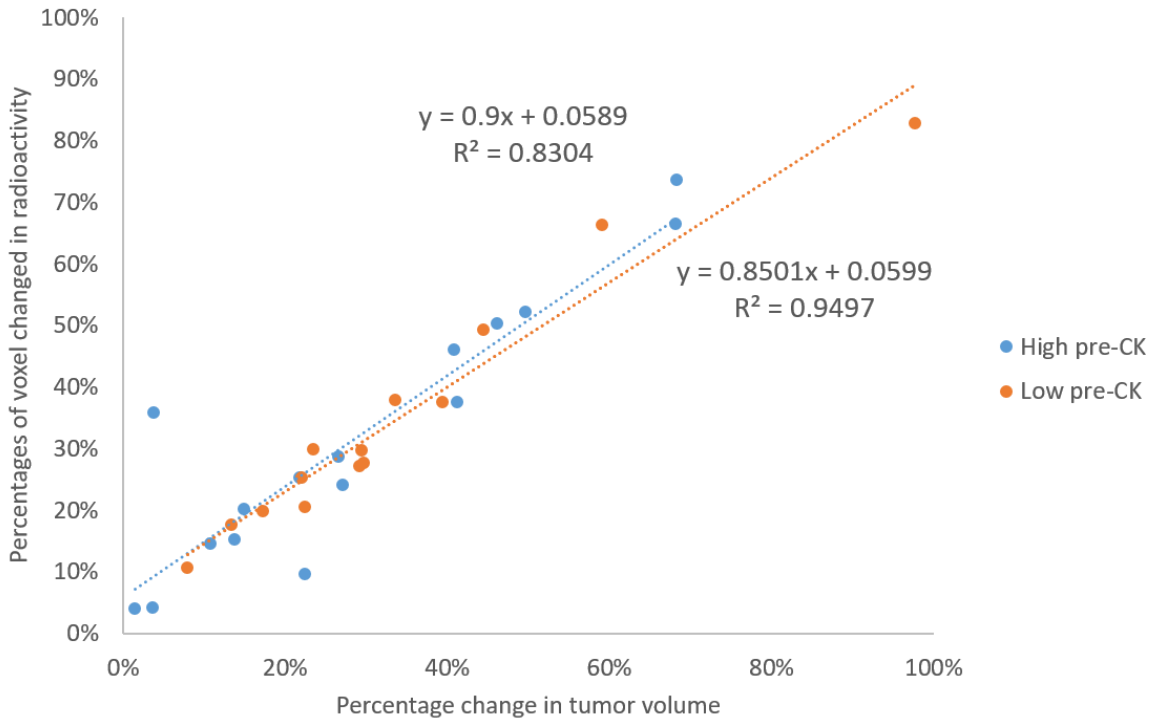

Figure 4.10 – The comparison of the F-18 ML-10 assessment in patients with pre-CK radioactivity higher than 10,000 Bq/mL (blue) and lower than 10,000 Bq/mL (red). The F-18 ML-10 assessment on this two groups of patients does not show significant difference in the linear correlation between tumor volume change and changes in radioactivity early after radiotherapy.

4.2.5 Evaluation on applicability of the F-18 ML-10 therapeutic response by different subgroups of patients

In order to further analyze the applicability of F-18 ML-10 early assessment of therapeutic response for different patients, the distribution of change in radioactivity and volume has been shown in Figure 4.11 a and b, respectively. By this result, no correlation of the therapeutic response could be found in this distribution figure.

Moreover, the patients have been divided into two subgroups aged >50 and ≤50, as shown in Figure 4.12 a and b, respectively. By this analysis, no significant difference could be found between these two subgroups, suggesting that the therapeutic response of patients

is not related to the age in this study. However, by further analysis on the comparison of the F-18 ML-10 assessment in patients aged >50 and ≤50, as shown in Figure 4.13, the F-18 ML-10 assessment on patients elder than 50 years old shows a better linear correlation between tumor volume change and changes in radioactivity early after radiotherapy in this study (R square 0.9778 versus 0.8108). This indicates that the F-18 ML-10 early assessment may give a more accurate evaluation early after radiotherapy.

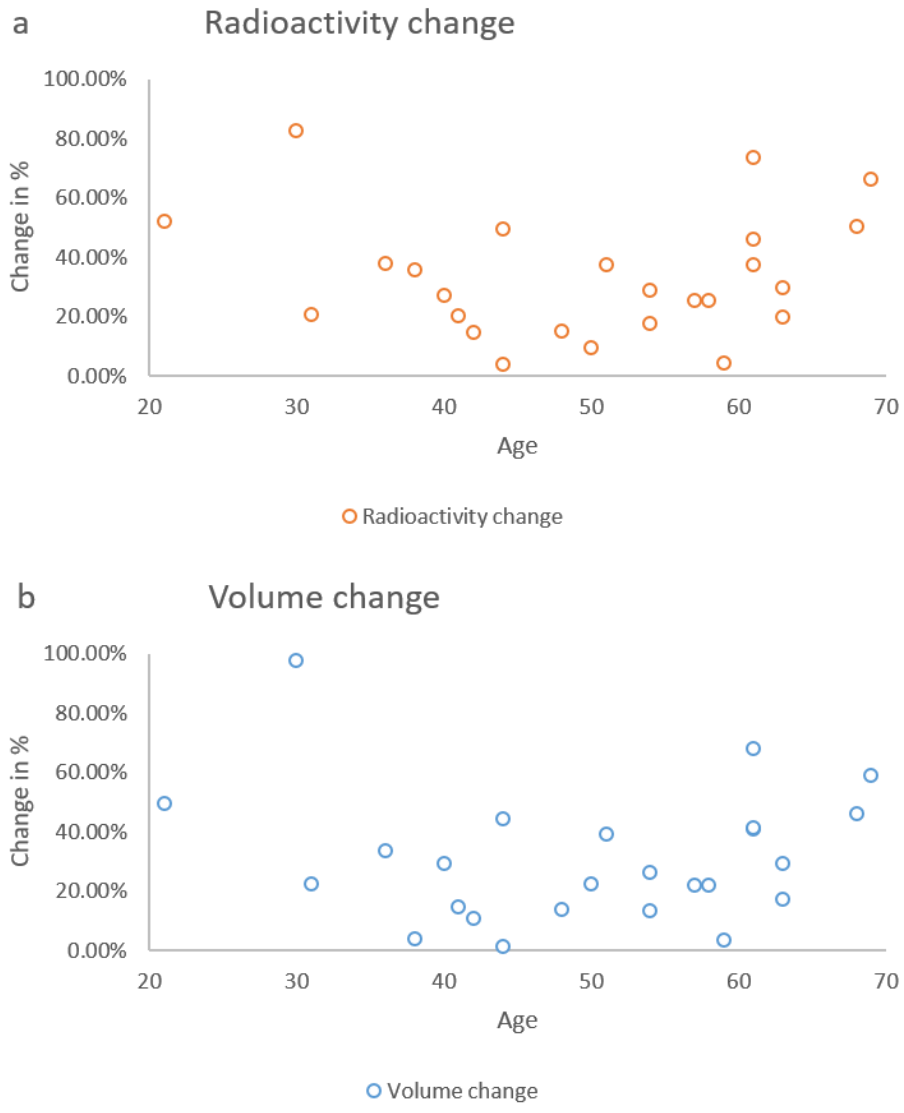

Figure 4.11 – The change in radioactivity (a) and volume (b) from patients at different ages.

Besides, the patients have also been divided into two subgroups by gender. As shown in Figure 4.14, no significant difference could be found between these two subgroups, suggesting that the therapeutic response of patients is not related to the gender in this study.

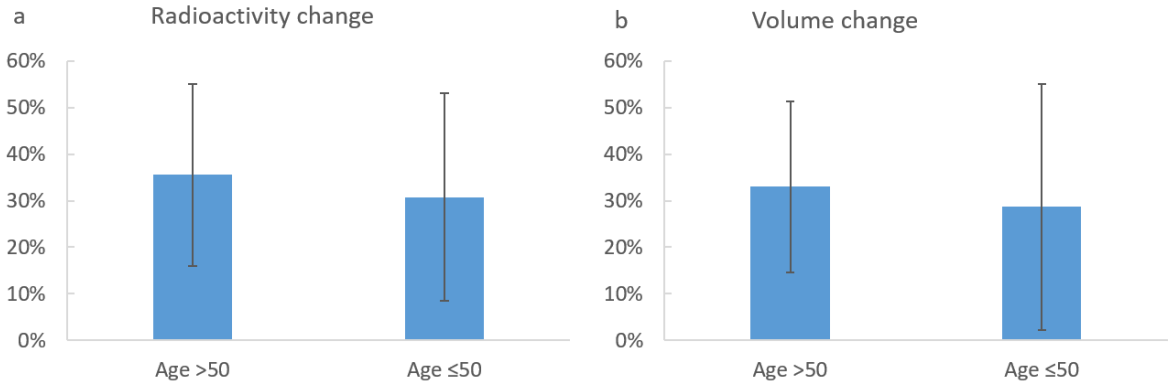

Figure 4.12 – The comparison of therapeutic response in patients aged >50 and ≤50. No significant difference in radioactivity change (a, p = 0. 0.5730), or subsequent volume change (b, p = 0.6430) was found between these two subgroups of patients.

Moreover, as shown in Figure 4.15, the result of comparison of the F-18 ML-10 assessment in female (blue) and male (red) patients does not show any significant difference in the linear correlation between tumor volume change and changes in radioactivity early after radiotherapy, suggesting that the applicability of F-18 ML-10 assessment is not influenced by gender in this study.

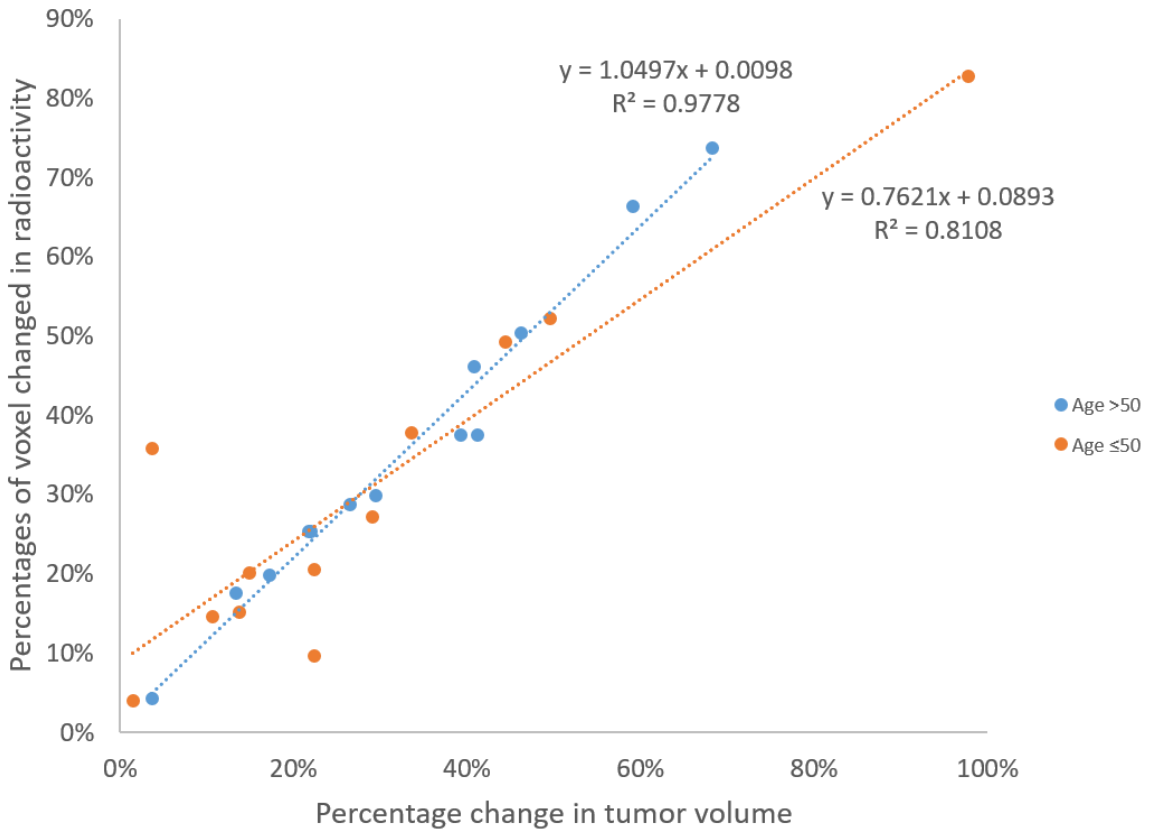

Figure 4.13 – The comparison of the F-18 ML-10 assessment in patients aged >50 (blue) and ≤50 (red). The F-18 ML-10 assessment on patients elder than 50 years old shows a better linear correlation between tumor volume change and changes in radioactivity early after radiotherapy.

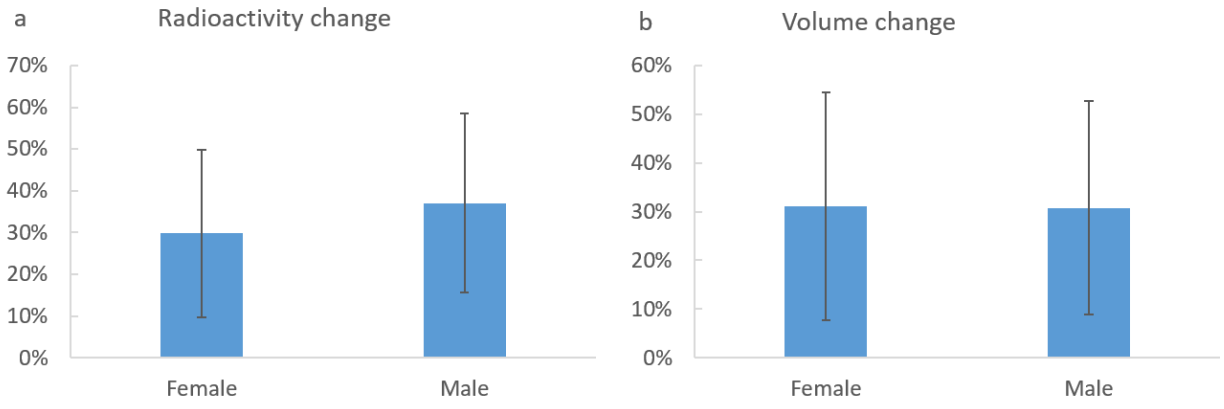

Figure 4.14 – The comparison of therapeutic response in female and male patients. No significant difference in radioactivity change (a, p = 0.3888), or subsequent volume change (b, p = 0.9718) was found between these two subgroups of patients.

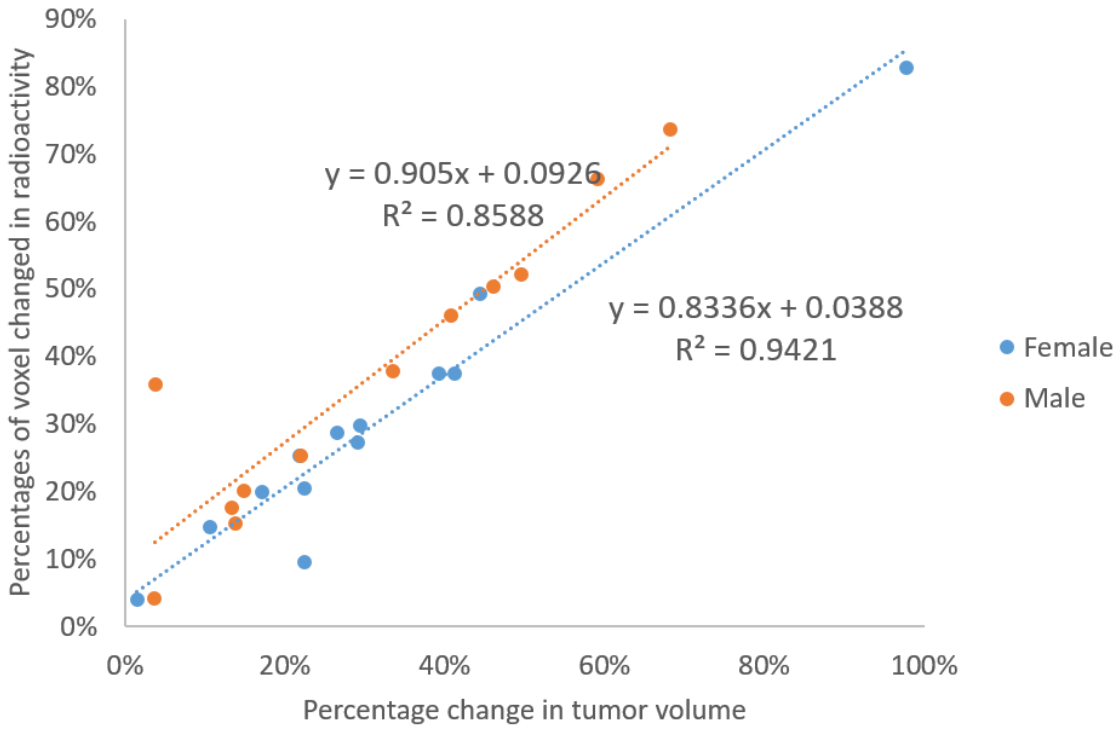

Figure 4.15 – The comparison of the F-18 ML-10 assessment in female (blue) and male (red) patients. The F-18 ML-10 assessment on this two groups of patients does not show significant difference in the linear correlation between tumor volume change and changes in radioactivity early after radiotherapy.

4.2.6 Discussion on the clinical application of F-18 ML-10

Before the clinical use of F-18 ML-10 apoptosis imaging, F-18 FDG PET imaging has been used for the radiotherapy assessment in intracranial tumor in some studies [21, 165]. However, the increased F-18 FDG uptake caused by radiotherapy-related inflammation could lead to a false positive result in PET images. In addition, the high F-18 FDG uptake in normal tissue reduces the signal-to-noise ratio. Therefore, F-18 FDG imaging is not an ideal method for the assessment of intracranial tumor radiotherapy due to the limited accuracy. Lorberboym et al [28] investigated apoptosis imaging of intracranial tumor by Tc-99m Annexin-V SPECT imaging, which could achieve better accuracy. However, it was

limited by the high molecular weight, slow blood clearance, immunogenicity, and poor specificity of Tc-99m Annexin-V [24].

Early quantitative assessment of radiotherapy via non-invasive imaging is important to evaluate the treatment and then improve clinical management. In this study, F-18 ML-10 has been used to visualize the change of apoptosis in tumor area as an early assessment of CK treatment for intracranial tumor. With voxel-wise analysis as well as correlation analysis, the feasibility of the assessment method was demonstrated. The safety and efficacy of F-18 ML-10 has been investigated in preclinical studies [26] and multi-center clinical trials [22], suggesting good stability, safety, specificity, and rapid biodistribution.

The concept of apoptosis was first proposed by Kerr et al [166]. A study on the difference between apoptotic cells and necrotic cells suggested that apoptosis is a programmed death process, the inhibition of which is highly related to the occurrence and development of tumor [167]. In addition, as B-cell lymphoma 2 (Bcl-2) gene is identified as a regulator of apoptosis, it is considered to be anti-apoptotic thus classified as an oncogene. Therefore, it is misunderstood that the apoptosis in tumor tissue is less active than normal tissue. In fact, more apoptosis was found in tumor tissue than normal tissue in most cases. In this study, a significantly higher F-18 ML-10 uptake in tumor cells was observed in PET/CT images.

Cancer is treated with radiotherapy mainly by apoptosis induction [25, 29, 162]. In the early stage of an effective treatment, complex pathophysiological changes occur in the tumor, including apoptosis onset in vascular endothelial cells, vascular occlusion and consequent removal of necrotic cells, etc. Especially, the tumor vascular occlusion and the

removal of necrotic cells result in reduced tracer uptake visualized by apoptosis imaging, thus attenuates the overall apoptosis change in tumor tissue [9]. In this study, heterogeneous and two-way change of F-18 ML-10 uptake was observed in some subjects, as shown in Figure 4.4. Therefore, it may not be accurate to evaluate the efficacy of the treatment using the overall change of tracer uptake in ROI after treatment. Considering the spatial heterogeneity of tumor tissue, a voxel-based analysis method proposed by Moffat et al[164] was used in this study. The PET signal of the whole tumor tissue was divided into voxels – the smallest unit of three-dimensional imaging. The change in radioactivity in each voxel was then calculated and classified into three categories (increase, decrease, and unchanged) with the threshold of 12.5%. For the quantitative analysis of the voxel-wise change, the voxels with both increased and decreased tracer uptake (red and blue points shown in Figure 4.5) were put together as tissue with apoptosis change induced by radiotherapy, to take the heterogeneously internal changes from the tumor tissue into consideration. Positive correlation was observed between the change in F-18 ML-10 uptake (X) and the subsequent change in tumor volume (Y) with a linear regression equation: $Y = 1.018 * X - 0.016$. Additionally, the difference of voxels with increased and decreased tracer uptake may provide potential reference to distinguish the apoptosis and necrosis in tumor tissue.

Twenty-nine subjects with multiple types of intracranial tumor have been investigated in this study, 30 lesions in 29 patients were classified into malignant and benign, according to 2016 WHO CNS tumors classification. A significantly different response in radioactivity, as well as subsequent tumor volume change, has been observed, suggesting that malignant tumors tend to be more sensitive to CK treatment. All 30 lesions have also been divided into two groups by pre-CK radioactivity, but no significant difference was found in

radioactivity change, or subsequent volume change, indicating that the therapeutic response of CK treatment is not correlated with the apoptosis before CK treatment.

Although clinical trials of small molecule probes conducted worldwide is limited, its potential for early assessment of radiotherapy has been proved to be effective and reliable, as shown in this study and previous preclinical and clinical studies [22, 23, 26]. The study is limited to the small samples size, and further studies are needed with large sample clinical data.

4.3 Summary

In this chapter, I demonstrate that F-18 ML-10 PET/CT apoptosis imaging to be a safe and effective clinical method for the assessment of early response of radiotherapy. In F-18 ML-10 PET/CT apoptosis imaging, the tracer uptake in normal brain tissue is lower than that in tumor tissue, thus the anatomic positioning of tumor tissue and surrounding edema area could be accurately identified and visualized. More importantly, F-18 ML-10 PET/CT apoptosis imaging can be used for early prediction of the effectiveness of CK radiotherapy. A significant correlation between the rate of change in F-18 ML-10 uptake in the tumor and the rate of subsequent change in tumor volume was observed. In comparison to the therapeutic response in different cancer types, a rapid response in radioactivity, as well as subsequent tumor volume change, has been observed in malignant tumors, which tends to be more sensitive to CK treatment. Another comparison indicates that the therapeutic response of CK treatment is not significantly correlated with the apoptosis level before CK treatment by the study. By analyses on the application of this method on different patients, the result indicates that the F-18 ML-10 early assessment may give a more accurate

evaluation early after radiotherapy. Our study has also shown the accuracy of AMIC Ray-Scan 64 PET/CT and safety of CK stereotactic radiosurgery treatment of intracranial tumors in PLAGH.

4.4 Experimental

4.4.1 Subjects

From January 2014 to December 2015, 29 human subjects (30 lesions) with intracranial tumors in our institution scheduled to undergo CK stereotactic radiotherapy, were enrolled in the study. These patients were strictly selected according to the integration and elimination standards and their informed consents have been acquired.

The inclusion criteria were as follows: 1, the patient voluntarily subjects to this study, and the patient or legal representative signs the informed consents; 2, the patient is between 18 to 75 years old; 3, the patient has been diagnosed as intracranial tumor and meets the criteria for CK treatment; 4, there are no abnormal findings on patient' routine blood, urine, and biochemical examination, electrocardiogram (ECG) and chest X-ray.

4.4.2 Informed consent and statement of human rights

Informed consent was obtained from all participants. All protocol of this clinical study has been approved by Institutional Review Board of Chinese PLA General Hospital

4.4.3 Imaging protocol

4.4.3.1 PET/CT acquisition protocol

PET/CT imaging were performed before and 48 hours after CK therapy with AMIC Ray-Scan 64 PET/CT system (AMIC, Beijing, China), 90 minutes after F-18 ML-10 tracer injection with 0.12 mCi/kg b. w. The F-18 ML-10 tracer was produced at the Department of Nuclear Medicine at PLAGH PET Facility[163] with PET-MF-2V-IT-I Fluorine multifunctional synthesis module (PETKJ, Beijing, China), and the radiochemical purity is of >98% by HPLC.

PET images were acquired by three-dimensional brain mode, with 2.5-mm slice width, 512 × 512 reconstruction matrix. CT images were acquired with a 50-cm field of view (FOV), 75-cm diameter of gantry, 2.5-mm of slice width, 150-cm maximum positioning length, 175-cm axial moving range of patient bed, and 512 × 512 of reconstruction matrix.

4.4.3.2 MRI acquisition protocol

MRI and CT scanning were used for location of tumor and anatomic assessment of the tumor response 2 to 4 months after radiotherapy. All MRI images were acquired on the 1.5 Tesla (1.5 T) MRI scanner (Siemens Espree, Siemen, Erlangen, Germany). Axial T1-weighted imaging (T1WI) was acquired, with slice width of 0.7 mm, repetition time (TR) = 1650，echo time (TE) = 3 ms; T2- weighted imaging (T2WI) was acquired, with slice width of 1.0 mm, TR = 5500, TE = 93 ms. 0.2 mmol/kg b.w. of Gadolinium-diethylenetriamine pentaacetic acid (Gd-DTPA) was injected intravenously prior to 3D T1WI enhanced imaging with above parameters.

4.4.3.3 CT acquisition protocol

CT images for localization of tumor were acquired on Brilliance TM (Philips healthcare, Amsterdam, Netherland), with an 80-cm maximum field of view (FOV), 60-cm actual FOV, 85-cm diameter of gantry, 1.5-mm of slice thickness, 150-cm maximum positioning length, 190-cm axial range of patient bed, and 1024 × 1024 of maximum reconstruction matrix.

4.4.4 Radiotherapy protocol

CyberKnife which enables stereotactic radiosurgery delivery applied in this study was manufactured by Accuray (Accuray Inc., Sunnyvale, CA, USA). Non-isocentric treatment plan was implemented through accelerator mounted on the robotic arm with continuous real-time image-guided technology.

The blood, urine as well as biochemical examination, ECG and chest X-ray was acquired before. After enrolment, patients underwent head CT and MRI scanning for location of tumor. For each patient, the acquired CT images was co-registered with MRI images by MIM software (version number: 6.5.4), which was imported into CyberKnife Robotic Radiosurgery System (Multiplan 4.0.2) for target and organs at risk delineation. With the information provided by the fused images, the target area of CK treatment was optimized and the gross tumor volume (GTV) was recorded by radiologists and physicians. Patients underwent CK stereotactic radiosurgery with 6D‑skull tracking, and the treatment scheme was with 14-24 Gy in 1-3 fractions depending on the tumor size and position.

4.4.5 Imaging analysis

Voxel-based analysis on PET/CT image was used in the apoptosis imaging visual analysis, which performs voxel-by-voxel subtraction of the change PET/CT before (pre-CK) and early after CK treatment (post-CK). The PET/CT data of pre-CK and post-CK, along with CT, MRI and GTV data, were delivered to the MIM image processing software after acquisition. The CT data with GTV information were registered with data from PET/CT imaging. With the imported GTV information as reference, region of interest (ROI) was plotted in MIM software. Each voxel value in PET / CT images was represented by radioactivity (Bq/ml) or standardized uptake value (SUV). The images of MRI, CT and PET/CT were registered and the voxel size and slice width from different imaging modalities were normalized. The values of radioactivity for each voxel in the ROI were collected separately on baseline PET scan and the follow-up. The percentage change in each voxel was calculated. Voxel-based subtraction PET images were acquired using MIM software for visual analysis to observe the changes of cell apoptosis before and after CK treatment.

4.4.6 Statistical analysis

For statistical analysis, two-tail paired Student's t-tests were applied with SPSS 19.0 to analyze the change in radioactivity before and after treatment. Correlation between change ratio of radioactivity and lesion volume was analyzed with linear regression analysis. And $p < 0.05$ was considered as statistically significant.

CHAPTER 5. OTHER RELATED WORKS

In previous chapters, I demonstrated how molecular imaging meets the clinical needs for early assessment by F-18 ML-10 apoptosis imaging. Furthermore, molecular imaging could also play important role in early diagnosis and intraoperative tumor detection by distinguishing cancer tissue from normal or other tissues. In this chapter, I demonstrate the analysis of the sensitivity of three molecular probes for hand-held spectroscopic device. The fluorescence and Raman spectroscopy has been normalized and then analyzed. The surface enhanced Raman scattering (SERS) gold nanoparticles have been proved to be ultra-high sensitive for in vitro detection, with wide dynamic range, thus could achieve distinguishing of signal of tumor tissue from that of normal tissue. Furthermore, the differentiation of tumor tissue from inflammatory tissue has also been investigated by a preclinical quad-modality imaging with applying multiple probes.

5.1 Sensitivity of hand-held spectroscopic imaging for surgery guidance

5.1.1 Introduction

As discussed in previous chapters, the use of novel F-18 pharmaceuticals for assessment of cancer therapy has been investigated by distinguishing of the apoptotic cells from viable cells. Such early assessment provides opportunity to early management of cancer therapeutics. Furthermore, it is also important to distinguish the subtle metastases while surgery operation. In this chapter, I further demonstrate the sensitivity of novel molecular probe in real-time guidance for cancer surgery.

Dr. Shuming Nie and colleagues from our group in Emory University first developed spectroscopic device configured with handheld laser probes, and showed that the device has a high detection sensitivity for ICG, can effectively distinguish and label the tumor tissue/lymph and the normal tissue [82]. With this spectroscopic device, the SERS signal could be detected as well. Molecular probes based on nanoparticles that produce signal from SERS have been investigated widely [168-178]. Research and clinical trials for the device has been conducted in the Emory University Hospital and the Affiliated Hospital of Pennsylvania, for imaging-guided breast, lung, colon and pancreatic cancer surgery. About 200 cases of surgical results have supported the effectiveness of the device [81, 83, 179]. The advantages of this device are shown as following:

(1) Ultra high detection sensitivity that can achieve single cell detection level at laboratory and is able to observe subtle metastases while surgery operation, superior to similar devices either domestic or abroad.

(2) No requirement for the in-situ injection of ICG, thus largely reduces the background noise, and helps to exactly locate the tumor before surgery and judge whether there is residual cut edge after the surgery.

(3) Direct detection and real-time observation of tumors while surgery operation.

(4) Applicable for multiple types of cancer.

(5) High speed imaging and data processing system, enabling the real-time observation during surgery operation.

5.1.2 Results and discussion

5.1.2.1 Detection system and photo-stability analysis of three molecular probes

As introduced previously, the SpectroPen could allow sensitive detection by collecting characteristic emission from reagents those who are excited by a laser. The laser utilized by the SpectroPen spreads in a form of the Gaussian beam, so the excitation intensity would be different with the change of distance between the Pen and the sample solutions. The maximal intensity of the laser could be reached when the sample would be located at around the focus of the laser (i.e., the waist of the laser beam). According to the calculation:

$$f = \frac{\pi w_0^2}{\lambda} = \frac{3.14\times(50\mu m^2)}{0.785\mu m} = 10^4\mu m = 1cm\ ,$$

The radius of the laser spot is theoretically 1 cm, so that the highest energy of the laser beam should be around the area of 1 cm away from the sampling head. With the higher excitation, more electrons in reagent solutions would be excited, resulting in a higher intensity of the emission signal received via the SpectroPen.

As shown in Figure 5.1, distance dependence was investigated by an experiment of varying the distance between the Pen and the samples. The reagent for this distance dependence experiment is SERS-tag nanoparticles with the concentration of 50 pM. All the signals collected by detector under certain distance have been integrated to indicate the total intensity of the emission, which is proportional to the excitation energy. As depicted in Figure 5.2a, the detector could receive the highest signal intensity when the sampling head is located at 8 mm away from the top of the sample solution.

5.1.2.2 Limits of measurement comparison among QD, IR dye and SERS gold nanoparticle

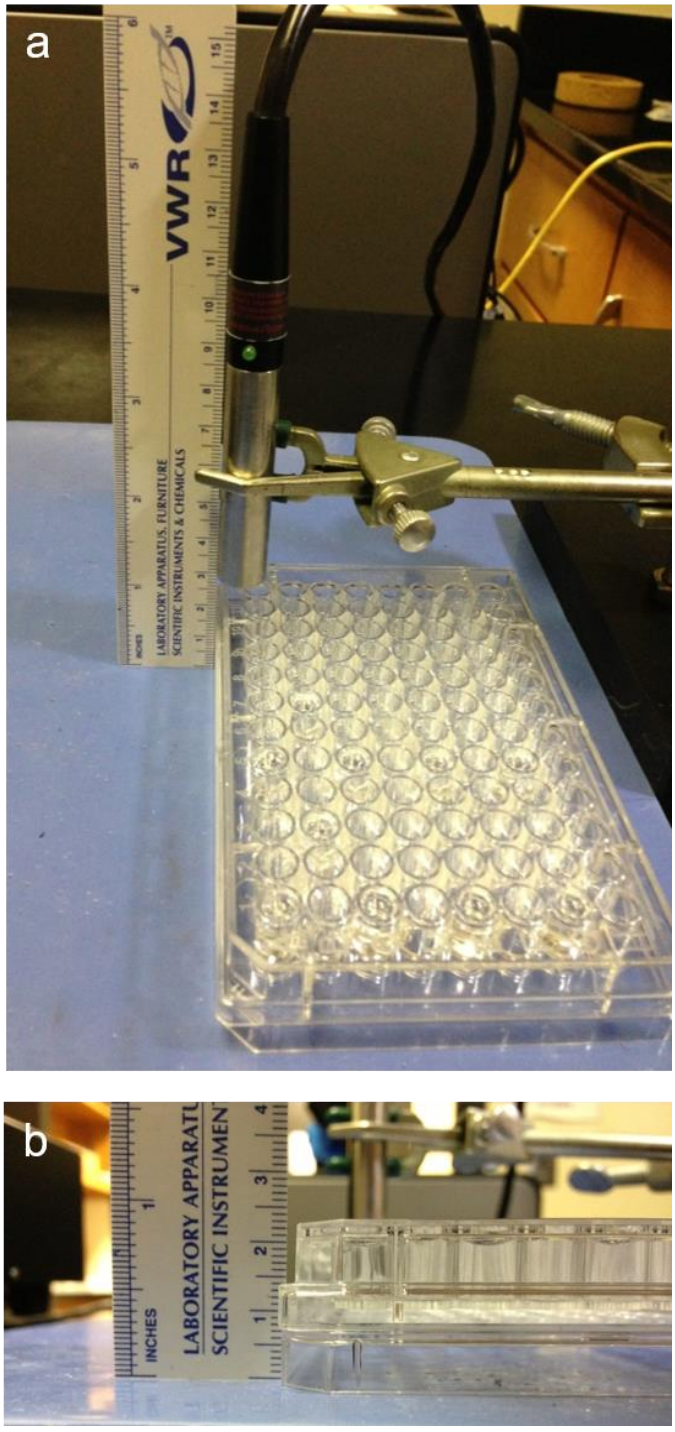

Figure 5.1 – Setup for detection system (a) and for the distance dependence (b).

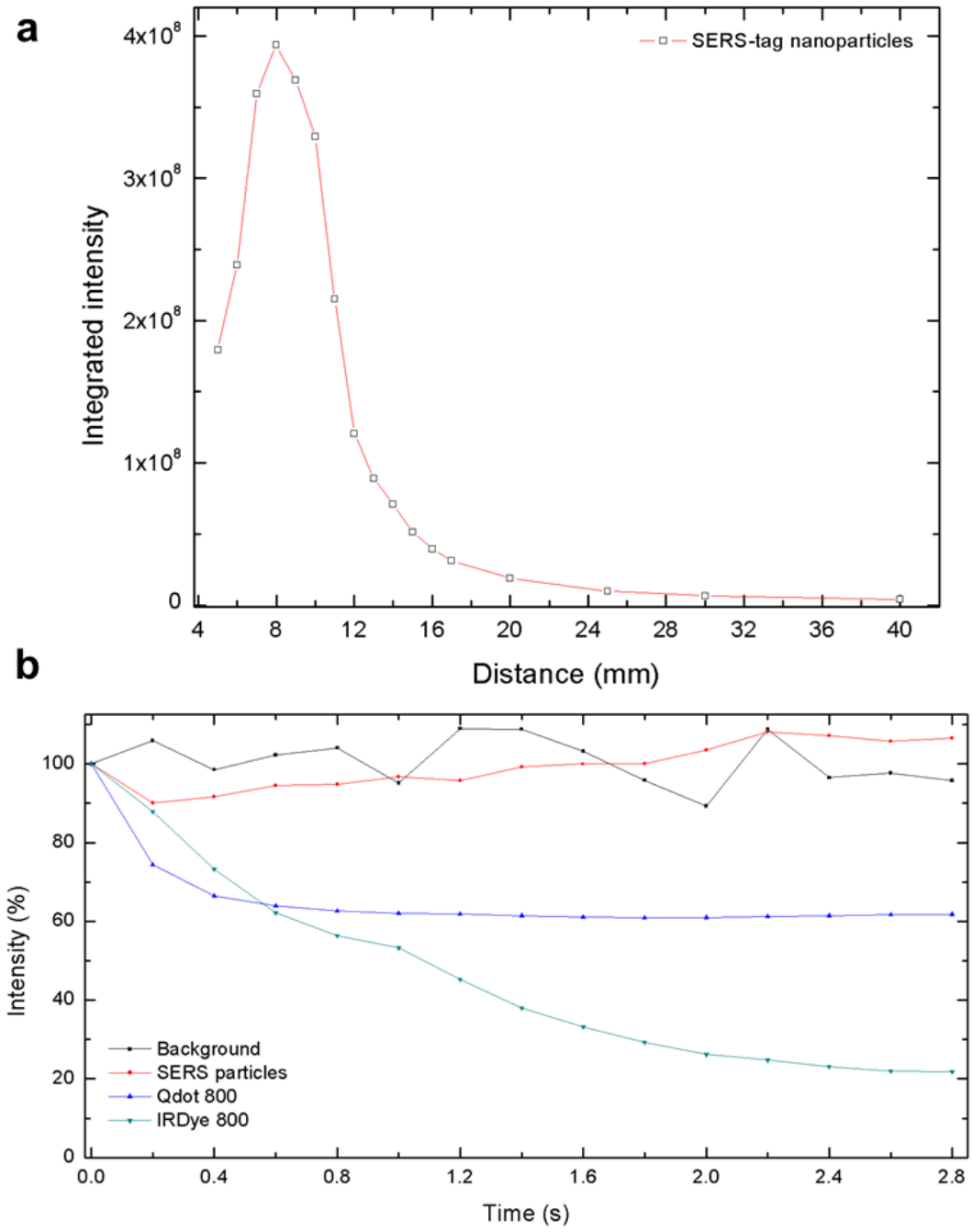

Figure 5.2 – (a) The signal from SERS-tag nanoparticles at concentration of 50 pM collected by detector at detection distances ranging from 4 mm to 40 mm. (b) Photostability test of 5 nM of Qdot 800 (blue line), 5 nM of IRDye (cyan line), 0.75 pM of SERS-tag nanoparticles (red line), and background (black line).

To investigate whether the SERS-tag nanoparticles remain photosensitive when shined under the focused laser beam, we studied the photobleaching of SERS-tag

nanoparticles and compared with IRDye 800 and Qdot 800. As shown in Figure 5.2b, the results suggest that there was no noticeable photobleaching for the nanoparticles over the average detection period for SpectroPen, while decreases in fluorescence intensity were observed for other two reagents with the same setup. The signal of Qdot 800 decreases 30% of the original fluorescence intensity within the first 0.3 second excitation, but the emission intensity remains 61.8% after 2.8 second shining under laser. The reagent IRDye 800, however, suffers from the severe photobleaching – there is only 21.8% remaining intensity after the reagent exploded under laser for 2.8 second.

As shown in Figure 5.3a, the original spectra of three reagents were detected by SpectroPen with considerable signal-to-noise ratio. In the SERS spectrum, the wavenumber was converted to wavelength prior to comparing the limit of measurement.

In this study, the limit of measurement has also been determined as the minimal spectrally resolvable concentration. As depicted in Figure 5.3b, taking the quantum dots (QD) 800 as an example, as the spectrum of 0.025 nM QD 800 is the minimal spectrally resolvable concentration, this would be considered as the limit of measurement of QD 800 by this SpectroPen. To better analyze the linearity and dynamic range of fluorescent signal, all the data point in the same range of wavelength (i.e., 797.52 – 931.20 nm, or 200 – 2000 cm^{-1}) has been integrated.

As the analysis of SERS spectrum usually based on the “fingerprint” in the spectrum, rather than the overall integration, the method of integration for SERS signal has been compared as shown in Figure 5.4. As shown in Figure 5.4a, we integrated all the data from 200 – 2000 cm^{-1} without any further data processing. The R square value is 0.99847.

However, for SERS signal, there is a high background caused by the SERS signal itself. Therefore, partially integration of the data after subtracting the baseline has been analyzed, where the baseline was defined as the lowest value of the data in the range from 400 to 1700 reciprocal centimeter. The R square value is slightly higher, which is 0.99862.

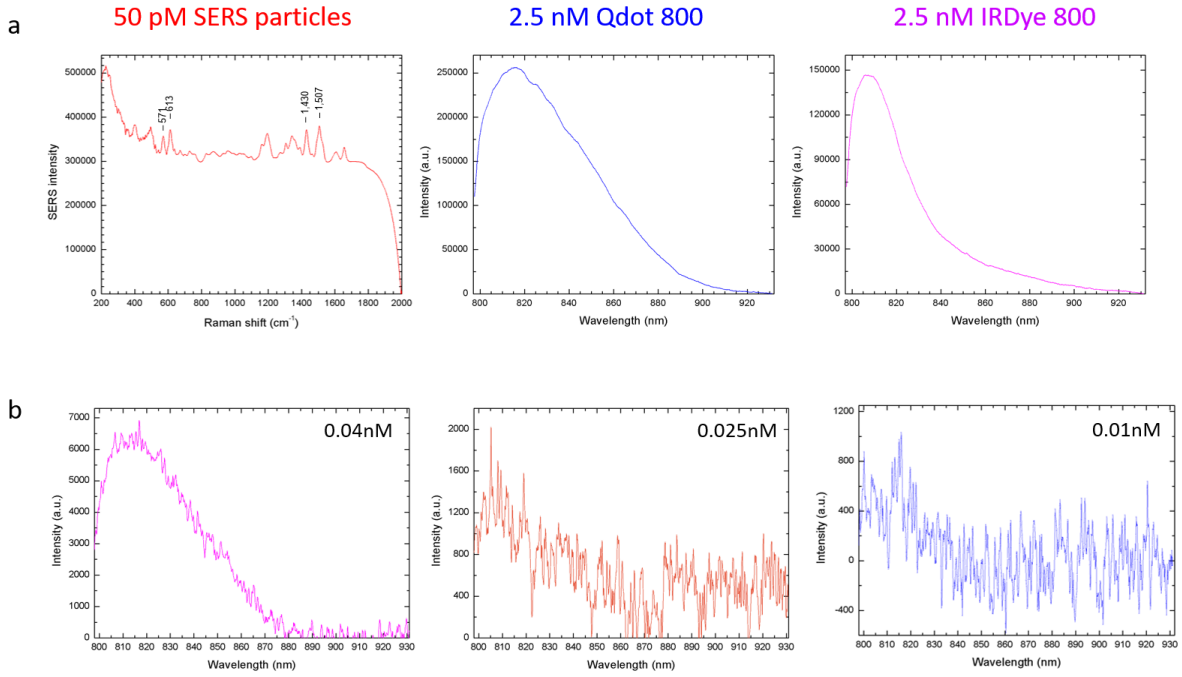

Figure 5.3 – (a) Original spectra of QD, IRDye, and SERS gold nanoparticles detected by SpectroPen; (b) determination of limit of measurement with different concentration of QD solution.

As the peak at 1507 cm^{-1} is one of the characteristic peaks of this SERS agents, the peak height has also been used for the analysis. The linearity of the last method is the best of all three methods, where the R square value is 0.99915. The last analytical method provides the most accurate relationship between signal weakness and concentration of SERS agents. Therefore, we use this peak height method to analyze the SERS signal. However, for the comparison of three reagents, the integrated method is adopted to keep the comparison consistent.

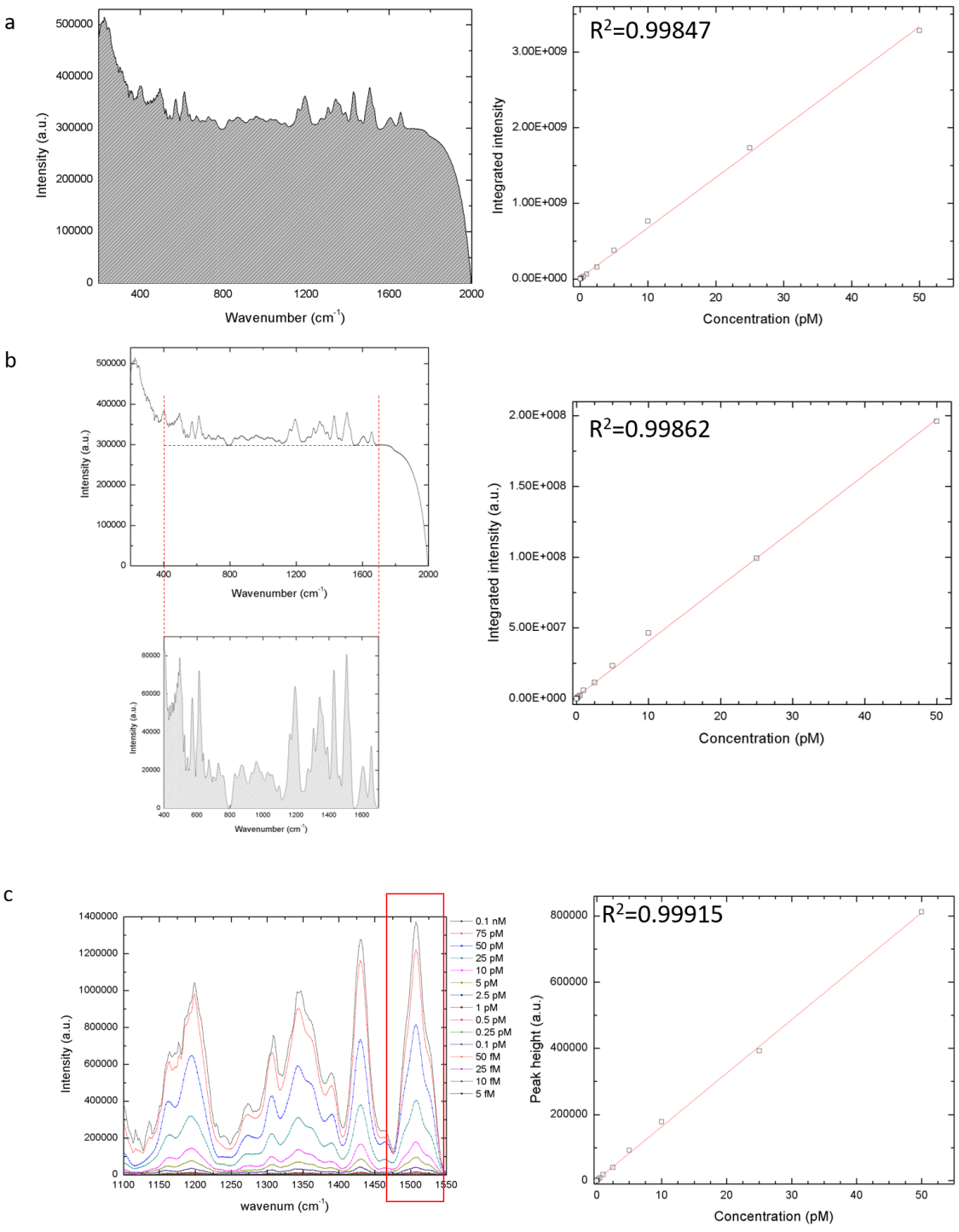

Figure 5.4 – Integration of SERS signal: (a) integration of data from 200 – 2000 cm^{-1}; (b) partial integration of data after subtracting the baseline from solvent; (c) the intensity of one characteristic peak at 1507 cm^{-1} after subtraction of baseline.

In this study, the reagents were firstly diluted in water. However, the signal, especially for low concentration, are various under the same condition, due to adhesion of the particles to the surface of tubes. As the bovine serum albumin (BSA) is usually be supplied to prevent this adhesion. Therefore, we applied 1% BSA in the solvent to prevent reagents absorbing to the wall of wells. Diluted in BSA solution, the reagent provides a more stable signal at low concentration, and the comparison of BSA solution and aqueous solution is shown in Figure 5.5.

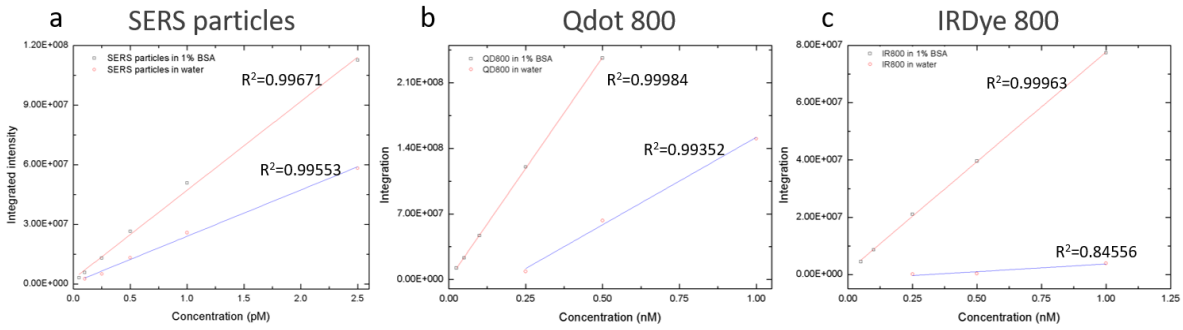

Figure 5.5 – Comparison of solvent: 1% BSA solution (red) and aqueous solution (blue).

To measure the limits of detection of IRDye 800, the solution was diluted to concentrations ranging from 0.01 to 0.5 nM. The spectra are shown in Figure 5.6a, the minimal spectrally resolvable concentration of SERS agent is 5×10^{-11} M (i.e., 0.05 nM), with the detection distance of one centimeter.

The Quantum dots were also diluted to concentrations ranging from 0.01 to 0.5 nM. The minimal spectrally resolvable concentration of Quantum dots is 2.5×10^{-11} M (i.e., 25 pM), under one-centimeter detection. To measure the limits of detection of SERS nanoparticles, the solution was diluted to concentrations ranging from 0.1 pM to 5 fM. According to the peak height analytical method, the spectra after subtracting background

is shown in the Figure 5.6c. As depicted in this figure, the minimal spectrally resolvable concentration of SERS agent is 5×10^{-11} M (i.e., 5 fM), under one-centimeter detection.

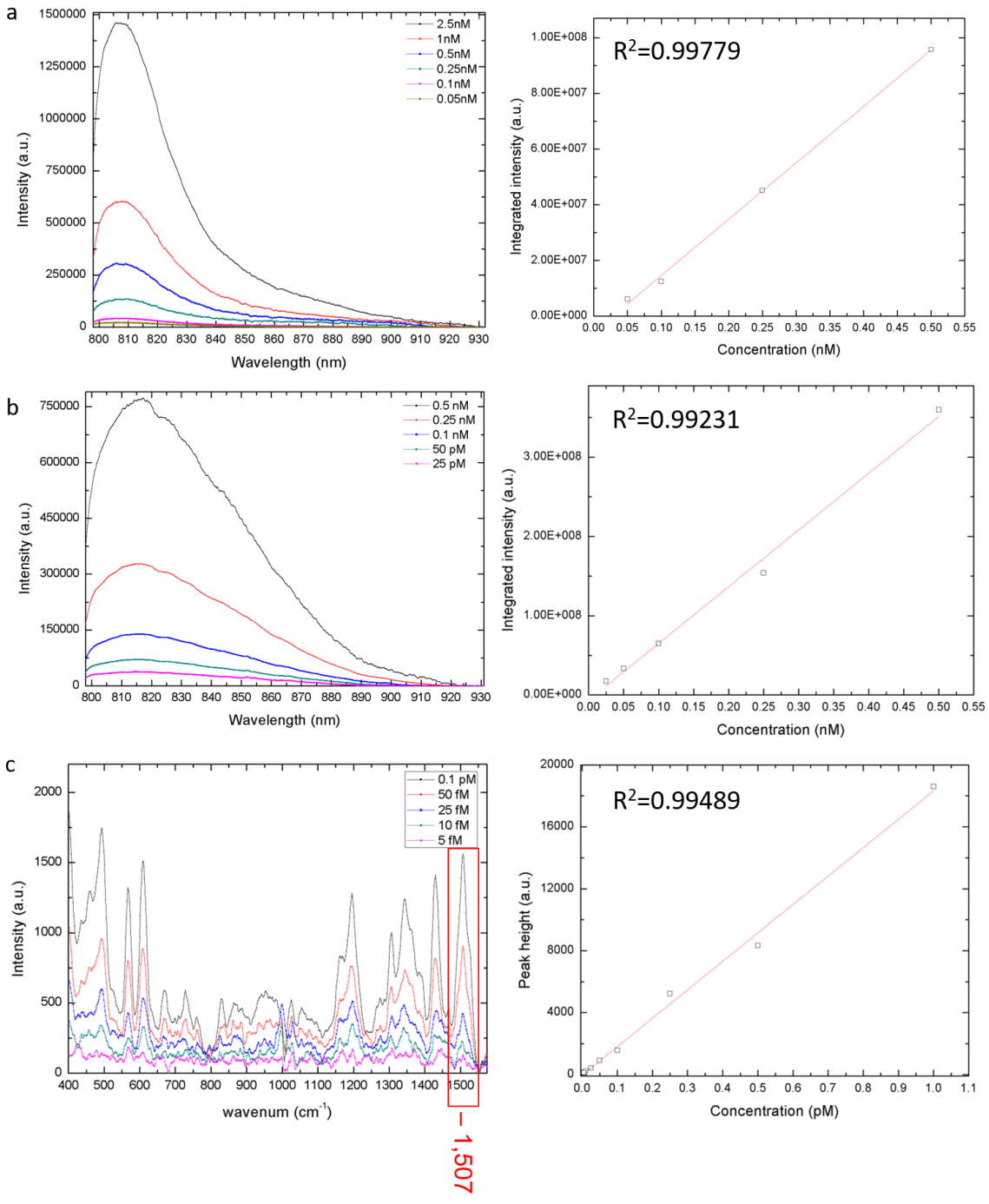

Figure 5.6 – Limit of measurement of IRDye 800 (a), Qdot 800 (b), and SERS gold nanoparticles (c).

By further investigation on the limit of measurement of SERS gold nanoparticles, the detection under 8 mm for as long as 30 second integration has been set. As shown in Figure 5.7, the result suggests that the spectrum of 1 fM SERS agents cannot be detected. But the signal-to-noise ratio at concentrations of 10 fM, 5 fM, and 2.5 fM is acceptable. So that the SERS particles have an ultra-sensitivity, that is, 2.5×10^{-15} M, for SpectroPen detection.

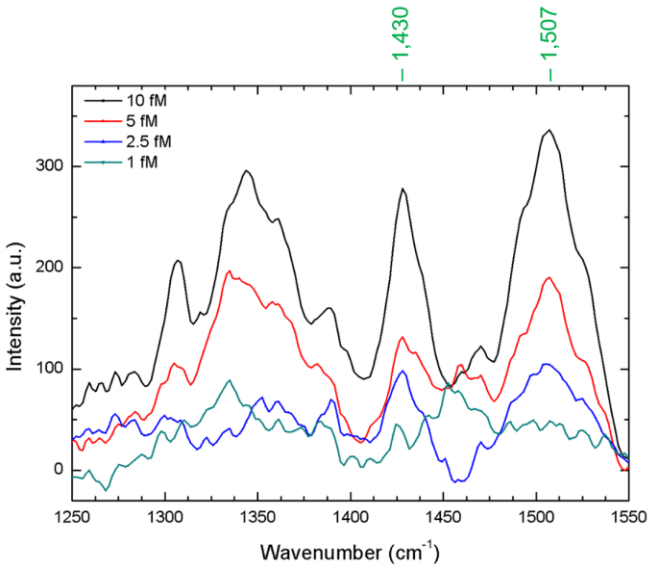

Figure 5.7 – Limit of measurement of SERS gold nanoparticles with 30 second acquisition under focus distance.

As the laser of SpectroPen spreads like a Gaussian beam, the depth of focus is defined by the radius of the laser spot, which could be calculated to 1 cm. The beam could be treated as a cylinder shown in Figure 5.8a. The exact volume of solution under laser shining could be calculated, resulting in 0.0628 microliter in 300 microliter samples, according to the calculation:

$$V_{cylinder} = \pi w_0^2 \quad L$$
$$= 3.14\times(50\mu m)^2\times 8mm = 0.0628mm^3$$

Therefore, the particles number could be calculated to 95, according to the calculation:

$$Number = n\ N_A = c\ V\ N_A$$
$$= 2.5\times10^{-15} mol/L \times 6.28\times10^{-8} L \times 6.022\times10^{23} mol^{-1} = 95$$

It is suggested that the minimum of the gold nanoparticles number for SpectroPen detection is around 95 particles.

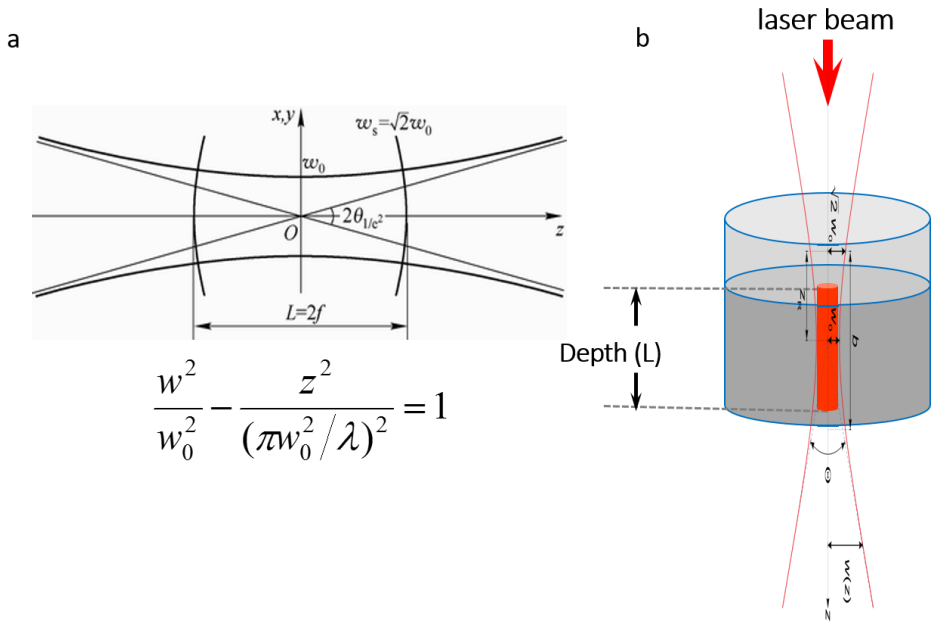

$$\frac{w^2}{w_0^2} - \frac{z^2}{(\pi w_0^2/\lambda)^2} = 1$$

Figure 5.8 – Schematic of Gaussian beam (a) and the laser beam travel through the detection system (b).

5.1.2.3 Dynamic range of detection of three molecular probes by SpectroPen

To investigate the dynamic range of the detection, the molecular probes have been diluted into a wide range of concentration. As those fluorescent agents cannot tolerate a long integration time, owing to the photo bleaching, the one second acquisition was taken for the normalization. As SERS particles are photo-stable, they can be used to acquire signal with longer time. Therefore, the acquisition time for IR800 and QD800 were limited to no longer than one second, while for SERS particles, the acquisition time could be longer than 10 second.

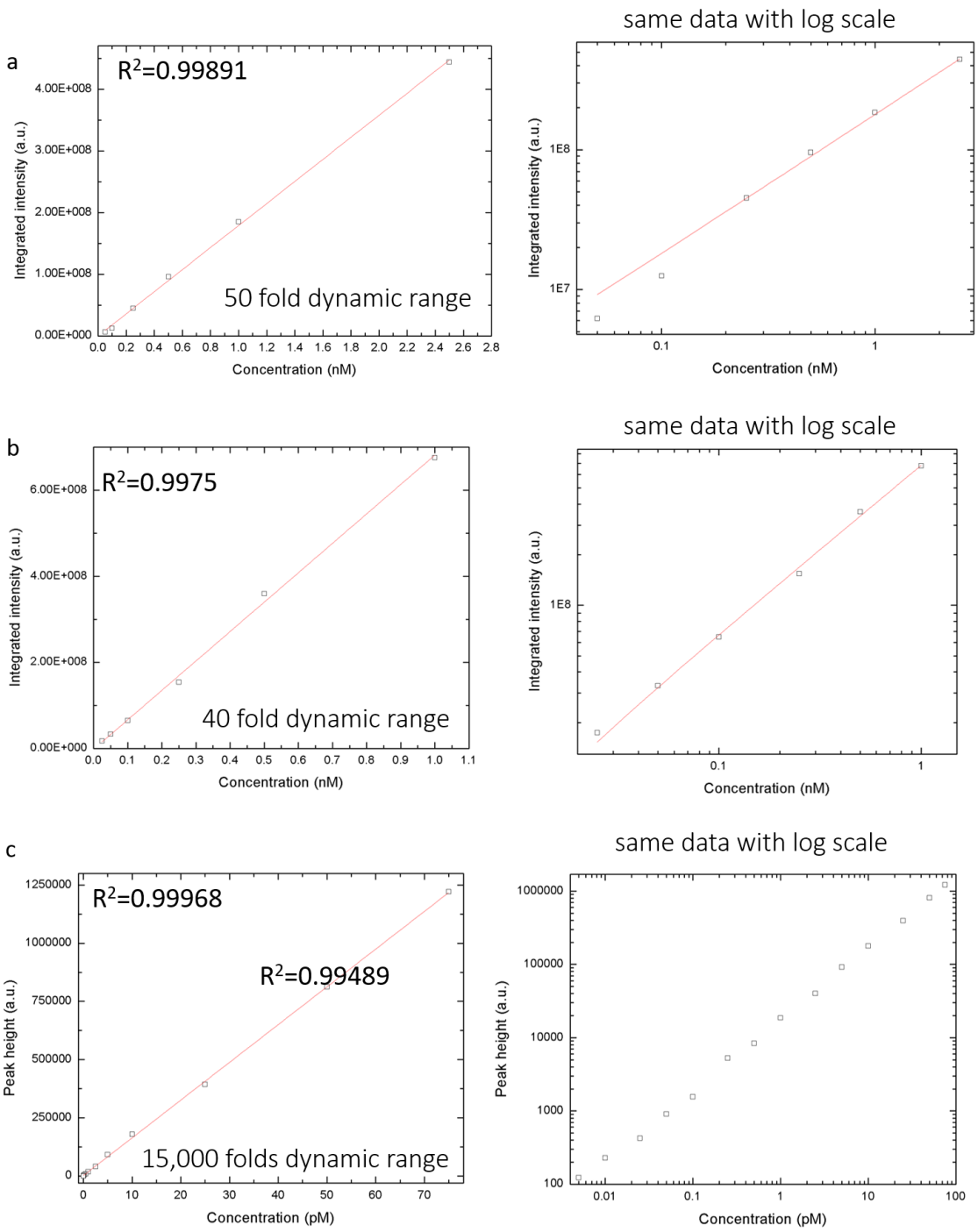

Figure 5.9 – Dynamic range of IRDye 800 (a), Qdot 800 (b), and SERS gold nanoparticles (c).

As shown in Figure 5.9, the dynamic range of IRDye 800 (a), Qdot 800 (b), and SERS gold nanoparticles (c) are 1, 1, and 4 orders of magnitude, respectively. With a much wider

dynamic range, SERS particles could have great potential to accurately discover tumor-margin, where the signal would be much lower than central tumor tissue. Although the SERS signal saturates the detector of SpectroPen at the concentration of 75 pM, the signal intensity could reach a high level with the increase of the concentration to nM level.

Therefore, for the same concentration of reagents, SERS particles would have an overwhelming high intensity of signal, resulting in a potentially more accurate but less expensive diagnostic approach. On the other hand, focused on the application of SpectroPen, SERS particles could provide a considerable high signal at a low concentration, which would help with reducing the toxicity and side effect of the agent itself. Thanks to its ultimate photo stability, SERS particles may have potential to achieve a higher sensitivity with intense stimulation.

5.1.3 Summary

In this chapter, I demonstrate the sensitivity investigation of widely used optical probes for SpectroPen real-time guidance for tumor removal surgery. The limit of measurement of SERS particles is 10 thousand times lower than QD800, even 20 thousand times lower than IR800. Furthermore, the dynamic range of SERS nanoparticles is more than 300-fold higher than other 2 imaging probes.

These parameters are important for the application of SpectroPen. The Limits of Detection, on one hand, determines the minimal quantity of the injection of contrast agents, which could help with reducing side effect and toxicity. On the other hand, weak tumor-margin signals that are 50-60-fold lower than the central tumor signals. The wider dynamic

range provides opportunity for simultaneous measurement without adjusting the data acquisition parameters.

5.1.4 Experimental

5.1.4.1 Detection sensitivity and dynamic range measurement:

The reagents were diluted in 1% BSA in Phosphate buffered saline (PBS) solution, as well as in water, to a concentration of $5.0 \times 10^{-15} – 1.0 \times 10^{-8}$ M for SpectroPen detection. 300 μL of these reagent solutions and pure solvents for control were transferred into different wells in a 96 well cell culture plates (polystyrene). As previously described, the SpectroPen [82] combines a pen-shaped sampling head and a Raman spectrometer via a FC connector, with a Raman shift range of 200 – 2000 cm^{-1}. Emitting at 785 nm, the excitation is provided by 200 mW near infrared diode laser. The setup of SpectroPen is shown in Figure 5.10a and Figure 5.10b. The sampling head was fixed above the center of each well of the plate. The distance between detector and the sample was measured by a ruler. The integration time of collection was selected properly from 0.1 to 10 s.

5.1.4.2 Tissue penetration measurement

To determine the penetration depth of the SpectroPen detection, chicken breast tissues were utilized to mimicry the human tissue. As shown in Figure 5.10c and Figure 5.10d, droplets of SERS-tag nanoparticles with different concentration and different volume were held by (under) a Parafilm. On the top of the film, different thickness of the meat was put between SERS-tag nanoparticles sample and the SpectroPen. The fluorescence or Raman

spectra were collected from 0.05 to 30 s, depending on the signal-to-noise ratio of the spectra. These tissues were cut to the thickness ranging from 1 to 10 mm, step by 1 mm.

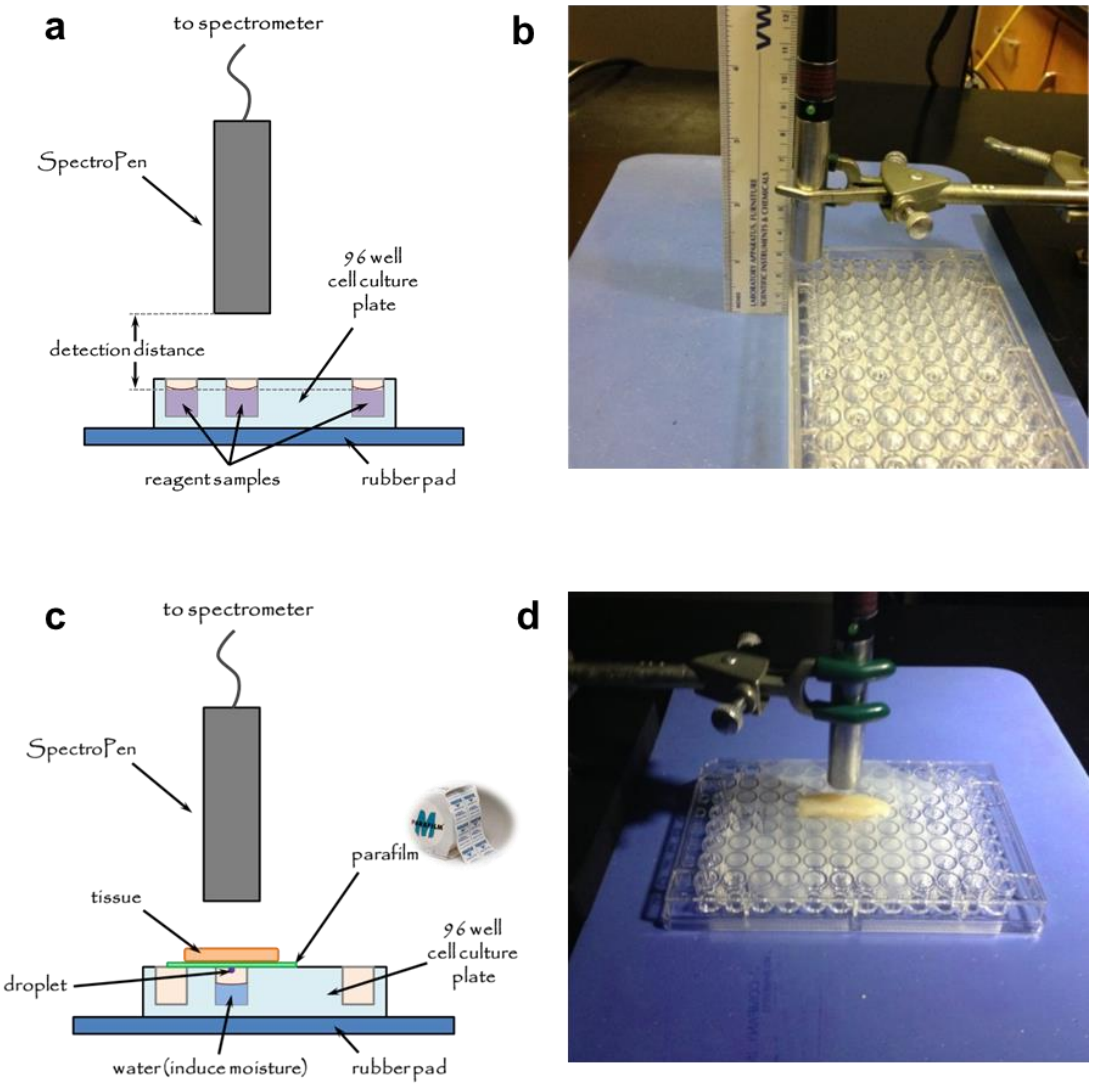

Figure 5.10 – Experimental setup. (a) Sketch and (b) photograph for SpectroPen detection of IR dye, Quantum Dots, and SERS-tag nanoparticles in a 96-well plate. (c) Sketch and (d) photograph for tissue penetration depth studies.

5.2 Preclinical Application on a small animal quad-modality imaging system to distinguish tumor tissue and inflammatory tissue

5.2.1 Introduction

Molecular imaging plays a key role in biomedical research. Recent developments in both imaging techniques and novel molecular probes have sparked great desires for the development of multi-modality and multi-probes molecular imaging instruments.

Up to now, three major molecular imaging modalities have been mostly used, which are PET, SPECT, and fluorescence imaging. Positron emission tomography (PET) and single photon emission computed tomography (SPECT) rely on radiolabeling, which are already clinically used as powerful imaging techniques. Fluorescence imaging relies on optical labeling, such as Green fluorescence protein (GFP), which is favored by researchers due to its versatility and ease of make and use. Several articles have discussed the feasibility and potential opportunities of combining the PET-SPECT and radiology-optical imaging modalities, and recommended to use these kinds of strategies in biomedical research. As a quad-modality molecular imaging system has been developed by our group, the biomedical application could be investigated by using this device

5.2.2 Results and discussion

5.2.2.1 Phantom imaging study

We first investigated the imaging and co-registered performance by using a custom-made multi-modality imaging phantom. The phantom is a solid cylinder having a light scattering property similar to tissue (Figure 5.11p). There are two holes in this cylinder where glass tubes with radiolabeling medicines and fluorescence dyes can be inserted, as shown in Figure 5.11q. With a designed imaging protocol, multimodal molecular imaging of this phantom was performed in a sequential mode. Figure 5.11 shows the imaging results, including images not only by different modalities but also from the co-registered fusion.

Both PET and SPECT provided high quality images without crosstalk. We intended to make a small bubble separating two PET medicine drops, and this small gap was clearly distinguished in PET images with high spatial resolution. In addition, FMI also successfully reconstructed the fluorophores deep in the phantom. In Figure 5.11r, the maximum intensity projection (MIP) rending of the fusion images demonstrated the co-registration performance.

5.2.2.2 Small animal imaging study

We induced a xenograft tumor and an inflammation in the right shoulder and the right hind limb of a BALB/C nude mouse, respectively. We used F-18 FDG for PET imaging, Tc-99m 3PRG2 for SPECT imaging and Cy7-entrapped CCPM nanoparticles for fluorescence imaging. F-18 FDG, which is taken by high-glucose-using cells, has been widely used for PET imaging of tissue metabolism; Tc-99m 3PRGD2, which is a Tc-99m labeled dimeric cyclic RGD peptide with increased receptor binding affinity and improved kinetics for SPECT imaging, is able to target integrin αvβ3-positive tumors; and Cy7-entrapped CCPM nanoparticles, which is a near-infrared (NIR) fluorescence (NIRF) imaging tracer for optical imaging, can preferentially accumulate in tumor site because of the enhanced permeability and retention (EPR) effect, which is characterized by microvascular hyperpermeability to circulating colloidal particles and impaired lymphatic drainage in tumor tissues.

Figure 5.12 shows multi-modality and multi-probe imaging results. Complementing the CT scanning results, the PET images showed high radioactivity accumulation in the brain, the right shoulder and the right legs (Figure 5.12e). In SPECT images, the

radioactivity accumulation of Tc-99m 3PRGD$_2$ primarily occurred in the right shoulder, the abdomen, and the area of bladder (Figure 5.12h and Figure 5.12i). Besides, according to the FMI imaging results in Figure 5.12m, only the area of right shoulder had a significant accumulation of Cy7-entrapped CCPM nanoparticles.

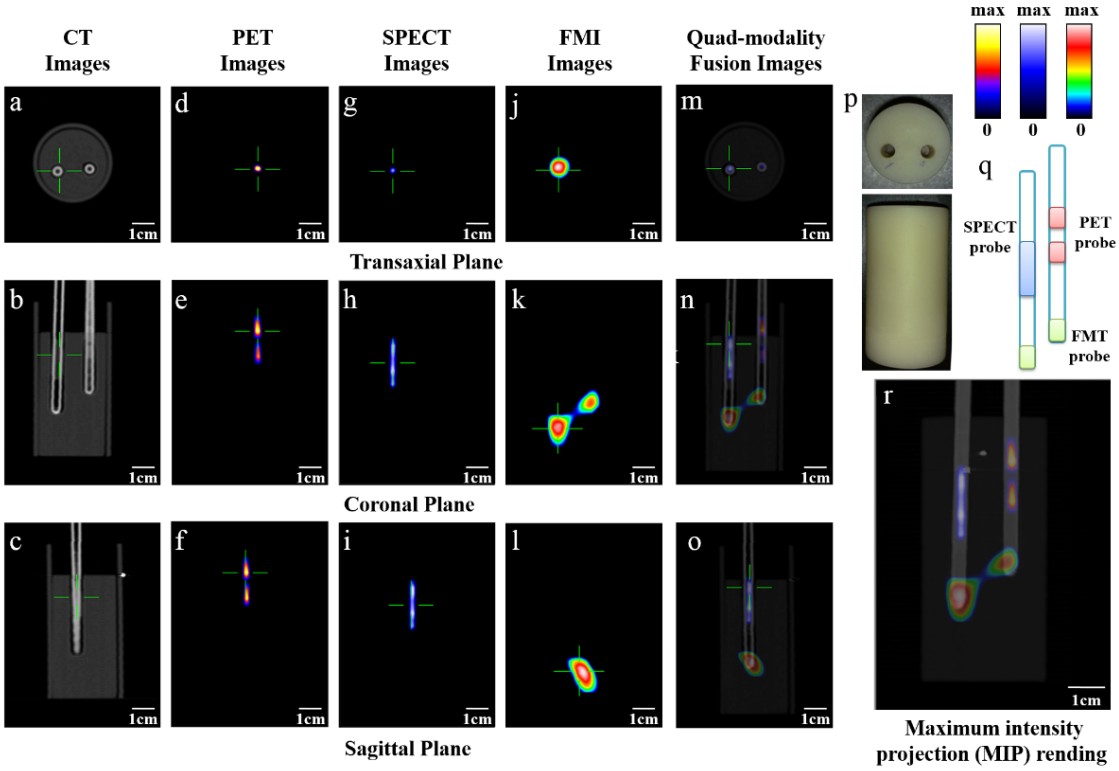

Figure 5.11 – The imaging results of the multi-modality phantom. The CT images (a-b), PET images (d-f), SPECT images (g-i), FMI images (j-l) and quad-modality fusion images (m-o) are presented. In the results, the quality of SPECT images has not been affected by the crosstalk from the positron-emitting radionuclides. The MIP rending of the fusion images (r) demonstrated the co-registration performance. The imaging results indicate that our hybrid multi-modality imaging system resulted in appropriate imaging and accurately co-registered performances. The right, middle and left color bar correspond to the PET images, the SPECT and FMI images respectively. Reprinted from Lu et al [78] with permission. Copyright © 2014 Society of Nuclear Medicine and Molecular Imaging, Inc.

From either the PET image or SPECT image alone, the tumor area remained unclear. However, we were able to identify the tumor's location by the complementary information

obtained from the PET-SPECT-CT fusion images (Figure 5.12k). On the other hand, FMI image gave the right suspicious area, but the imaging resolution is low. Complementing FMI with radioactive molecular imaging significantly improved both specificity and resolution. This result successfully demonstrated the superior power of multimodal molecular imaging.

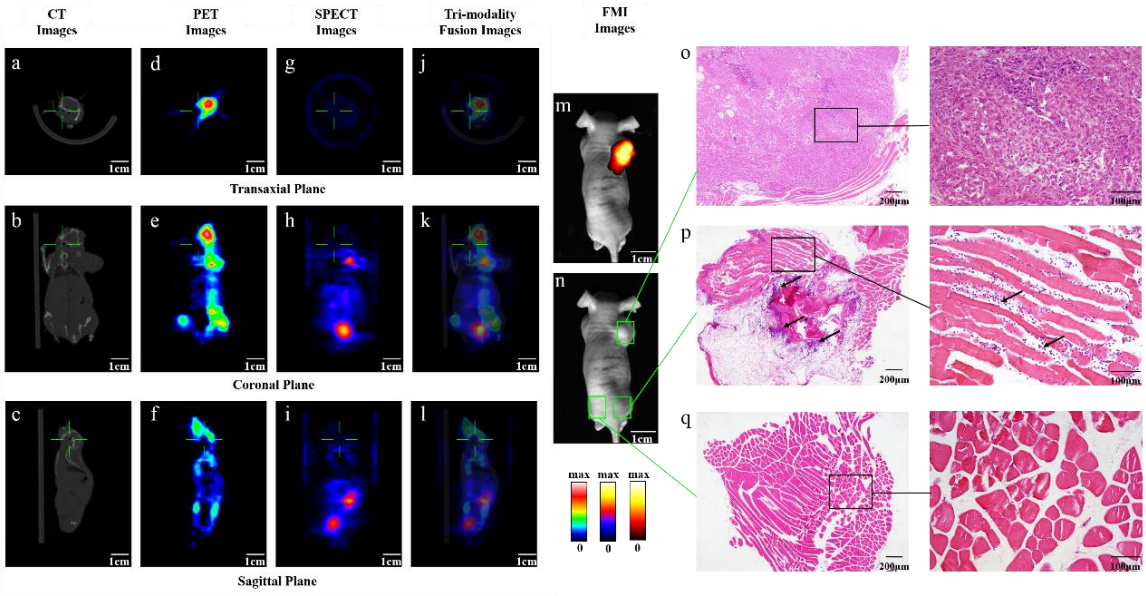

Figure 5.12 – Quad-modality in vivo animal study. Complementing the CT scanning results (a-c), the PET images (d-f) showed high radioactivity accumulation in the brain, the right shoulder and both legs. In SPECT images (g-i), the radioactivity accumulation of 99mTc-3PRGD2 in the right shoulder, the abdomen and the area of bladder was evident. There was only the area of right shoulder that had a great accumulation of Cy7-entrapped CCPM nanoparticles (m). (n) shows the white light image provided by FMI modality. We were able to identify the tumor's location by the complementary information obtained from the PET-SPECT-CT fusion images (j-l), and in addition the FMI imaging result has also confirmed it. The histology (o) confirms the tumor area of right shoulder with high cell proliferation observed with high tracer uptake in PET, SPECT and FMI images. The histology (p) confirms the inflammation area of right leg with a large number of inflammatory cells such as neutrophils (arrow) showed increased F-18 FDG accumulation in PET images. The right, middle and left color bar correspond to the PET images, the SPECT and FMI images respectively. Reprinted from Lu et al [78] with permission. Copyright © 2014 Society of Nuclear Medicine and Molecular Imaging, Inc.

Moreover, by following optimized imaging procedure, the entire imaging time for this in vivo study, including preparation and imaging, took only 3 hours. However, it can be over 6 hours by simply summation of all imaging times from each individual modality. The significant reduction in imaging time is essential to study dynamic physiologies.

In animal disease model study, the quad-modality imaging system successfully acquired tumor images non-invasively and *in vivo*. The animal experiment validated that the four modalities of PET, SPECT, FMI and CT can provide more comprehensive information for molecular imaging studies, improving the overall specificity. In our study, the fusion images of a tumor-xenograft mouse (Figure 5.12) showed complementary information that differentiated between the tumor location and the inflammation location. These findings were confirmed by *ex vivo* histology.

Comparing to the great potential applications of the quad-modality imaging protocol, the tumor imaging result, which we presented previously, is only a drop of the bucket. Metabolism, metastasis and neovascularization are most three important characteristics of the biologic behavior of cancer cell. Differentiation of the subtypes of the same type of cancer cell can result in different biological behaviors and variations in the biologic behavior of cancel cell cause different responses to the treatment. Traditionally, molecular biology approaches such as immunohistochemistry are used for revealing the biologic behavior of cancer cells, however recently molecular imaging approaches, which allows for noninvasive in *vivo* imaging and quantification of biologic processes such as metabolism, metastasis and neovascularization, are more and more widely used in these studies. For instance, the GFP gene can be introduced into cancer cells for monitoring the metastasis of the cancer by using FMI, the F-18 FDG can be adequate in precisely

quantifying the metabolism of cancer cells through PET imaging and the Tc-99m $3PRGD_2$ can reveal the neovascularization of the cancer cells by SPECT imaging. It should be noted that the complexity of biologic behavior of cancer cells is beyond the ability of any single molecular imaging approaches, or molecular tracer, to reveal. Thus, multi-modality and multi-probes molecular imaging would be great helpful in better observing and predicting the biologic behavior of cancer cells. Considering this, we developed the quad-modality molecular imaging system which includes the three major molecular imaging modalities of PET, SPECT and FMI, as well as an X-ray CT to provide the anatomical information.

Multimodal molecular imaging generally required an extended time. For instance, in our system, SPECT typically needs to wait for 60 minutes after the injection of medicine, and it took another 20~30 minutes to finish the scanning. In addition, different imaging modalities might have conflicts, such as the potential risk of crosslink between PET and SPECT. However, summation of operation time by all three molecular imaging modalities, as well as the waiting time of short-lifetime radioactive medicine, will be about 6 hours. Thus, the procedure of multimodal molecular imaging must be carefully optimized to minimize the total scanning time. To avoid crosslink, the PET tracer was injected after the SPECT scan in our system. In addition, long lasting fluorescence tracers could be injected the day before the experiment. Finally, we achieved a 3-hour imaging time. The total length of the scanning time can be even shortened by performance improvement of the imaging system. For example, we can inject both radiolabeling tracers simultaneously by using a better SPECT detector which can differentiate signals from PET tracer [63].

5.2.3 Summary

In this chapter, I have demonstrated the classification of tumor tissue from inflammatory tissues by a quad-modality molecular imaging system with application of three different molecular probes in an animal model. F-18 FDG traces the abnormal metabolic activities by PET imaging. However, the tumor site and inflammation tissue both have high metabolism, thus could not be distinguished by PET in this disease model. Tc-99m 3PRGD$_2$ reveals the neovascularization of the cancer cells by SPECT imaging, and Cy7-entrapped CCPM nanoparticles preferentially accumulate in tumor site because of the EPR effect. From either the PET image or SPECT image alone, the tumor area remained unclear. With the comprehensive information collected from four modalities, the tumor tissue has been successfully distinguished from other false-positive signal from inflammation. Therefore, it is suggested that the tumor tissue could be distinguished in vivo by appropriate application of multimodality molecular imaging along with multiple molecular probes. In current stage, many molecular probes are only available for preclinical uses, which may limit the clinical application of multimodality imaging. With the development of more safe and efficacious molecular probes, the molecular imaging will be a powerful weapon for the classification and distinguish of tumor for early diagnosis.

5.2.4 Experimental

5.2.4.1 Multi-modality imaging protocol

A phantom and a mouse were scanned to evaluate the imaging capability and fusion performance of the system. Geometric calibration and image co-registration was processed. Because the FMI module was setup opposite to the PET/SPECT/CT modules, we generally started with FMI imaging when performing multi-modality imaging, then rotated the

animal bed in the direction of the PET/SPECT/CT modules for the remaining imaging procedures.

Both phantom and animal experiments were carried out to evaluate the imaging capability and fusion performance of the system. As discussed, vast differences in uptake period and imaging technique, each molecular imaging modality requires specific procedure. Therefore, the overall imaging time can last six hours in our system without optimization of the imaging protocols. However, long imaging time not only brings difficulties in dynamic study, but also may cause health hazard for animals. Thus, optimization in the imaging protocol for multimodal molecular imaging is in great desire. Given a physiological or pathological study case, several primary issues to be considered in assigning the imaging sequence are:

1) Uptake time;

2) Preferred imaging period after uptake;

3) Imaging operation time; and

4) Potential crosstalk with other modalities.

In this chapter, the overall optimization principle is: performing imaging with short uptake during the long-uptake period of other modalities; putting modalities that can cause crosstalk with others after its conflict counterparts.

Figure 5.13a listed both imaging period and the uptake period of three molecular tracers. Among them, the radionuclides used in PET imaging will cause a serious crosstalk

problem on the quality of the SPECT imaging (Figure 5.14), the imaging time will be much longer if we start with PET imaging before SPECT imaging. In addition, due to relative long-uptake period for FMI, other modalities can be performed earlier than FMI. Based on these considerations, Figure 5.13b presented our optimized imaging protocol. The total imaging time was shortened to be 180 minutes without the crosstalk influence.

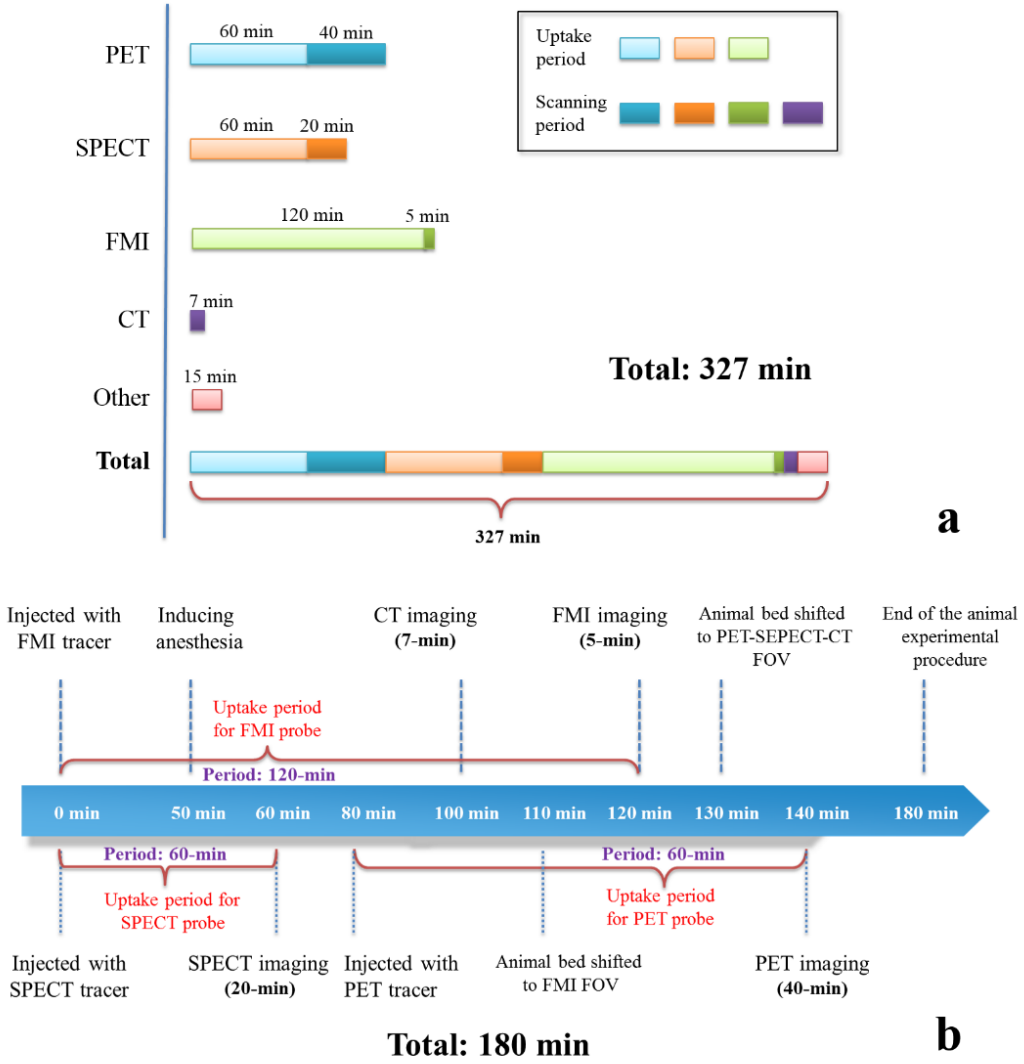

Figure 5.13 – Timeline schematic of the whole animal experimental procedure. A typical multi-modality scanning procedure in animal studies takes about 270 minutes, considering the time needed for drug metabolism. Adapted from Lu et al [78] with permission. Copyright © 2014 Society of Nuclear Medicine and Molecular Imaging, Inc.

5.2.4.2 Phantom studies

The phantom was a cylinder (30 mm in diameter 57 mm long) made of polyvinyl chloride resin, which had a similar light scattering property to that of animal tissue.

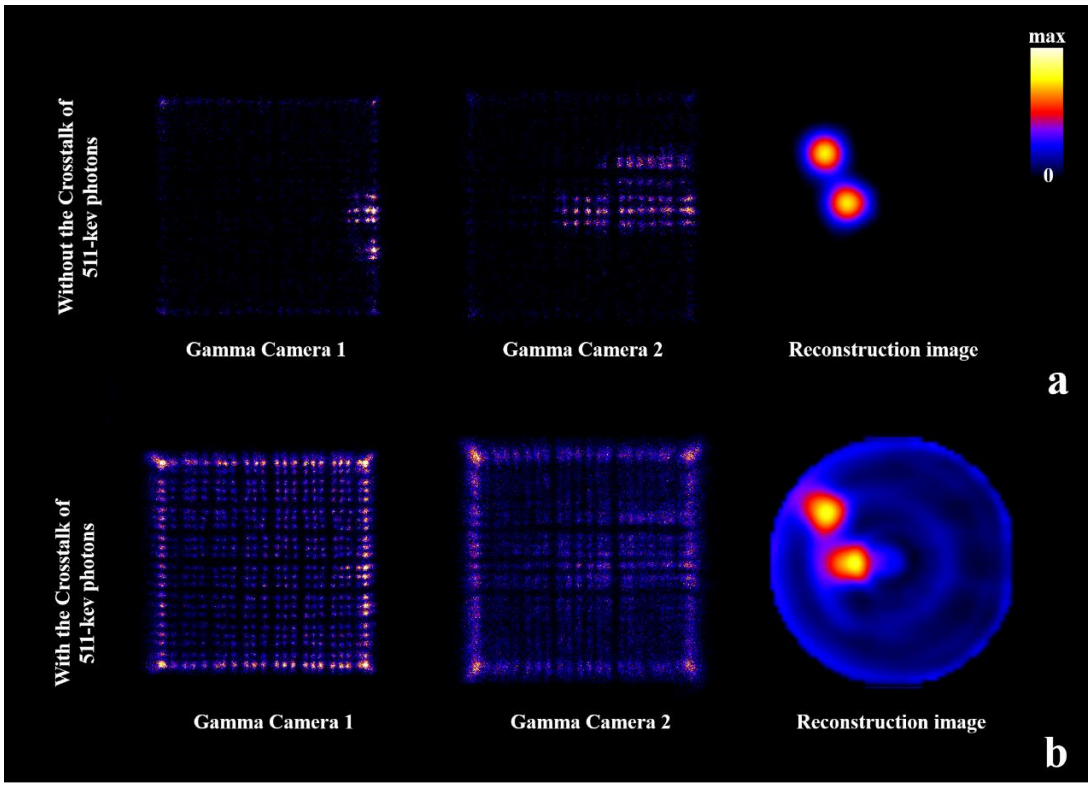

Figure 5.14 – Scattering influence on the quality of the SPECT imaging, which is caused by the crosstalk from the positron-emitting radionuclides. (a) Without the crosstalk of positron-emitting radionuclides, the SPECT module had a good imaging performance. (b) The imaging performance was degraded with the crosstalk of positron-emitting radionuclides.

The phantom contained two glass tubes (inner diameter: 2.2 mm, length: 50 mm) at different insertion depths (28 mm and 45 mm). The bottom zones of the glass tubes were injected with 20 μL (10 μM) indocyanine green (ICG) as the fluorophore for FMI; the middle section of the 45-mm-insertion-depth glass tube was injected with 7.4 MBq (0.2 mCi) of Tc-99m 2-Methoxyisobutylisonitrile (Tc-99m MIBI). The phantom was placed on the animal bed, which was located within the field of view for the FMI module, and

performed fluorescence molecular tomography scanning (360º rotation, scanned for 4 s / 10º, 36 angles in total), after which the animal bed was shifted to the field of view for the PET/SPECT/CT modules and subject to SPECT scan (180º rotation, scanned for 10 s / 3º, 60 angles in total). After completion of the SPECT scan, the middle section of the 28-mm-insertion-depth glass tube was injected with 7.4 MBq (0.2 mCi) of 2-deoxy-2-(^{18}F)fluoro-D-glucose (F-18 FDG) for the PET scan (300 – 650 keV energy window and 12-ns timing window, scanned for 5 min / per bed positions, 3 bed positions). Finally, the phantom was moved to the field of view for the helical CT scan (60 slices, 1.32 mm helical pitch, 360 projection numbers and 25 ms sampling intervals; X-ray tube voltage = 50 keV, at 10 mA).

5.2.4.3 In vivo animal studies

We performed studies on a 16-weeks old, 20-g BALB/C male nude mouse bearing a 10 mm^2 xenograft tumor [induced by hypodermic injection of human pulmonary adenocarcinoma A549 cells (2.5×10^7, 2.5 mL) were injected subcutaneously into the right shoulder flank area of ~16-week-old male nude mice (BALB/c, nu/nu)] in its right shoulder, and chronic inflammation [induced by injecting a proinflammatory substance of Bacillus Calmette-Gu (1 mg/ml, 0.2 mL respectively) into subcutaneous air pouches produced on right hind limb flank area of the mouse] in its right hind limb. The mouse was intravenously injected with 0.2 ml (1.5×10^{15} particles/mouse) Cy7-entrapped CCPM nanoparticles and 37.0 MBq (1.0 mCi) 99mTc-3PRG2 via the tail vein. After 50-min uptake period, the mouse was subject to the anesthesia procedures [2.50% isoflurane in oxygen (1.5 L/min) for inducing anesthesia then lower to 1.00% isoflurane in oxygen (0.8 L/ml) for maintenance], to prevent motion during the multi-modality scanning. The mouse was

scanned with SPECT (180º of rotation, 20 s / 3º, 60 angles; duration 20 min) after the 60-min uptake period of Tc-99m 3PRGD$_2$. Then the mouse was intravenously injected with 37.0 MBq (1.0 mCi) F-18 FDG via the tail vein and the anesthesia gas increased to 2.5% isoflurane in oxygen during the injection and lower to 1.00% after the injection. In the end of the 120-min uptake period of Cy7-CCPM nanoparticles, a helical CT scan (scanned for 60 slices, 1.5 mm helical pitch, 360 projection numbers and 25 ms sampling intervals, X-ray tube voltage is 50 keV and the tube current is 10 mA) was performed to the mouse to obtain CT images. The FMI scan (reflection scan mode for the whole body, integration times of 5s) was started after positioning the mouse on the animal bed. After a 60-min uptake period of F-18 FDG, the mouse was PET scanned (300 - 650 keV energy window, 12-ns timing window, 10 min / bed position) for 40 minutes of four bed positions. The whole animal experimental procedure is illustrated in Figure 5.13b. After the examination, the mouse was sacrificed and the tumor and inflammation tissues were excised, fixed in 4% paraformaldehyde and embedded in paraffin. Hematoxylin-Eosin staining was performed on 5-μm-thick tissue sections.

The PET/SPECT/CT images were reconstructed as aforementioned. Since the subcutaneous tumor lied in a very shallow region of the body, only the 2D fluorescence imaging were given using the epi-illumination FMI. All the reconstructed images were co-registered automatically to perform image fusion. Animal studies were performed in accordance with the guidelines from the Peking University Laboratory Animal Centre and protocols approved by this institution.

CHAPTER 6. CONCLUSION AND OUTLOOK

In this dissertation, I start the investigation on quality control of the synthesis of F-18 ML-10 by elucidating the effect of reductive stabilizer and pH value on the false negative results K2.2.2 detection. After this part, I demonstrate F-18 ML-10 assessment of radiotherapy as a clinical method for the early evaluation of tumor radiotherapy, and the applicability of this method has been discussed by different brain tumor types. Besides, it is suggested that this method shows the potential for the future assessment of subsidiary-injury of lung cancer radiotherapy by clinical and animal studies.

In chapter 1, I introduce the background and priniciples of the researches in this dissertation.

In chapter 2, I demonstrate that the interference from reagents commonly used in F-18 pharmaceutical production to spot test of K2.2.2. No false-positive result of spot test for detection of K2.2.2 has been observed with the presence of seven different amines or other reagents commonly utilized in F-18 radiopharmaceutical synthesis. The interference test demonstrated that the false-negative results are not due to the presence of amines or other chemical impurities. However, it was shown that the pH and the presence of ascorbic acid could lead to false-negative results. The specificity of iodoplatinate staining spot test for K2.2.2 detection has been investigated in this study. The detection of K2.2.2 is not interfered by other chemical impurities. However, the pH should be lower than 8.0, in order to make an accurate detection. The lower limit of the detection is 5 μg/mL by this method, which is applicable for the test of K2.2.2 residue in F-18 FDG injection produced by routes

of synthesis that uses K2.2.2. Therefore, the iodoplatinate staining spot test is rapid and easy to operate, and sample saving (3 μL versus 0.1 mL) for routine quality control.

In chapter 3 and 4, I demonstrate that F-18 ML-10 PET/CT apoptosis imaging to be a potentially safe and effective clinical method for the assessment of early response of radiotherapy by pilot clinical studies. In F-18 ML-10 PET/CT apoptosis imaging, the tracer uptake in normal brain tissue is lower than that in tumor tissue, thus the anatomic positioning of tumor tissue and surrounding edema area could be accurately identified and visualized. More importantly, F-18 ML-10 PET/CT apoptosis imaging can be used for early prediction of the effectiveness of CK radiotherapy. A significant correlation between the rate of change in F-18 ML-10 uptake in the tumor and the rate of subsequent change in tumor volume was observed. In comparison to the therapeutic response in different cancer types, a rapid response in radioactivity, as well as subsequent tumor volume change, has been observed in malignant tumors, which tends to be more sensitive to CK treatment. Besides, the assessment to malignant tumor shows a more linear relationship with the volume change. Another comparison indicates that the therapeutic response of CK treatment is not significantly correlated with the apoptosis level before CK treatment by the study. By evaluation on applicability of this method to different patients, the F-18 ML-10 gives a better assessment to patients aged >50. In chapter 3, the early assessment of therapeutic response by the F-18 ML-10 apoptosis imaging has been first applied to lung cancer, and the result of this assessment is consistent with that of traditional evaluation. Moreover, this study provides evidence that CK treatment could be harmful to heart tissue, due to a rapid apoptotic response from heart tissue after radiotherapy. A follow-up animal study suggests that 20 Gy radiation could induce a rapid apoptosis response of heart tissue

in the radiotherapy. Therefore, it is indicated that this method could be potentially used for the assessment of subsidiary-injury of lung cancer radiotherapy. However, as a pilot study, the amount of clinical cases is limited. Therefore, more future studies need to be carried out to further evaluation of the safety and efficacy of this method.

In chapter 5, I demonstrate the sensitivity investigation of novel molecular probes for real-time guidance for tumor removal surgery. The limit of measurement of SERS particles is 10 thousand times lower than QD800, even 20 thousand times lower than IR800. Furthermore, the dynamic range of SERS nanoparticles is more than 300-fold higher than other 2 imaging probes. These parameters are important for the application of SpectroPen. The Limits of Detection, on one hand, determines the minimal quantity of the injection of contrast agents, which could help with reducing side effect and toxicity. On the other hand, weak tumor-margin signals that are 50-60-fold lower than the central tumor signals. The wider dynamic range provides opportunity for simultaneous measurement without adjusting the data acquisition parameters. I also have demonstrated the classification of tumor tissue from inflammatory tissues by a quad-modality molecular imaging system with application of three different molecular probes in an animal model. F-18 FDG traces the abnormal metabolic activities by PET imaging. However, the tumor site and inflammation tissue both have high metabolism, thus could not be distinguished by PET in this disease model. T-99m 3PRGD$_2$ reveals the neovascularization of the cancer cells by SPECT imaging, and Cy7-entrapped CCPM nanoparticles preferentially accumulate in tumor site because of the EPR effect. From either the PET image or SPECT image alone, the tumor area remained unclear. With the comprehensive information collected from four modalities, the tumor tissue has been successfully distinguished from other false-positive signal from

inflammation. Therefore, it is suggested that the tumor tissue could be distinguished in vivo by appropriate application of multimodality molecular imaging along with multiple molecular probes. In current stage, many molecular probes are only available for preclinical uses, which may limit the clinical application of multimodality imaging. With the development of more safe and efficacious molecular probes, the molecular imaging will be a powerful weapon for the classification and distinguish of tumor for early diagnosis.

In sum, this dissertation demonstrates following creative research:

1. The interference in K2.2.2 detection K2.2.2 detection in quality control in the synthesis of F-18 radiopharmaceuticals has been demonstrated.

2. Application and evaluation on F-18 ML-10 assessment of therapeutic response has been conducted and discussed, by pilot clinical study on 29 cases of patient with intracranial tumor.

3. First application on lung cancer therapeutic response assessment by F-18 ML-10 PET imaging has been conducted and the potential future application has been discussed.

4. The sensitivity of three widely used optical probes for SpectroPen detection has been investigated, and an application on a quad-modal molecular imaging system has been conducted.

As for limitations and future research aims, the clinical investigation on F-18 ML-10 was limited by the amount of clinical cases. Therefore, more clinical studies need to be carried out to further evaluation of the safety and efficacy of this method.

APPENDIX A. A PRELIMINARY STUDY OF F-18 FALLYPREIDE PET/CT BRAIN IMAGING

As a preliminary study of brain imaging of PET/CT, we investigated the visualization of dopamine D2/D3 receptors by F-18 fallypride in normal volunteers by using AMIC Ray-Scan 64 PET/CT. This work was done during July 2014 – May 2015. The dysfunction of dopamine system, a neurotransmission mode playing important roles in human brain, is implicated in many disorders in nervous system, such as Parkinson's disease (PD), Attention Deficit Hyperactivity Disorder (ADHD). F-18-fallypride is a radioactive molecular probe for Positron Emission Tomography (PET) visualizing the Dopamine D2/D3 receptors in striatal and extrastriatal areas.[180-182]

15 normal volunteers (8 males and 7 females) were investigated with AMIC Ray-Scan 64 PET/CT. The F-18-fallypride was injected intravenously (2.96MBq/kg) to normal volunteer 1 hour prior to PET/CT brain scanning. Image reconstruction and data analysis was performed by using AMIC Ray-Scan 64 PET/CT software.

Reconstructed by AMIC Ray-Scan 64 PET/CT software, the image of dopamine system in extrastriatal areas including substantia nigra and red nucleus is visualized clearly, and signal distribution of F-18 fallypride in caudate nucleus and putamen in left and right side is homogeneous and symmetrical in normal volunteers' brain scanning (result is depicted in Figure A1).

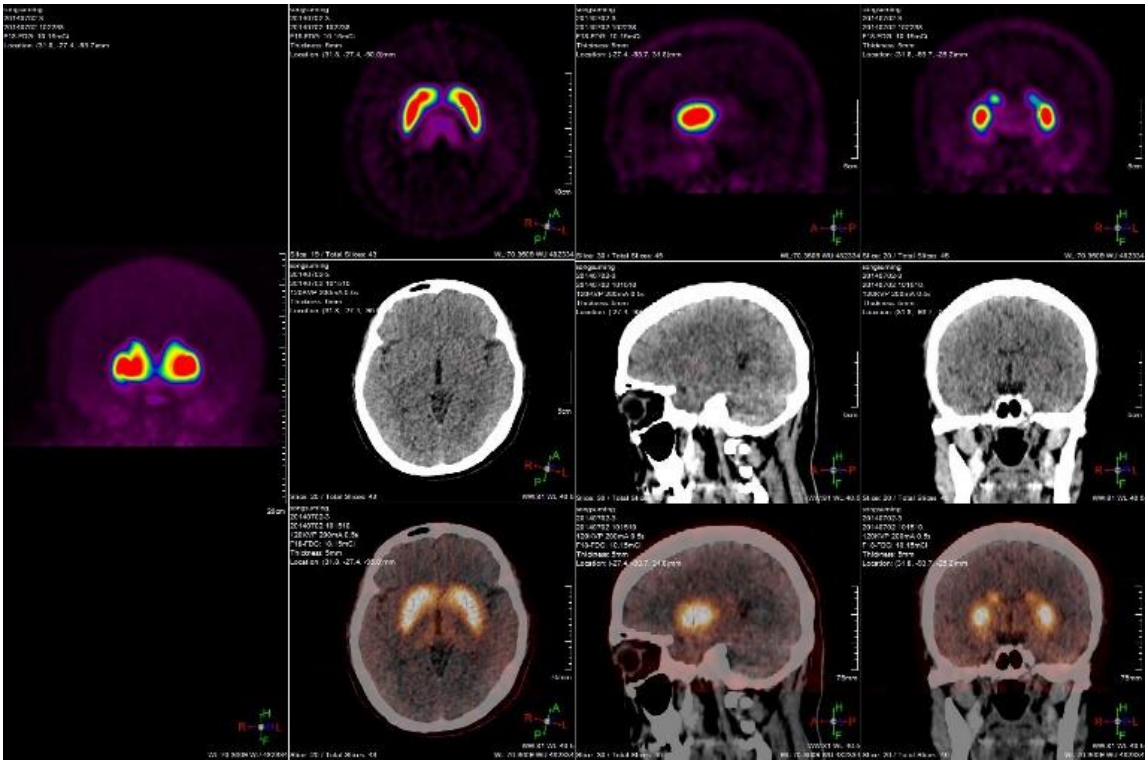

Figure A1 – Signal distribution of F-18 fallypride in caudate nucleus and putamen in left and right side is homogeneous and symmetrical. Adapted from Zhou, et al [183].

F-18 fallypride PET/CT scanning is a promising method in visualizing of neurotransmitters like dopamine receptors due to the decay rate and its strong signal, comparing to other radiotracers. In this study, we confirmed that the AMIC Ray-Scan 64 PET/CT system, as well as F-18 fallypride, performs excellently in dopamine D2/D3 receptors imaging in normal volunteers. Thus, this Ray-Scan system could be widely used in drug discovery and other clinical applications.

APPENDIX B: COPYRIGHT INFORMATION

Chapter 1; Figure 1.1 and Figure 1.5:

Reprinted with permission from Weissleder and Pittet [30]. Copyright © 2008 Nature Publishing Group.

Chapter 1; Figure 1.2:

Reprinted with permission from Hanahan et al [40]. Copyright © 2011 Elsevier Inc.

Chapter 1; Figure 1.3:

Reprinted with permission from Lu et al [78]. Copyright © 2014 Society of Nuclear Medicine and Molecular Imaging, Inc.

Chapter 1; Figure 1.4:

Reprinted with permission from Mohs et al [82]. Copyright © 2010 American Chemical Society.

Chapter 1; Figure 1.7:

Reprinted with permission from Cohen et al [135]. Copyright © 2011 Nature Publishing Group.

Chapter 2; Figure 2.1:

Reprinted with permission from Hamacher el al [152]. Copyright © 2014 Society of Nuclear Medicine and Molecular Imaging, Inc.

Chapter 5; Figure 5.11, Figure 5.12, and Figure 5.13:

Reprinted with permission from Lu et al [78]. Copyright © 2014 Society of Nuclear Medicine and Molecular Imaging, Inc.

REFERENCES

[1] Siegel, R. L., Miller, K. D., Jemal, A., Cancer statistics, 2017[J]. CA: A Cancer Journal for Clinicians, 2017, 67 (1), pp 7-30.

[2] Torre, L. A., Bray, F., Siegel, R. L., et al., Global cancer statistics, 2012[J]. CA: A Cancer Journal for Clinicians, 2015, 65 (2), pp 87-108.

[3] Zheng, R., Zeng, H., Zhang, S., et al., National estimates of cancer prevalence in china, 2011[J]. Cancer Letters, 2016, 370 (1), pp 33-38.

[4] Wang, H., Zhang, J., Tian, J., et al., Using dual-tracer pet to predict the biologic behavior of human colorectal cancer[J]. Journal of Nuclear Medicine, 2009, 50 (11), pp 1857-1864.

[5] Stephen, R., Gillies, R., Promise and progress for functional and molecular imaging of response to targeted therapies[J]. Pharmaceutical Research, 2007, 24 (6), pp 1172-1185.

[6] Ostrom, Q. T., Gittleman, H., Farah, P., et al., Cbtrus statistical report: Primary brain and central nervous system tumors diagnosed in the united states in 2006-2010[J]. Neuro-Oncology, 2013, 15 (Suppl 2), pp ii1-ii56.

[7] Lym, R., Ostrom, Q., Kruchko, C., et al., Completeness and concordancy of who grade assignment for brain and central nervous system tumors in the united states, 2004–2011[J]. Journal of Neuro-Oncology, 2015, 123 (1), pp 43-51.

[8] Louis, D., Ohgaki, H., Wiestler, O., et al., The 2007 who classification of tumours of the central nervous system[J]. Acta Neuropathologica, 2007, 114 (2), pp 97-109.

[9] Allen, A., Ben-Ami, M., Reshef, A., et al., Assessment of response of brain metastases to radiotherapy by pet imaging of apoptosis with 18f-ml-10[J]. European Journal of Nuclear Medicine and Molecular Imaging, 2012, 39 (9), pp 1400-1408.

[10] Kaal, E. C. A., Niël, C. G. J. H., Vecht, C. J., Therapeutic management of brain metastasis[J]. The Lancet Neurology, 2005, 4 (5), pp 289-298.

[11] Mehta, M. P., Tsao, M. N., Whelan, T. J., et al., The american society for therapeutic radiology and oncology (astro) evidence-based review of the role of radiosurgery for brain metastases[J]. International Journal of Radiation Oncology Biology Physics, 2005, 63 (1), pp 37-46.

[12] Aoyama, H., Shirato, H., Tago, M., et al., Stereotactic radiosurgery plus whole-brain radiation therapy vs stereotactic radiosurgery alone for treatment of brain metastases: A randomized controlled trial[J]. JAMA, 2006, 295 (21), pp 2483-2491.

[13] Patchell , R. A., Tibbs , P. A., Walsh , J. W., et al., A randomized trial of surgery in the treatment of single metastases to the brain[J]. New England Journal of Medicine, 1990, 322 (8), pp 494-500.

[14] Mehta, M. P., Paleologos, N. A., Mikkelsen, T., et al., The role of chemotherapy in the management of newly diagnosed brain metastases: A systematic review and evidence-based clinical practice guideline[J]. Journal of Neuro-Oncology, 2010, 96 (1), pp 71-83.

[15] Vuletic, I., Zhou, K., Li, H., et al., Validation of bevacizumab therapy effect on colon cancer subtypes by using whole body imaging in mice[J]. Molecular Imaging and Biology, 2017, pp 1-10.

[16] Hyafil, F., Tran-Dinh, A., Burg, S., et al., Detection of apoptotic cells in a rabbit model with atherosclerosis-like lesions using the positron emission tomography radiotracer [18f] ml-10[J]. Molecular imaging, 2015, 14 (8), pp 433-442.

[17] Ostrom, Q. T., Gittleman, H., Fulop, J., et al., Cbtrus statistical report: Primary brain and central nervous system tumors diagnosed in the united states in 2008-2012[J]. Neuro-Oncology, 2015, 17 (suppl 4), pp iv1-iv62.

[18] Ahmed, R., Oborski, M. J., Hwang, M., et al., Malignant gliomas: Current perspectives in diagnosis, treatment, and early response assessment using advanced quantitative imaging methods[J]. Cancer Management and Research, 2014, 6 pp 149-170.

[19] Oborski, M. J., Laymon, C. M., Lieberman, F. S., et al., First use of 18f-labeled ml-10 pet to assess apoptosis change in a newly diagnosed glioblastoma multiforme patient before and early after therapy[J]. Brain and Behavior, 2014, 4 (2), pp 312-315.

[20] Oborski, M. J., Laymon, C. M., Qian, Y., et al., Challenges and approaches to quantitative therapy response assessment in glioblastoma multiforme using the novel apoptosis positron emission tomography tracer f-18 ml-10[J]. Translational Oncology, 2014, 7 (1), pp 111-119.

[21] Hentschel, M., Appold, S., Schreiber, A., et al., Early fdg pet at 10 or 20 gy under chemoradiotherapy is prognostic for locoregional control and overall survival in patients with head and neck cancer[J]. European Journal of Nuclear Medicine and Molecular Imaging, 2011, 38 (7), pp 1203-1211.

[22] Höglund, J., Shirvan, A., Antoni, G., et al., 18f-ml-10, a pet tracer for apoptosis: First human study[J]. Journal of Nuclear Medicine, 2011, 52 (5), pp 720-725.

[23] Reshef, A., Shirvan, A., Akselrod-Ballin, A., et al., Small-molecule biomarkers for clinical pet imaging of apoptosis[J]. Journal of Nuclear Medicine, 2010, 51 (6), pp 837-840.

[24] Hoebers, F. J. P., Kartachova, M., de Bois, J., et al., (99m)tc hynic-rh-annexin v scintigraphy for in vivo imaging of apoptosis in patients with head and neck cancer treated

with chemoradiotherapy[J]. European Journal of Nuclear Medicine and Molecular Imaging, 2008, 35 (3), pp 509-518.

[25] Fernández-Luna, J. L., Apoptosis regulators as targets for cancer therapy[J]. Clinical and Translational Oncology, 2007, 9 (9), pp 555-562.

[26] Aloya, R., Shirvan, A., Grimberg, H., et al., Molecular imaging of cell death in vivo by a novel small molecule probe[J]. Apoptosis, 2006, 11 (12), pp 2089-2101.

[27] Damianovich, M., Ziv, I., Heyman, S. N., et al., Aposense: A novel technology for functional molecular imaging of cell death in models of acute renal tubular necrosis[J]. European Journal of Nuclear Medicine and Molecular Imaging, 2006, 33 (3), pp 281-291.

[28] Lorberboym, M., Blankenberg, F. G., Sadeh, M., et al., In vivo imaging of apoptosis in patients with acute stroke: Correlation with blood–brain barrier permeability[J]. Brain Research, 2006, 1103 (1), pp 13-19.

[29] Witham, T. F., Okada, H., Fellows, W., et al., The characterization of tumor apoptosis after experimental radiosurgery[J]. Stereotactic and Functional Neurosurgery, 2005, 83 (1), pp 17-24.

[30] Weissleder, R., Pittet, M. J., Imaging in the era of molecular oncology[J]. Nature, 2008, 452 (7187), pp 580-589.

[31] Ale, A., Ermolayev, V., Herzog, E., et al., Fmt-xct: In vivo animal studies with hybrid fluorescence molecular tomography-x-ray computed tomography[J]. Nat Meth, 2012, 9 (6), pp 615-620.

[32] Nahrendorf, M., Keliher, E., Marinelli, B., et al., Hybrid pet-optical imaging using targeted probes[J]. Proceedings of the National Academy of Sciences, 2010, 107 (17), pp 7910-7915.

[33] Jain, R. K., Delivery of molecular and cellular medicine to solid tumors[J]. Advanced Drug Delivery Reviews, 2012, 64, Supplement (0), pp 353-365.

[34] Brigger, I., Dubernet, C., Couvreur, P., Nanoparticles in cancer therapy and diagnosis[J]. Advanced Drug Delivery Reviews, 2012, 64, Supplement (0), pp 24-36.

[35] Vahrmeijer, A. L., Hutteman, M., van der Vorst, J. R., et al., Image-guided cancer surgery using near-infrared fluorescence[J]. Nat Rev Clin Oncol, 2013, 10 (9), pp 507-518.

[36] Gregory, S. G., Sekhon, M., Schein, J., et al., A physical map of the mouse genome[J]. Nature, 2002, 418 (6899), pp 743-750.

[37] Roda, A., Guardigli, M., Pasini, P., et al., Bioluminescence and chemiluminescence in drug screening[J]. Analytical and Bioanalytical Chemistry, 2003, 377 (5), pp 826-833.

[38] Wang, W., El-Deiry, W. S., Bioluminescent molecular imaging of endogenous and exogenous p53-mediated transcription in vitro and in vivo using an hct116 human colon carcinoma xenograft model[J]. Cancer Biology & Therapy, 2003, 2 (2), pp 196-202.

[39] Xibo, M., Zhaofei, L., Xin, Y., et al., Dual-modality monitoring of tumor response to cyclophosphamide therapy in mice with bioluminescence imaging and small-animal positron emission tomography[J]. Molecular Imaging, 2011, 10 (4), pp 278-283.

[40] Hanahan, D., Weinberg, Robert A., Hallmarks of cancer: The next generation[J]. Cell, 2011, 144 (5), pp 646-674.

[41] Weissleder, R., Molecular imaging: Exploring the next frontier[J]. Radiology, 1999, 212 (3), pp 609-614.

[42] Ntziachristos, V., Ripoll, J., Wang, L. V., et al., Looking and listening to light: The evolution of whole-body photonic imaging[J]. Nat Biotech, 2005, 23 (3), pp 313-320.

[43] Bhaumik, S., Gambhir, S. S., Optical imaging of renilla luciferase reporter gene expression in living mice[J]. Proceedings of the National Academy of Sciences of the United States of America, 2002, 99 (1), pp 377-382.

[44] Bushberg, J. T., Seibert, J. A., Leidholdt, E. M., et al., The essential physics of medical imaging[M]. Wolters Kluwer Health: 2011.

[45] de Kemp, R. A., Epstein, F. H., Catana, C., et al., Small-animal molecular imaging methods[J]. Journal of Nuclear Medicine, 2010, 51 (Supplement 1), pp 18S-32S.

[46] Beyer, T., Townsend, D. W., Brun, T., et al., A combined pet/ct scanner for clinical oncology[J]. Journal of Nuclear Medicine, 2000, 41 (8), pp 1369-1379.

[47] Townsend, D. W., Multimodality imaging of structure and function[J]. Physics in Medicine and Biology, 2008, 53 (4), p R1.

[48] Judenhofer, M. S., Wehrl, H. F., Newport, D. F., et al., Simultaneous pet-mri: A new approach for functional and morphological imaging[J]. Nat Med, 2008, 14 (4), pp 459-465.

[49] Zaidi, H., Prasad, R., Advances in multimodality molecular imaging[M]. 2009; p 122-128.

[50] Cherry, S. R., Multimodality imaging: Beyond pet/ct and spect/ct[J]. Seminars in Nuclear Medicine, 2009, 39 (5), pp 348-353.

[51] Ale, A., Ermolayev, V., Herzog, E., et al., Fmt-xct: In vivo animal studies with hybrid fluorescence molecular tomography-x-ray computed tomography[J]. Nature Methods, Jun, 2012, 9 (6), pp 615-+.

[52] Zhang, Q., Brukilacchio, T. J., Li, A., et al., Coregistered tomographic x-ray and optical breast imaging: Initial results[J]. Journal of Biomedical Optics, 2005, 10 (2), pp 024033-024033.

[53] Hasegawa, B. H., Stebler, B., Rutt, B. K., et al., A prototype high-purity germanium detector system with fast photon-counting circuitry for medical imaging[J]. Medical Physics, 1991, 18 (5), pp 900-909.

[54] Lang, T. F., Hasegawa, B. H., Liew, S. C., et al., Description of a prototype emission transmission computed tomography imaging system[J]. Journal of Nuclear Medicine, 1992, 33 (10), pp 1881-1887.

[55] Weisenberger, A. G., Lee, Z., Majewski, S., et al. Development of a triple modality small animal planar imaging system[A], In Nuclear Science Symposium Conference Record, 2005 IEEE[C], 2005.

[56] Parnham, K. B., Chowdhury, S., Li, J., et al. Second-generation, tri-modality pre-clinical imaging system[A], In Nuclear Science Symposium Conference Record, 2006. IEEE[C], 2006; pp 1802-1805.

[57] Culver, J., Akers, W., Achilefu, S., Multimodality molecular imaging with combined optical and spect/pet modalities[J]. Journal of Nuclear Medicine, 2008, 49 (2), pp 169-172.

[58] Davis, S. C., Pogue, B. W., Springett, R., et al., Magnetic resonance–coupled fluorescence tomography scanner for molecular imaging of tissue[J]. Review of Scientific Instruments, 2008, 79 (6), p 064302.

[59] Nahrendorf, M., Waterman, P., Thurber, G., et al., Hybrid in vivo fmt-ct imaging of protease activity in atherosclerosis with customized nanosensors[J]. Arteriosclerosis, Thrombosis, and Vascular Biology, 2009, 29 (10), pp 1444-1451.

[60] Magota, K., Kubo, N., Kuge, Y., et al., Performance characterization of the inveon preclinical small-animal pet/spect/ct system for multimodality imaging[J]. European Journal of Nuclear Medicine and Molecular Imaging, 2011, 38 (4), pp 742-752.

[61] Wang, G., Zhang, J., Gao, H., et al., Omni-tomography/multi-tomography--integrating multiple modalities for simultaneous imaging[J]. OALib, 2011, pp 1-43.

[62] Bohndiek, S. E., Wagadarikar, A., Zavaleta, C. L., et al., A small animal raman instrument for rapid, wide-area, spectroscopic imaging[J]. Proceedings of the National Academy of Sciences, 2013, 110 (30), pp 12408-12413.

[63] Goorden, M. C., van der Have, F., Kreuger, R., et al., Vector: A preclinical imaging system for simultaneous submillimeter spect and pet[J]. Journal of Nuclear Medicine, 2013, 54 (2), pp 306-312.

[64] Quarto, G., Pifferi, A., Bargigia, I., et al., Recipes to make organic phantoms for diffusive optical spectroscopy[J]. Appl. Opt., 2013, 52 (11), pp 2494-2502.

[65] Louie, A., Multimodality imaging probes: Design and challenges[J]. Chemical Reviews, 2010, 110 (5), pp 3146-3195.

[66] Cai, W., Chen, X., Multimodality molecular imaging of tumor angiogenesis[J]. Journal of Nuclear Medicine, 2008, 49 (Suppl 2), pp 113S-128S.

[67] Stout, D. B., Zaidi, H., Preclinical multimodality imaging in vivo[J]. PET Clinics, 2008, 3 (3), pp 251-273.

[68] Mawlawi, O., Townsend, D., Multimodality imaging: An update on pet/ct technology[J]. European Journal of Nuclear Medicine and Molecular Imaging, 2009, 36 pp 15-29.

[69] Hyde, D., de Kleine, R., MacLaurin, S. A., et al., Hybrid fmt–ct imaging of amyloid-β plaques in a murine alzheimer's disease model[J]. NeuroImage, 2009, 44 (4), pp 1304-1311.

[70] Matter, C. M., Stuber, M., Nahrendorf, M., Imaging of the unstable plaque: How far have we got?[J]. European Heart Journal, 2009, 30 (21), pp 2566-2574.

[71] Schober, O., Rahbar, K., Riemann, B., Multimodality molecular imaging — from target description to clinical studies[J]. European Journal of Nuclear Medicine and Molecular Imaging, 2009, 36 (2), pp 302-314.

[72] Zaidi, H., Prasad, R., Advances in multimodality molecular imaging[J]. Journal of Medical Physics, 2009, 34 pp 122-128.

[73] Krohn, K. A., O'Sullivan, F., Crowley, J., et al., Challenges in clinical studies with multiple imaging probes[J]. Nuclear medicine and biology, 2007, 34 (7), pp 879-885.

[74] Beekman, F., Hutton, B., Multi-modality imaging on track[J]. European Journal of Nuclear Medicine and Molecular Imaging, 2007, 34 (9), pp 1410-1414.

[75] Cherry, S. R., Multimodality in vivo imaging system: Twice the power or double the trouble?[J]. Annual Review of Biomedical Engineering, 2006, 8 (1), pp 35-62.

[76] Liu, H., Ren, G., Miao, Z., et al., Molecular optical imaging with radioactive probes[J]. PLoS ONE, 2010, 5 (3), p e9470.

[77] Morse, D. L., Gillies, R. J., Molecular imaging and targeted therapies[J]. Biochemical Pharmacology, 2010, 80 (5), pp 731-738.

[78] Lu, Y., Yang, K., Zhou, K., et al., An integrated quad-modality molecular imaging system for small animals[J]. Journal of Nuclear Medicine, 2014, 55 pp 1-5.

[79] Nguyen, Q. T., Olson, E. S., Aguilera, T. A., et al., Surgery with molecular fluorescence imaging using activatable cell-penetrating peptides decreases residual cancer and improves survival[J]. Proceedings of the National Academy of Sciences of the United States of America, 2010, 107 (9), pp 4317-4322.

[80] Yoo, H., Kim, J. W., Shishkov, M., et al., Intra-arterial catheter for simultaneous microstructural and molecular imaging in vivo[J]. Nat Med, 2011, 17 (12), pp 1680-1684.

[81] Madajewski, B., Judy, B. F., Mouchli, A., et al., Intraoperative near-infrared imaging of surgical wounds after tumor resections can detect residual disease[J]. Clinical cancer research : an official journal of the American Association for Cancer Research, 2012, 18 (20), pp 5741-5751.

[82] Mohs, A. M., Mancini, M. C., Singhal, S., et al., Hand-held spectroscopic device for in vivo and intraoperative tumor detection: Contrast enhancement, detection sensitivity, and tissue penetration[J]. Analytical Chemistry, 2010, 82 (21), pp 9058-9065.

[83] Okusanya, O. T., DeJesus, E. M., Jiang, J. X., et al., Intraoperative molecular imaging can identify lung adenocarcinomas during pulmonary resection[J]. The Journal of Thoracic and Cardiovascular Surgery, 2015, 150 (1), pp 28-35.

[84] Buttan, A. K., Panagiotides, G., Barnes, M. J., et al., Multimodality imaging in the diagnosis of coexisting left atrial myxoma and aortic valve papillary fibroelastoma[J]. Circulation, 2012, 125 (23), pp e1003-e1005.

[85] Guerrero, S., Herance, J. R., Rojas, S., et al., Synthesis and in vivo evaluation of the biodistribution of a 18f-labeled conjugate gold-nanoparticle-peptide with potential biomedical application[J]. Bioconjugate Chemistry, 2012, 23 (3), pp 399-408.

[86] Huang, H., Mei, L., Chu, T., Synthesis, radiolabeling and biological evaluation of propylene amine oxime complexes containing nitrotriazoles as hypoxia markers[J]. Molecules, 2012, 17 (6), pp 6808-6820.

[87] Mei, L., Wang, Y., Chu, T., 99mtc/re complexes bearing bisnitroimidazole or mononitroimidazole as potential bioreductive markers for tumor: Synthesis, physicochemical characterization and biological evaluation[J]. European Journal of Medicinal Chemistry, 2012, 58 pp 50-63.

[88] Shahjamali, M. M., Bosman, M., Cao, S., et al., Gold coating of silver nanoprisms[J]. Advanced Functional Materials, 2012, 22 (4), pp 849-854.

[89] Dongkyu, K., Mi Kyung, Y., Tae Sup, L., et al., Amphiphilic polymer-coated hybrid nanoparticles as ct/mri dual contrast agents[J]. Nanotechnology, 2011, 22 (15), p 155101.

[90] Li, G.-W., Xie, X. S., Central dogma at the single-molecule level in living cells[J]. Nature, 2011, 475 (7356), pp 308-315.

[91] Morales-Avila, E., Ferro-Flores, G., Ocampo-García, B. E., et al., Multimeric system of 99mtc-labeled gold nanoparticles conjugated to c[rgdfk(c)] for molecular imaging of tumor α(v)β(3) expression[J]. Bioconjugate Chemistry, 2011, 22 (5), pp 913-922.

[92] Ocampo-García, B. E., Ramírez, F. d. M., Ferro-Flores, G., et al., 99mtc-labelled gold nanoparticles capped with hynic-peptide/mannose for sentinel lymph node detection[J]. Nuclear Medicine and Biology, 2011, 38 (1), pp 1-11.

[93] Reuveni, T., Motiei, M., Romman, Z., et al., Targeted gold nanoparticles enable molecular ct imaging of cancer: An in vivo study[J]. international Journal of Nanomedicine, 2011, 6 p 2859.

[94] Schuster, D. M., Savir-Baruch, B., Nieh, P. T., et al., Detection of recurrent prostate carcinoma with anti-1-amino-3-18f-fluorocyclobutane-1-carboxylic acid pet/ct and 111in–capromab pendetide spect/ct[J]. Radiology, 2011, 259 (3), pp 852-861.

[95] Woodard, L. E., Nimmagadda, S., Cxcr4-based imaging agents[J]. Journal of Nuclear Medicine, 2011, 52 (11), pp 1665-1669.

[96] Baker, M., Whole-animal imaging: Probe progress[J]. Nature, 2010, 463 (7283), pp 979-979.

[97] Casals, E., Pfaller, T., Duschl, A., et al., Time evolution of the nanoparticle protein corona[J]. ACS Nano, 2010, 4 (7), pp 3623-3632.

[98] de la Zerda, A., Bodapati, S., Teed, R., et al., A comparison between time domain and spectral imaging systems for imaging quantum dots in small living animals[J]. Molecular Imaging and Biology, 2010, 12 (5), pp 500-508.

[99] Jacobson, O., Weiss, I. D., Kiesewetter, D. O., et al., Pet of tumor cxcr4 expression with 4-18f-t140[J]. Journal of Nuclear Medicine, 2010, 51 (11), pp 1796-1804.

[100] Ji, L., Ahmed, C., Steven, J. C., et al., A novel functional ct contrast agent for molecular imaging of cancer[J]. Physics in Medicine and Biology, 2010, 55 (15), p 4389.

[101] Minchin, R. F., Martin, D. J., Minireview: Nanoparticles for molecular imaging—an overview[J]. Endocrinology, 2010, 151 (2), pp 474-481.

[102] Nimmagadda, S., Pullambhatla, M., Stone, K., et al., Molecular imaging of cxcr4 receptor expression in human cancer xenografts with [64cu]amd3100 positron emission tomography[J]. Cancer Research, 2010, 70 (10), pp 3935-3944.

[103] Chu, T., Xu, H., Yang, Z., et al., Synthesis and in vitro evaluation of three 99mtc-labeled hydroxamamide-based ligands as markers for hypoxic cells[J]. Applied Radiation and Isotopes, 2009, 67 (4), pp 590-593.

[104] Kosaka, N., Ogawa, M., Sato, N., et al., In vivo real-time, multicolor, quantum dot lymphatic imaging[J]. J Invest Dermatol, 2009, 129 (12), pp 2818-2822.

[105] Nimmagadda, S., Pullambhatla, M., Pomper, M. G., Immunoimaging of cxcr4 expression in brain tumor xenografts using spect/ct[J]. Journal of Nuclear Medicine, 2009, 50 (7), pp 1124-1130.

[106] Yaghoubi, S. S., Jensen, M. C., Satyamurthy, N., et al., Noninvasive detection of therapeutic cytolytic t cells with 18f-fhbg pet in a patient with glioma[J]. Nat Clin Prac Oncol, 2009, 6 (1), pp 53-58.

[107] Yang, Z., Leon, J., Martin, M., et al., Pharmacokinetics and biodistribution of near-infrared fluorescence polymeric nanoparticles[J]. Nanotechnology, 2009, 20 (16), p 165101.

[108] Lane, L. A., Qian, X., Smith, A. M., et al., Physical chemistry of nanomedicine: Understanding the complex behaviors of nanoparticles in vivo[J]. Annual Review of Physical Chemistry, 2015, 66 (1), pp 521-547.

[109] Mitragotri, S., Burke, P. A., Langer, R., Overcoming the challenges in administering biopharmaceuticals: Formulation and delivery strategies[J]. Nat Rev Drug Discov, 2014, 13 (9), pp 655-672.

[110] Sykes, E. A., Chen, J., Zheng, G., et al., Investigating the impact of nanoparticle size on active and passive tumor targeting efficiency[J]. ACS Nano, 2014, 8 (6), pp 5696-5706.

[111] Torchilin, V. P., Multifunctional, stimuli-sensitive nanoparticulate systems for drug delivery[J]. Nat Rev Drug Discov, 2014, 13 (11), pp 813-827.

[112] Bao, G., Mitragotri, S., Tong, S., Multifunctional nanoparticles for drug delivery and molecular imaging[J]. Annual Review of Biomedical Engineering, 2013, 15 (1), pp 253-282.

[113] Chauhan, V. P., Jain, R. K., Strategies for advancing cancer nanomedicine[J]. Nat Mater, 2013, 12 (11), pp 958-962.

[114] Lesniak, A., Salvati, A., Santos-Martinez, M. J., et al., Nanoparticle adhesion to the cell membrane and its effect on nanoparticle uptake efficiency[J]. Journal of the American Chemical Society, 2013, 135 (4), pp 1438-1444.

[115] Levine, P. M., Carberry, T. P., Holub, J. M., et al., Crafting precise multivalent architectures[J]. MedChemComm, 2013, 4 (3), pp 493-509.

[116] Prabhakar, U., Maeda, H., Jain, R. K., et al., Challenges and key considerations of the enhanced permeability and retention effect for nanomedicine drug delivery in oncology[J]. Cancer Research, 2013, 73 (8), pp 2412-2417.

[117] Albanese, A., Tang, P. S., Chan, W. C. W., The effect of nanoparticle size, shape, and surface chemistry on biological systems[J]. Annual Review of Biomedical Engineering, 2012, 14 (1), pp 1-16.

[118] Canton, I., Battaglia, G., Endocytosis at the nanoscale[J]. Chemical Society Reviews, 2012, 41 (7), pp 2718-2739.

[119] Sharifi, S., Behzadi, S., Laurent, S., et al., Toxicity of nanomaterials[J]. Chemical Society Reviews, 2012, 41 (6), pp 2323-2343.

[120] Walkey, C. D., Chan, W. C. W., Understanding and controlling the interaction of nanomaterials with proteins in a physiological environment[J]. Chemical Society Reviews, 2012, 41 (7), pp 2780-2799.

[121] Walkey, C. D., Olsen, J. B., Guo, H., et al., Nanoparticle size and surface chemistry determine serum protein adsorption and macrophage uptake[J]. Journal of the American Chemical Society, 2011, 134 (4), pp 2139-2147.

[122] Wilson, R., Yeping, X., Jie, C., et al., Pharmacokinetic and toxicological evaluation of multi-functional thiol-6-fluoro-6-deoxy-d-glucose gold nanoparticles in vivo[J]. Nanotechnology, 2012, 23 (37), p 375101.

[123] Carmeliet, P., Jain, R. K., Molecular mechanisms and clinical applications of angiogenesis[J]. Nature, 2011, 473 (7347), pp 298-307.

[124] Chauhan, V. P., Stylianopoulos, T., Boucher, Y., et al., Delivery of molecular and nanoscale medicine to tumors: Transport barriers and strategies[J]. Annual Review of Chemical and Biomolecular Engineering, 2011, 2 (1), pp 281-298.

[125] Chou, L. Y. T., Ming, K., Chan, W. C. W., Strategies for the intracellular delivery of nanoparticles[J]. Chemical Society Reviews, 2011, 40 (1), pp 233-245.

[126] Kunzmann, A., Andersson, B., Thurnherr, T., et al., Toxicology of engineered nanomaterials: Focus on biocompatibility, biodistribution and biodegradation[J]. Biochimica et Biophysica Acta (BBA) - General Subjects, 2011, 1810 (3), pp 361-373.

[127] Zhao, F., Zhao, Y., Liu, Y., et al., Cellular uptake, intracellular trafficking, and cytotoxicity of nanomaterials[J]. Small, 2011, 7 (10), pp 1322-1337.

[128] Cho, K., Wang, X., Nie, S., et al., Therapeutic nanoparticles for drug delivery in cancer[J]. Clinical Cancer Research, 2008, 14 (5), pp 1310-1316.

[129] Choi, H. S., Liu, W., Misra, P., et al., Renal clearance of nanoparticles[J]. Nature biotechnology, 2007, 25 (10), pp 1165-1170.

[130] Kim, B. Y. S., Rutka, J. T., Chan, W. C. W., Nanomedicine[J]. New England Journal of Medicine, 2010, 363 (25), pp 2434-2443.

[131] Nie, S., Xing, Y., Kim, G. J., et al., Nanotechnology applications in cancer[J]. Annual Review of Biomedical Engineering, 2007, 9 (1), pp 257-288.

[132] Smith, A. M., Duan, H., Mohs, A. M., et al., Bioconjugated quantum dots for in vivo molecular and cellular imaging[J]. Advanced Drug Delivery Reviews, 2008, 60 (11), pp 1226-1240.

[133] Yang, D. J., Azhdarinia, A., Wu, P., et al., In vivo and in vitro measurement of apoptosis in breast cancer cells using 99mtc-ec-annexin v[J]. Cancer Biotherapy and Radiopharmaceuticals, 2001, 16 (1), pp 73-83.

[134] Tait, J. F., Imaging of apoptosis[J]. Journal of Nuclear Medicine, 2008, 49 (10), pp 1573-1576.

[135] Cohen, A., Shirvan, A., Levin, G., et al., From the gla domain to a novel small-molecule detector of apoptosis[J]. Cell Res, 2009, 19 (5), pp 625-637.

[136] Baudot, P., Jacque, M., Robin, M., Effect of a diaza-polyoxa-macrobicyclic complexing agent on the urinary elimination of lead in lead-poisoned rats[J]. Toxicology and Applied Pharmacology, 1977, 41 (1), pp 113-118.

[137] Lewis Sr, R., Tatken, R., Registry of toxic effects of chemical substances, us department of health and human services[M]. 1979.

[138] Convention, U. S. P., U.S. Pharmacopeia & national formulary[M]. 40 ed.; Rockville, MD, USA: United States Pharmacopeial Convention, Incorporated: 2016.

[139] Commission, C. P., Pharmacopoeia of the people's republic of china[M]. Beijing, China: Chemical Industry Press: 2015.

[140] Europe, C. o., Commission, E. P., European pharmacopoeia[M]. 9.0 ed.; Strasbourg, France: Council of Europe: 2016.

[141] Alexoff, D. L., Fowler, J. S., Gatley, S. J., Removal of the 2.2.2 cryptand (kryptofix 2.2.2™) from 18fdg by cation exchange[J]. International Journal of Radiation Applications and Instrumentation. Part A. Applied Radiation and Isotopes, 1991, 42 (12), pp 1189-1193.

[142] Chaly, T., Dahl, J. R., Thin layer chromatographic detection of kryptofix 2.2.2 in the routine synthesis of [18f]2-fluoro-2-deoxy-d-glucose[J]. International Journal of Radiation Applications and Instrumentation. Part B. Nuclear Medicine and Biology, 1989, 16 (4), pp 385-387.

[143] Mock, B. H., Winkle, W., Vavrek, M. T., A color spot test for the detection of kryptofix 2.2.2 in [18f]fdg preparations[J]. Nuclear Medicine and Biology, 1997, 24 (2), pp 193-195.

[144] Scott, P. J. H., Kilbourn, M. R., Determination of residual kryptofix 2.2.2 levels in [18f]-labeled radiopharmaceuticals for human use[J]. Applied Radiation and Isotopes, 2007, 65 (12), pp 1359-1362.

[145] Ferrieri, R. A., Schlyer, D. J., Alexoff, D. L., et al., Direct analysis of kryptofix 2.2.2 in 18fdg by gas chromatography using a nitrogen-selective detector[J]. Nuclear Medicine and Biology, 1993, 20 (3), pp 367-369.

[146] Kruse, M., Rees, S., Watkins, G. Quality control of kryptofix or tetrabutylammonium ion in fdg samples by quantitative hplc analysis[A], In Journal of Nuclear Medicine[C], 2000; p 148.

[147] Nakao, R., Ito, T., Yamaguchi, M., et al., Simultaneous analysis of fdg, cldg and kryptofix 2.2.2 in [18f]fdg preparation by high-performance liquid chromatography with uv detection[J]. Nuclear Medicine and Biology, 2008, 35 (2), pp 239-244.

[148] Ma, Y., Huang, B. X., Channing, M. A., et al., Quantification of kryptofix 2.2.2 in 2-[18f]fdg and other radiopharmaceuticals by lc/ms/ms[J]. Nuclear Medicine and Biology, 2002, 29 (1), pp 125-129.

[149] Zweig, G., Sherma, J., Crc handbook of chromatography: General data and principles[M]. CRC press, Inc: 1972.

[150] Kuntzsch, M., Lamparter, D., Brüggener, N., et al., Development and successful validation of simple and fast tlc spot tests for determination of kryptofix® 2.2.2 and tetrabutylammonium in 18f-labeled radiopharmaceuticals[J]. Pharmaceuticals, 2014, 7 (5), p 621.

[151] Hung, T.-M., Ho, C.-M., Liu, Y.-C., et al., Up-regulation of microrna-190b plays a role for decreased igf-1 that induces insulin resistance in human hepatocellular carcinoma[J]. PLoS ONE, 2014, 9 (2), p e89446.

[152] Hamacher, K., Coenen, H. H., Stöcklin, G., Efficient stereospecific synthesis of no-carrier-added 2-[18f]-fluoro-2-deoxy-d-glucose using aminopolyether supported nucleophilic substitution[J]. Journal of Nuclear Medicine, 1986, 27 (2), pp 235-238.

[153] Scott, P. J. H., Hockley, B. G., Kung, H. F., et al., Studies into radiolytic decomposition of fluorine-18 labeled radiopharmaceuticals for positron emission tomography[J]. Applied Radiation and Isotopes, 2009, 67 (1), pp 88-94.

[154] Fawdry, R. M., Radiolysis of 2-[18f]fluoro-2-deoxy-d-glucose (fdg) and the role of reductant stabilisers[J]. Applied Radiation and Isotopes, 2007, 65 (11), pp 1193-1201.

[155] Liu, S., Ellars, C. E., Edwards, D. S., Ascorbic acid: Useful as a buffer agent and radiolytic stabilizer for metalloradiopharmaceuticals[J]. Bioconjugate Chemistry, 2003, 14 (5), pp 1052-1056.

[156] Yan, M., Qin, Z., Cheng, P., et al., The synthesis of fdg on improved multifunction module using sumitomo cfn fluoride as raw material[J]. Journal of Isotopes, 2013, 26 (3), pp 175-179.

[157] Wang, Q., Ru, Q., Ding, W., et al., New method for preparation and quality control of^{18}f-fdg synthesized by siemens explora fdg4 synthetic system[J]. Journal of Modern Medicine and Health, 2011, 27 (5), pp 656-657.

[158] Zhang, J., Tian, J., Huan, D., et al., Basic hydrolysis of 1,3,4,5-tetra-o-acetyl-2-[^{18}f] fluoro-*d*-glucose on solid phase extraction[J]. Journal of Isotopes, 2003, 16 (3), pp 222-225.

[159] Mosdzianowski, C., Lemaire, C., Simoens, F., et al., Epimerization study on [18f]fdg produced by an alkaline hydrolysis on solid support under stringent conditions[J]. Applied Radiation and Isotopes, 2002, 56 (6), pp 871-875.

[160] Drumhiller, J. A., Laing, J. L., Taylor, R. W., Spectrophotometric titration of cryptands and complexiметric titration of barium with cryptand (2.2.2)[J]. Analytica Chimica Acta, 1984, 162 pp 315-321.

[161] Zhang, J., Chen, Z., Wu, X., et al., Specificity of the spectrophotometry for detecting aminopolyether k2.2.2 in ^{18}f-fdg[J]. Journal of Isotopes, 2015, 28 (3), pp 129-134.

[162] Meggiato, T., Calabrese, F., Valente, M., et al., Spontaneous apoptosis and proliferation in human pancreatic cancer[J]. Pancreas, 2000, 20 (2), pp 117-122.

[163] Gui, Y., Xu, Z., Zhang, X., et al., Synthesis precursor of apoptosis imaging agent ^{18}f-ml-10 and its radiolabing with ^{18}f[J]. Journal of Nuclear and Radiochemistry, 2016, 38 (3), pp 188-192.

[164] Moffat, B. A., Chenevert, T. L., Lawrence, T. S., et al., Functional diffusion map: A noninvasive mri biomarker for early stratification of clinical brain tumor response[J]. Proceedings of the National Academy of Sciences of the United States of America, 2005, 102 (15), pp 5524-5529.

[165] Ariji, Y., Fuwa, N., Kodaira, T., et al., False-positive positron emission tomography appearance with 18f-fluorodeoxyglucose after definitive radiotherapy for cancer of the mobile tongue[J]. The British Journal of Radiology, 2009, 82 (973), pp e3-e7.

[166] Kerr, J. F. R., Wyllie, A. H., Currie, A. R., Apoptosis: A basic biological phenomenon with wide-ranging implications in tissue kinetics[J]. British Journal of Cancer, 1972, 26 (4), pp 239-257.

[167] Sgonc, R., Gruber, J., Apoptosis detection: An overview[J]. Experimental Gerontology, 1998, 33 (6), pp 525-533.

[168] Qian, X., Emory, S. R., Nie, S., Anchoring molecular chromophores to colloidal gold nanocrystals: Surface-enhanced raman evidence for strong electronic coupling and irreversible structural locking[J]. Journal of the American Chemical Society, 2012, 134 (4), pp 2000-2003.

[169] Qian, X., Nie, S., Surface‐enhanced raman nanoparticles for in‐vivo tumor targeting and spectroscopic detection[J]. AIP Conference Proceedings, 2010, 1267 (1), p 81.

[170] Qian, X., Peng, X.-H., Ansari, D. O., et al., In vivo tumor targeting and spectroscopic detection with surface-enhanced raman nanoparticle tags[J]. Nat Biotech, 2008, 26 (1), pp 83-90.

[171] Wang, X., Qian, X., Beitler, J. J., et al., Detection of circulating tumor cells in human peripheral blood using surface-enhanced raman scattering nanoparticles[J]. Cancer Research, 2011, 71 (5), pp 1526-1532.

[172] Doering, W. E., Nie, S., Single-molecule and single-nanoparticle sers: Examining the roles of surface active sites and chemical enhancement[J]. The Journal of Physical Chemistry B, 2002, 106 (2), pp 311-317.

[173] Gómez-Graña, S., Pérez-Juste, J., Alvarez-Puebla, R. A., et al., Self-assembly of au@ag nanorods mediated by gemini surfactants for highly efficient sers-active supercrystals[J]. Advanced Optical Materials, 2013, 1 (7), pp 477-481.

[174] Jiang, X., Jiang, Z., Xu, T., et al., Surface-enhanced raman scattering-based sensing in vitro: Facile and label-free detection of apoptotic cells at the single-cell level[J]. Analytical Chemistry, 2013, 85 (5), pp 2809-2816.

[175] Lee, S., Chon, H., Lee, J., et al., Rapid and sensitive phenotypic marker detection on breast cancer cells using surface-enhanced raman scattering (sers) imaging[J]. Biosensors and Bioelectronics, 2013, 51 pp 238-243.

[176] Liu, M., Wang, Z., Zong, S., et al., Sers-based DNA detection in aqueous solutions using oligonucleotide-modified ag nanoprisms and gold nanoparticles[J]. Analytical and Bioanalytical Chemistry, 2013, 405 (18), pp 6131-6136.

[177] McVeigh, P. Z., Mallia, R. J., Veilleux, I., et al., Widefield quantitative multiplex surface enhanced raman scattering imaging in vivo[J]. Journal of Biomedical Optics, 2013, 18 (4), p 046011.

[178] Ming, X., James, N., Veera, A., et al., Gold nanotags for combined multi-colored raman spectroscopy and x-ray computed tomography[J]. Nanotechnology, 2010, 21 (3), p 035101.

[179] Okusanya, O. T., Deshpande, C., Barbosa, E. M., et al., Molecular imaging to identify tumor recurrence following chemoradiation in a hostile surgical environment[J]. Molecular imaging, 2014, 13 pp 1-6.

[180] Slifstein, M., Kegeles, L. S., Xu, X., et al., Striatal and extrastriatal dopamine release measured with pet and [18f] fallypride[J]. Synapse, 2010, 64 (5), pp 350-362.

[181] Slifstein, M., Narendran, R., Hwang, D.-R., et al., Effect of amphetamine on [18f]fallypride in vivo binding to d2 receptors in striatal and extrastriatal regions of the primate brain: Single bolus and bolus plus constant infusion studies[J]. Synapse, 2004, 54 (1), pp 46-63.

[182] Ceccarini, J., Vrieze, E., Koole, M., et al., Optimized in vivo detection of dopamine release using 18f-fallypride pet[J]. Journal of Nuclear Medicine, 2012, 53 (10), pp 1565-1572.

[183] Zhou, K., Guo, Z., Zhang, J., et al., Brain imaging of dopamine d2/d3 receptors of 18f-fallypride-pet in normal volunteers: An amic ray-scan 64 pet/ct clinical system clinical trial[J]. Journal of Nuclear Medicine, 2015, 56 (supplement 3), p 1626.

PUBLICATIONS

[1] **Zhou, K**., Guo, Z., Zhang, J., Tian, J., Ren, Q. Brain imaging of dopamine D2/D3 receptors of 18F-fallypride-PET in normal volunteers: An AMIC Ray-Scan 64 PET/CT clinical system clinical trial. Journal of Nuclear Medicine 2015 vol. 56 no. supplement 3:1626.

[2] **Zhou, K.**, Zhang, J., Chen, Z., Wu, X., Zhang, X., Ren, Q. Interference on K2.2.2 detection via spot test. Journal of Radioanalytical and Nuclear Chemistry 2017. In submission.

[3] Lu, Y., Yang, K., **Zhou, K.**, Pang, B., Wang, G., Ding, Y., Zhang, Q., Hang, H., Tian, J., Li, C., Ren, Q. An Integrated Quad-Modality Molecular Imaging System for Small Animals. Journal of Nuclear Medicine 2014, 55: 1-5.

[4] Lu, Y., Yang, K., **Zhou, K.**, Zhang, Q., Pang, B., Ren, Q. Development of a SiPM-based PET imaging system for small animals. Nuclear Instruments and Methods in Physics Research Section A: Accelerators, Spectrometers, Detectors and Associated Equipment 2014, 743: 30-38.

[5] Vuletic, I., **Zhou, K.**, Li, H., Bai, H., Meng, X., Zhu, S., Ding, Y., Li, J., Sun, H., Ren, Q. Validation of Bevacizumab therapy effect on colon cancer subtypes by using whole body imaging in mice. Molecular Imaging and Biology 2017. Doi: 10.1007/s11307-017-1048-z.

[6] Sun, L.*, **Zhou, K.***, Wang, W., Zhang, X., Ju, Z., Qu, B., Yu, X., Zhang, J., Pan, L. F-18 ML-10 imaging for assessment of apoptotic response of intracranial tumor early after radiotherapy by PET/CT. Cureus 2017. In submission.

[7] Wang, L, Vuletic, I., Deng, D., Crielaard, W., Xie, Z., **Zhou, K**., Zhang, J., Sun, H., Ren, Q., Guo, C. Bifidobacterium breve as a delivery vector of IL-24 gene therapy for Head and Neck Squamous Cell Carcinoma in vivo. Gene therapy 2017. Under review.

[8] Ren, Q., Lu, Y., Yang, K., Jiang, X., Pang, B., **Zhou, K.**, Zhang, Q. Multimodal Molecular Image Imaging Device for Small Animal and Imaging Method. 2014. Pub. No.: WO/2014/019351.

VITA

Kedi Zhou

Kedi was born in Beijing, China. He attended public schools in Beijing, received a BS in Biotechnology and a BA in English from Huazhong University of Science and Technology, China in 2011 before enrolling in joint PhD program in Peking University, Georgia Institute of Technology and Emory University. When he is not working on his research, Mr. Zhou enjoys playing sports and travelling.